Simulation, construction and application of focused pinhole small animal SPECT

Brendan Vastenhouw

Printing of this thesis was financially supported by MILabs B.V., Utrecht, the Netherlands

Cover: collimator with pinholes (image: Norbert Gehéniau).

ISBN: 978-90-393-4941-0

Printed by Gildeprint, Enschede, the Netherlands

Simulation, construction and application of focused pinhole small animal SPECT

Simulatie, constructie en toepassing van gefocusseerde pinhole SPECT bij kleine dieren

(met een samenvatting in het Nederlands)

Proefschrift

ter verkrijging van de graad van doctor aan de Universiteit Utrecht
op gezag van de rector magnificus, prof.dr. J.C. Stoof, ingevolge het besluit
van het college voor promoties in het openbaar te verdedigen
op donderdag 6 november 2008 des middags te 12.45 uur

door

Brendan Vastenhouw

geboren op 28 februari 1974 te Zaanstad

Promotoren: **Prof. dr. F. J. Beekman**

Prof. dr. ir. M. A. Viergever

Het onderzoek werd mede mogelijk gemaakt met financiële steun van de Nederlandse Organisatie voor Wetenschappelijk Onderzoek (NWO, project 917.036.335) en een ‘high potential’ beurs van het UMC Utrecht.

Contents

Chapter 1

Introduction and thesis outline

New developments in molecular imaging techniques like small animal Single Photon Emission Computed Tomography (SPECT) systems are important tools to analyze mouse models of human diseases. Standard techniques like histology, protein staining, *in-situ* hybridisation and autoradiography, used to locate different types of cells and show the distribution of tissue or proteins in part of the body are very time consuming and have the disadvantage that they show only one ‘snapshot‘ in time. With SPECT it is possible to study the function of organs and tissue *in vivo* using radioactively labeled tracers. Moreover, the ability to monitor the same animal over a period of time is a major advantage for understanding different phases of a disease, pre-clinical testing of newly developed medicine and the development of new tracers for clinical application. Dedicated small animal SPECT systems have a high resolution and are able to detect small amounts of tracer, which means they have the potential to replace part of the standard *ex vivo* techniques.
The main subjects of this thesis are system simulation, instrumentation aspects and image reconstruction algorithms needed for the development of an ultra-high resolution SPECT system (U-SPECT). U-SPECT is dedicated for imaging small laboratory animals such as mice and rats. In addition, initial applications of the U-SPECT in biomedical research will be shown.

SPECT imaging

Single Photon Emission Computed Tomography (SPECT) is one of the most frequently used functional imaging techniques in clinical practice. Important areas where SPECT is applied include neurology, cardiology and oncology. Where other imaging modalities like X-ray Computed Tomography (CT) and Magnetic Resonance Imaging (MRI) are better suited for revealing anatomical structures, SPECT is a method *pur sang* for studying *functional aspects* of organs and cells using radioactively labeled tracers. Today, a large variety of different tracers is available, which are developed for a specific imaging task, i.e. myocardial perfusion, bone turnover and Dopamine transporters in the Brain. Many new SPECT tracers are under development.

Prior to the SPECT scan, the patient is injected with the tracer and typically after some time the tracer is accumulated at the target location. The radioactive molecules emit gamma photons which have enough energy to escape the body. These gamma photons are emitted in all directions, and they travel in straight lines when there is no interaction with the material they travel trough. One or more gamma cameras are used to detect the photons emerging from the body of the patient.

A number of projections (gamma camera images) are acquired from the patient each from a slightly different angle. Based on this projection set it is possible to reconstruct a 3D volume of the tracer distribution inside the patient using tomographic reconstruction techniques like filtered back projection or iterative image reconstruction [1]. Today, the iterative methods are commonly used since they are able to model the photon transport more accurate, which results in better image quality.

For SPECT, commonly used radio isotopes are Tc-99m, I-123, Tl-201, In-111 and Ga-67, which emit gamma photons with energies ranging from 60 to 300 keV. Most of these isotopes have a short half life (typically several hours to several days), which makes them well suited for imaging purposes.

Another form of imaging using radioactively labeled tracers is Positron Emission Tomography (PET). The principle of PET is also based on the detection of gamma photons which are able to escape from the body. However, no collimator is needed for a PET system, since a pair of gamma photons is always detected. The gamma photons are emitted simultaneously under an angle of 180 degrees as a result of the annihilation of a positron which is emitted by the tracer.

Pinhole imaging

The gamma camera is normally based on the scintillation principle in which gamma photons are first converted to visible light which can be detected by means of a (position sensitive) light detector. Most camera heads consists of a dense crystal to convert the gamma photon to visible light, a number of photomultiplier tubes (PMTs)

to detect the light and electronics to readout the PMT signals. Based on the Anger logic [2], the position where a photon hits the detector can be determined, but the direction of incidence can not. The intrinsic resolution of a gamma camera is typically around 3.5 mm Full Width at Half Maximum (FWHM).

To obtain information about the origin of the gamma photons, a collimator is mounted on top of the camera, which allows only a small fraction of the photons to pass. The collimator is made from a dense material like lead or tungsten which stops most photons, but photons which originate from a specific path can continue their path to the crystal. The most frequently used collimator for clinical SPECT is the parallel-hole collimator. It consists of a slab of lead with a large number of small parallel holes, which allow only photons perpendicular to the crystal to pass.

Another type of collimator which consists of just one hole is the pinhole collimator. It is not widely used for clinical applications, but it is the preferred type of collimator for imaging small organs and for small animal SPECT. For these small objects it has several advantages over parallel-hole collimation, which enable high resolution imaging. The projection obtained using a pinhole-collimator is always an inverted image of the original object. Moreover, the scale of the projection can be different from the original object. Figure 1 shows the projection from a parallel-hole collimator on the left and from a pinhole on the right. The size of the projection is almost independent of the distance for a parallel-hole collimator, but for the pinhole collimator the projection size is determined by the ratio: pinhole to detector distance / object to pinhole distance.

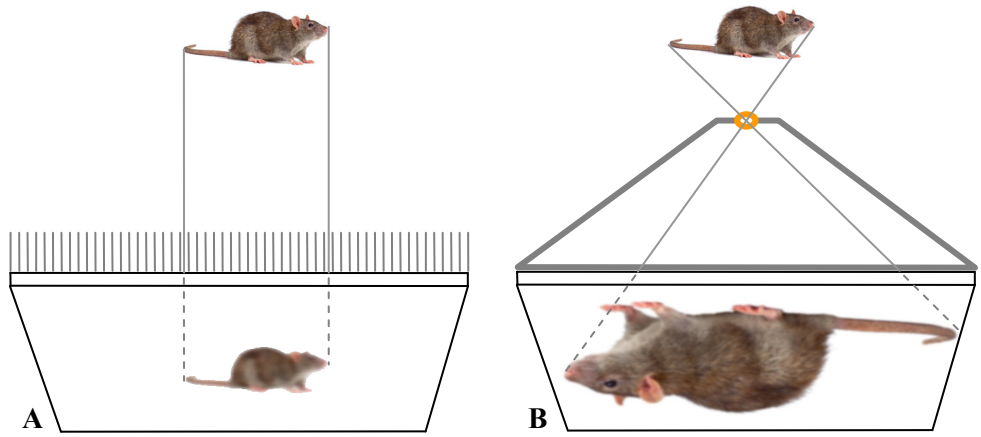

Figure 1: (A) parallel-hole projection. (B) pinhole-projection. Color figure available in appendix.

The possibility to magnify the image is an important property of this kind of collimator, since it removes the need for ultra high resolution gamma cameras and allows high resolution imaging using standard gamma cameras. A small object like a mouse or a rat can be placed close to the pinhole, while it is still possible to obtain a

highly magnified projection of the entire animal. Another advantage of pinhole-collimator is that the sensitivity (fraction of the emitted photons which are detected) is significantly higher when the object is closer to the pinhole, while for parallel-hole collimators the sensitivity is almost independent of the distance to the camera.

The size, shape and material of the pinhole are important aspects for pinhole imaging and have been studied using Monte Carlo simulations in [3] and [4]. A general overview of pinhole imaging can be found in [5].

Small animal SPECT

While SPECT was developed for clinical use, the development of small animal SPECT systems has been rapidly growing the last few years, since they are important tools to analyze mouse models of human diseases and pre-clinical testing of newly developed medicine. Some small animal SPECT systems are based on clinical cameras which are equipped with custom build collimators, others use dedicated high resolution detectors [6,7].

Pinhole collimators are commonly used for small animal imaging, since they combine the advantages of high resolution and high sensitivity. To increase the sensitivity of the system, it is possible to fit more than one pinhole to a gamma camera, but also multiple camera heads are frequently used. Further improvements to multi-pinhole systems can be obtained by focusing all pinholes on a small volume of interest to detect more photons originating from a specific location which contains the organ under investigation.

For tomographic reconstruction, a sufficient number of projections from the subject under a different angle are required. Usually, the detectors are rotated during a SPECT acquisition, but for small animals it is possible to rotate the animal instead. A special type of small animal SPECT systems have a completely stationary design, where there is no need to rotate the cameras or the animal. To achieve this, a large number of pinhole cameras are used, which surround the animal and simultaneously acquire projections from the animal at slightly different angles. These stationary systems are very well suited to perform dynamic scans with very short acquisition times.

U-SPECT

A stationary small animal SPECT system has been developed at the University Medical Center Utrecht. This machine, called U-SPECT-I, is based on a clinical SPECT system which has tree gamma camera heads. To convert the clinical system to the U-SPECT-I, a custom designed collimator tube with 75 pinholes is inserted in the center of the detectors and a XYZ stage is mounted in front of the system (figure 2A). This procedure takes about 15 minutes and no other modifications are needed, since we only use the detectors. The pinholes are mounted in the collimator tube with a

special geometry, where all pinholes focus to a small volume of interest to obtain a high sensitivity. Each pinhole projects on just a part of the detector and overlap between the pinholes is prevented by lead shielding. Because the clinical system was still in use on daily base, the first scans were performed at night. However, images with a resolution of 0.45 mm in all dimensions have been obtained using 0.6 mm pinholes, while 0.35 mm resolutions have been achieved with 0.3 mm pinholes.

More recently, a dedicated small animal system called U-SPECT-II has been developed which is based on the same design, but incorporates a large number of improvements (figure 2B). The detectors are larger than the ones used for the first generation. An exchangeable collimator design allows differently sized collimator tubes to be used. Currently, optimized collimators are available for mouse and rat imaging with a variety of pinhole diameters.

Simulation studies for a future U-SPECT-III system have been performed, where the conventional gamma camera detectors are replaced with high resolution detectors, based on a technique like CCD (Charge Coupled Device) and the total amount of pinholes is increased to 135. We expect that with such systems a much higher resolution can be obtained and that the system will more compact, but at this moment the production of such a system would be very expensive.

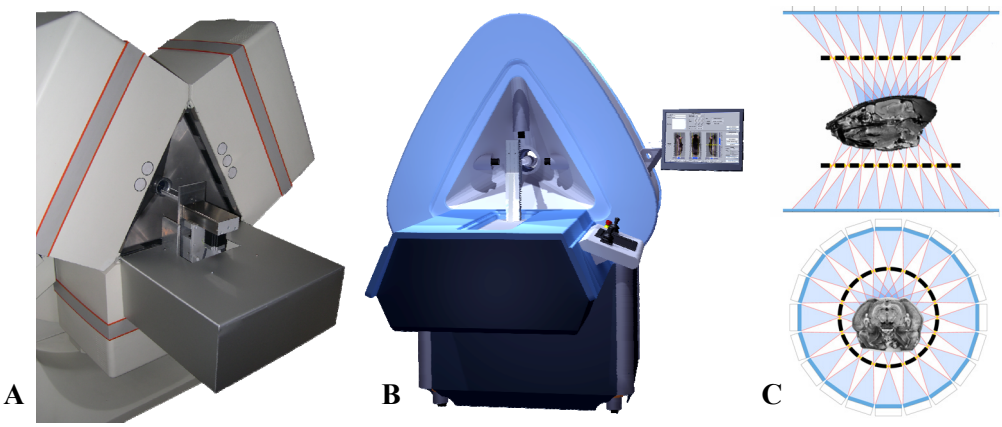

Figure 2: (**A**) U-SPECT-I (**B**) U-SPECT-II (**C**) cross sections through the U-SPECT-III geometry. Color figure available in appendix.

Image reconstruction

The image reconstruction software developed for the U-SPECT is based on an iterative statistical algorithm. One advantage of this type of reconstruction is that it is possible to accurately model the gamma photons. Interactions of the photons with the collimator, like scatter and penetration trough the edge of the pinholes can degenerate

the projection data which will result in more blurred reconstruction. Accurate modeling these effects will result in better reconstructed image quality [8,9,10].

The Maximum Likelihood Expectation Maximization (ML-EM) algorithm is the most widely used form of iterative reconstruction [11,12]. The image reconstruction is performed using an initial estimate of the activity distribution which is iteratively updated to get closer to the real (unknown) distribution. The updated activity distribution is estimated from the matrix equation: $\boldsymbol{Ma = p}$, which can also be written as a set of linear equations (figure 3). Here, $\boldsymbol{a}$ is a vector which represents the activity distribution ($\boldsymbol{a}_i$ is the amount of radioactive tracer present in a tiny volume element (voxel) i within the object), $\boldsymbol{p}$ is a vector which contains the projection data ($\boldsymbol{p}_j$ is the detector response of picture element (pixel) j of the detector), and $\boldsymbol{M}$ is the matrix that projects the activity distribution onto the detectors. The matrix elements $\boldsymbol{M}_{ji}$ represent the probability that photons emitted by an amount of tracer in voxel i are detected in pixel j of the detectors.

$$
\begin{array}{llllll}
M_{11}\,a_1 & + M_{12}\,a_2 & + M_{13}\,a_3 + & \ldots & + M_{1x}\,a_x & = p_1 \\
M_{21}\,a_1 & + M_{22}\,a_2 & + M_{23}\,a_3 + & \ldots & + M_{2x}\,a_x & = p_2 \\
M_{31}\,a_1 & + M_{32}\,a_2 & + M_{33}\,a_3 + & \ldots & + M_{3x}\,a_x & = p_3 \\
\vdots & \vdots & \vdots & \vdots & \vdots & \vdots \\
M_{y1}\,a_1 & + M_{y2}\,a_2 & + M_{y3}\,a_3 + & \ldots & + M_{yx}\,a_x & = p_y
\end{array}
$$

Figure 3: Set of linear equations used in iterative image reconstruction.

During iteration k of the reconstruction process, an estimate projection $\boldsymbol{p}^k$ is simulated based on the current activity distribution $\boldsymbol{a}^k$. Then, an error projection is generated using the relative difference between $\boldsymbol{p}^k$ and the measured projection $\boldsymbol{q}$. This error projection is used to make an error map for the activity distribution. The error map is applied to $\boldsymbol{a}^k$ in order to generate an updated activity distribution $\boldsymbol{a}^{k+1}$ which, based on the measured projections will be more likely. During the next iteration $\boldsymbol{p}^{k+1}$ is generated based on $\boldsymbol{a}^{k+1}$, and this scheme is repeated many times to obtain a good estimate for the activity distribution. A schematic diagram of the iterative reconstruction is shown in figure 4.

The principle behind the iterative reconstruction is based on the fact that when $\boldsymbol{p}^k$ is a good estimate of measured projection $\boldsymbol{q}$, then $\boldsymbol{a}^k$ is likely a good estimate of the real activity distribution. A uniform distribution is often used as a start value for $\boldsymbol{a}^0$.

To speedup the convergence of the iterative process, acceleration schemes are available like Ordered-Subset Expectation-Maximization (OS-EM) [13]. A more detailed explanation on iterative SPECT reconstruction can be found in [1].

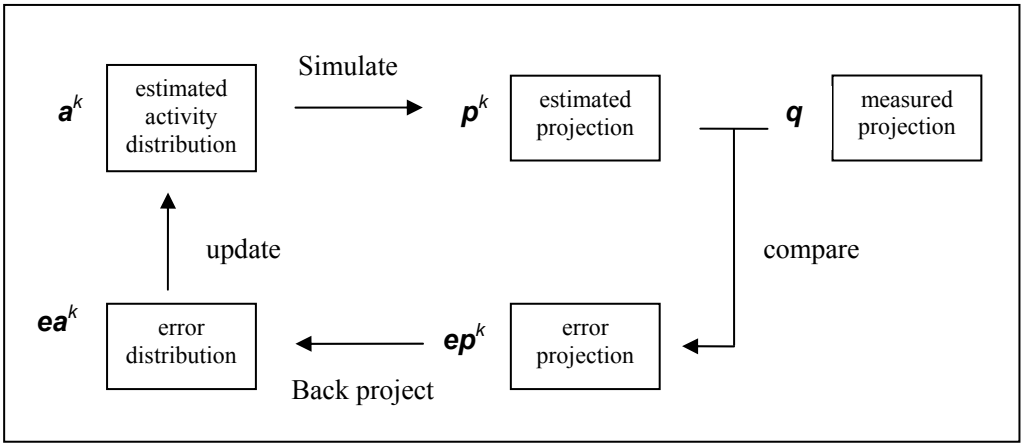

Figure 4: schematic diagram of the iterative reconstruction.

Thesis outline

This thesis is associated with simulation, construction, development and initial applications of a small-animal SPECT system called U-SPECT. The first chapter is a general introduction to SPECT, small animal imaging and image reconstruction, and chapter two covers the design and implementation of the first generation U-SPECT. Like most other small-animal SPECT devices, U-SPECT systems use pinhole collimation. Compared to other pinhole SPECT systems, the U-SPECT system uses a higher number of pinholes and a more focusing geometry. To obtain images at a sufficient number of angles most other pinhole SPECT systems use rotation of the collimator and detector with respect to the animal. U-SPECT systems are stationary, obtaining all angular information from the different projection angles of the pinholes. Other distinguishing features of U-SPECT are that the projections on the detector from different pinholes are made non-overlapping and very high magnification factors are used to achieve a very high image resolution.

The first prototype small-animal SPECT system that was built in Utrecht was called U-SPECT-I. This machine was constructed based on an existing clinical SPECT system with 3 gamma camera detectors, which was still in use in the clinic. After removal of the clinical collimators, a frame with a cylindrical pinhole collimator tube, various shielding parts, as well as a XYZ robotic stage, would be mounted onto the SPECT system. This would temporarily transform the clinical system to the hardware used for the U-SPECT-I system. Chapter 2 presents U-SPECT-I as a complete system. The performance in terms of achievable resolution and sensitivity are characterized and also the results from measurements with mice are shown.

The image reconstruction software of U-SPECT is based on an iterative statistical algorithm. For this type of reconstruction, a method to simulate the detector response for a known activity distribution is required, which is given by the system matrix. Accurate modelling of the gamma photons and the detector response in this

matrix is important to obtain good reconstructed images. This means that the determination of the matrix elements becomes one of the more crucial steps in the development of the SPECT system. Chapter 3 presents a method that was developed to obtain the system matrix which is based on point source measurements. We show the influence of changing certain parameters in the creation of the system matrix on the resulting reconstructed images.

With the highly focused design of the U-SPECT-I, sub millimeter images were obtained initially for only a limited volume of interest, for instance the heart or the brain of a mouse. Even with these highly focused systems it is possible to scan a volume of interest which is lager than the field-of-view of the system. This is accomplished by translating the animal trough the focus of the scanner and using specially adapted reconstruction methods, which is discussed in chapter 4 of this thesis. The method is validated using simulation studies, physical phantom experiments as well as total-body *in vivo* mouse imaging.

Development did not stop with the U-SPECT-I system. A next generation system was designed and developed, called U-SPECT-II which is now marketed by the UMC Utrecht Spin-off company MILabs. U-SPECT-II can be used for imaging both mice and rats. It has a significantly larger detector surface than U-SPECT-I and its detectors have fully digital electronics. The data is read out in list mode, providing energy discrimination capabilities and multi-isotope imaging, as well as gated imaging. Furthermore, it has an automated method to expand the field-of-view up to total body imaging. The design, development and initial measurements and tests to characterize the performance of the U-SPECT-II are described in chapter 5.

A potential problem with highly focused pinhole systems is that the field-of-view is often small, which makes it difficult to define the volume-of-interest to be scanned. Accurate selection of the organ will maximize sensitivity from the selected region which results in better resolution and lower noise. In Chapter 6 we propose and validate a new tool for optimizing the performance and conveniently and accurately selecting the volume-of-interest for focusing pinhole SPECT systems using optical cameras and a specially designed graphical user interface.

A pivotal question in neuropharmacology is how the function of neurotransmitter systems relates to psychiatric diseases. Analysis of animal models has been limited by the availability of methods to study *in vivo* neurotransmitter dynamics. In chapter 7 we show how U-SPECT can localize dopamine transporters in sub-compartments of the mouse brain during a range of points in time. Applied to the midbrain dopamine system of different models of disease, we expect that this will aid the understanding of dynamic processes of this neurotransmitter that underlie brain functions and human brain pathology.

In chapter 8 we simulate a next generation of U-SPECT: the U-SPECT-III. In this system low resolution detectors based on high voltage tubes will be replaced by solid state detectors like CCD's (charge-coupled device). We expect that with such systems a much higher resolution can be obtained and that the system will be more compact. This thesis concludes with a summary.

References

[1] Bruyant PP, 'Analytic and iterative reconstruction algorithms in SPECT', *J. Nucl. Med.* 2002; 43: 1343–1358.

[2] Anger HO, 'Scintillation Camera', *Rev. Sci. Instr.* 1958: 27-33.

[3] van der Have F and Beekman FJ, 'Photon penetration and scatter in micro-pinhole imaging: a Monte Carlo investigation', *Phys. Med. Biol.* 2004; 49: 1369-1386.

[4] van der Have F and Beekman FJ, 'Penetration, scatter and sensitivity in channel micro-pinholes for SPECT: a Monte Carlo investigation', *IEEE Trans. Nucl. Sci.* 2006; 53: 2635-2645.

[5] Beekman FJ and van der Have F, 'The pinhole: Gateway to ultra-high resolution three-dimensional radionuclide imaging', *Eur. J. Nucl. Med. Molec. Im.* 2007; 34: 151-161.

[6] King MA, Pretorius PH, Farncombe T, Beekman FJ, 'Introduction to the physics of molecular imaging with radioactive tracers in small animals', *J. Cell. Biochem.* 2002; Suppl. 339, 221–230.

[7] Meikle SR, Kench P, Kassiou M, Banati RB, 'Small animal SPECT and its place in the matrix of molecular imaging technologies', *Phys. Med. Biol.* 2005; 50: R45-R61.

[8] Floyd CE, Jaszczak RJ, Greer KL, Coleman RE, 'Inverse Monte Carlo as a unified reconstruction algorithm for ECT', *J. Nucl. Med.* 1986; 27: 1577-1585.

[9] Beekman FJ, Kamphuis C, Frey EC, 'Scatter compensation methods in 3D iterative SPECT reconstruction: A simulation study', *Phys. Med Biol.* 1997; 42: 1619-1632.

[10] Kadrmas DJ, Frey EC, Karimi SS, Tsui BMW, 'Fast implementation of reconstruction based scatter compensation in fully 3D SPECT image reconstruction', *Phys. Med. Biol.* 1998; 43: 857-873.

[11] Shepp LA, Vardi Y, 'Maximum likelihood reconstruction for emission tomography', *IEEE Trans. Med. Imaging.* 1982; 1: 113-122.

[12] Lange K, Carson R, ‘E.M. Reconstruction algorithms for emission and transmission tomography’, *J. Comput. Assist. Tomo.* 1984; 8: 306–316.

[13] Hudson HM, Larkin RS, ‘Accelerated image reconstruction using ordered subsets of projection data’, *IEEE Trans. Med. Imaging.* 1944; 13: 601-609.

Chapter 2

U-SPECT-I: A Novel System for Submillimeter Resolution Tomography with Radiolabeled Molecules in Mice

Freek J. Beekman, Frans van der Have, Brendan Vastenhouw, Annemarie J. A. van der Linden, Peter P. van Rijk, J. Peter H. Burbach and Marten P. Smidt

The Journal of Nuclear Medicine, 2005; 46: 1194-1200.

Abstract

A major advance in biomedical science and diagnosis was accomplished with the development of *in vivo* techniques to image radiolabeled molecules, but limited spatial resolution has slowed down applications to small experimental animals. Here we present a Single Photon Emission Computed Tomography system (U-SPECT-I) dedicated for radionuclide imaging in murine organs at the sub-mm resolution level. **Methods:** The basis for the high performance of U-SPECT-I is provided through a static triangular detector set-up, with a cylindrical imaging cavity in the center and the application of 75 gold micro-pinhole apertures placed in the cavity wall. The pinholes are focused to a small volume-of-interest such as the mouse heart or spine in order to maximize the detection yield of gamma-photons. Using the detector data, 3D molecule distributions are iteratively estimated using a statistical reconstruction algorithm that takes into account the system blurring and data noise in order to increase resolution and reduce image noise. **Results:** With 0.6 mm diameter pinholes, the maximum fraction of detected photons emitted by a point source (peak sensitivity) is 0.22 % for a 15 % wide energy window and remains higher than 0.12 % in the central 12 mm of the central plane. In a resolution phantom, radioactively filled capillaries as small as 0.5 mm and separated by 0.5 mm, can be distinguished clearly in reconstructions. Projection data needed for the reconstruction of cross-sections of molecule distributions in mouse organs can be readily obtained without the need for any mechanical movements. Images of a mouse spine show Tc-99m-hydroxy-methylene diphosphonate uptake down to the level of tiny parts of vertebral processes. These are separated clearly from the vertebral and inter-vertebral foramens. Using another tracer, myocardial perfusion in the left and right ventricular wall, even in structures as small as the papillary muscles, can be monitored. **Conclusion:** U-SPECT-I allows for discriminating between molecule concentrations in adjacent volumes as small as about 0.1 micro-liters, which is significantly smaller than any existing SPECT and Positron Emission Tomography (PET) system. Our initial *in vivo* images of the mouse heart and spine show that U-SPECT-I can be used for novel applications in the study of dynamic biological systems with a clear projection to clinical applications. The combination of high resolution and detection efficiency of U-SPECT-I opens up new possibilities for the study with radio-tracers in mouse models at the sub-organ level.

Introduction

Dedicated Single Photon Emission Computed Tomography (SPECT) and Positron Emission Tomography (PET) instruments [1] in concert with the radiolabeling of small molecules, antibodies, peptides, and probes for gene expression

have facilitated *in vivo* assessment of molecular mechanisms and the development of new tracers and pharmaceuticals [2-6]. Recent developments in this multi-disciplinary field of molecular imaging have initiated a revolution in biomedical sciences. A bottleneck in the assessment of molecular mechanisms at the sub-organ scale is the limited spatial resolution of available SPECT and PET instruments. In practice, the resolution in living animals is presently limited to tissue volumes of about one micro-liter (e.g. [7]) but often an order of magnitude larger. The increasing availability of genetically modified mice as models for human disease prompt for studies with SPECT and PET. However, improving image resolution and dynamic capabilities is essential to fully exploit disease models and tracers available.

SPECT systems employing pinhole ”lenses” permit radiolabeled molecule distributions to be imaged *in vivo* in small animals. Several small pinhole SPECT systems have been designed and constructed in recent years [8-14]. In addition to SPECT systems, dedicated small animal PET systems have been devised for the imaging of radiolabeled molecules [15]. The small animal versions of SPECT and PET are often referred to as micro-SPECT and micro-PET. The applications of SPECT and PET partly overlap and are often complementary. The method that is used for a particular application depends on matters such as equipment costs, infrastructure, required resolution and counting sensitivity and will also be influenced by logistics, costs and the availability of the specific radio-molecules required.

With micro-pinhole radio-nuclide imaging it becomes possible to obtain high spatial resolution projection data, particularly in small organs that can be positioned closely to the pinhole. For example, it has been shown experimentally that the thyroid of a living mouse (typical size 1×1 mm), can be imaged at a resolution as good as 0.2 mm using planar pinhole cameras [16]. However, a drawback of contemporary pinhole SPECT compared to PET is the limited ability to detect a good fraction of the emitted gamma-photons. This counting sensitivity is decreased even further when smaller pinholes are used to push high image resolution. With low counting sensitivity the high resolution information content of projection data cannot be fully exploited since reconstructed volumes calculated from these projections tend to be very noisy and visual interpretation is only possible after resolution degrading smoothing operations. This often results in a resolution that is significantly worse than that of images obtained with micro-PET.

The goal of this chapter is the launching of a dedicated mouse SPECT system (U-SPECT-I) that defines a new front line of micro-SPECT characteristics, through a design that enables one to exploit the high resolution content of pinhole projection data. U-SPECT-I is stationary in the sense that there is no need for moving any of the parts such as the detector and the collimator, or the animal. This has advantages for (i) system stability, (ii) simplicity of the system design, and (iii) flexibility to perform dynamic studies with any frame-time [14,17,18], and (iv) animal handling and positioning. In addition, U-SPECT-I is designed in such a way that all pinholes focus on a small area. In this way a specific object area is adequately magnified on the

detector plane, while only a limited part of the detector surface available is required for creating each mini-camera. All these independent mini-cameras together result in a significant higher sensitivity, thus overcoming a fundamental problem of micro-pinhole imaging. The system is based on conventional scintillation gamma cameras that are part of a clinical SPECT system (Picker 3000 S) and has the flexibility to be switched back rapidly to the original clinical imaging set-up. Validation of the system design and its outstanding imaging characteristics are demonstrated through imaging of specific phantoms and mouse organs.

Materials and Methods

In this section we describe the U-SPECT-I system geometry (composition and positioning of pinholes and detectors), the image reconstruction methods used, the physical phantom experiments performed, as well as the animal experiments that were used to prove the system performance.

Pinhole design and geometry of U-SPECT-I

Figure 1A shows an overview of the U-SPECT-I system, where the detectors of a triple head SPECT system (with clinical collimators removed) are used as a ”detector ring”. A cylinder with 75 gold pinholes is placed in the center (Figure 1B). The pinhole apertures are placed in a five fold ring geometry, each ring containing 15 pinhole apertures. The gold pinhole apertures have high photon stopping power compared to commonly used lead or tungsten, thus reducing blurring caused by radiation penetration and scattering in the aperture edge material [19]. In contrast with earlier proposed depleted uranium, which has an even better stopping power, gold pinholes can be manufactured quite easily in high quantities, and are not radio-active or poisonous. The high photon-counting sensitivity obtained with the high number of pinholes can be traded for increased image resolution by the use of relatively small pinholes (0.6 mm diameter). The pinholes have knife edges and an opening angle of 30 degrees with shielding placed in such a way that projections do not overlap (figure 2A). The shielding consists of a lead tube with square holes defining the edges of the projections (figure 2B).

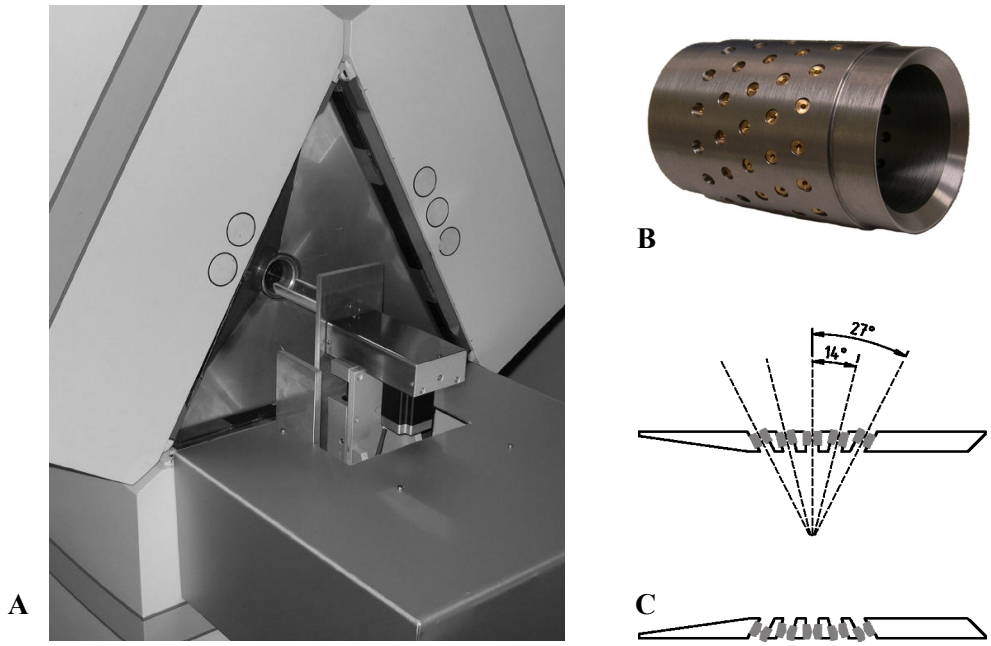

Figure 1: (A) overview of the U-SPECT-I system. Triangular shaped lead shielding is placed in between the camera heads of the triple detector system, the tungsten cylinder containing pinholes being placed in the center of the three detectors. The XYZ-stage with attached bed, placed in front of the lower detector, is also visible. (B) Cylinder with 75 gold pinhole apertures focused on the center of the cylinder. (C) Cross-section of cylinder with tilted pinholes. Color figure available in appendix.

A cross section through the detector and the central ring with pinholes is shown in Figure 2A. The edges of the 15 photon beams passing through the 15 pinholes in this ring are indicated by lines that diverge from the individual pinholes towards the detector and towards the central area of the cylinder. The pinholes in different rings are all focused on the center. The apertures in the outer rings are placed at a larger angle to the trans-axial axis. In this way, voxels in the central field-of-view can be observed via 69 pinholes simultaneously (six of the 75 pinhole cameras are partly or completely blind because of missing active crystal area close to the camera edges in the corners of the triangle). The pinhole positions in adjacent rings are rotated over eight degrees in order to increase the variety of angles at which each voxel is observed. The projections of the object area observed by different pinholes do not overlap. Overlap is prevented by placing a lead tube with 75 rectangular holes around the tungsten pinhole cylinder. The diameter of the rings with pinholes is 44 mm when measured at the centers of the pinhole openings. The intrinsic resolution of the gamma cameras was measured with a line-shaped beam (140 keV) to be 3.2 mm Full-Width-of-Half-Max.

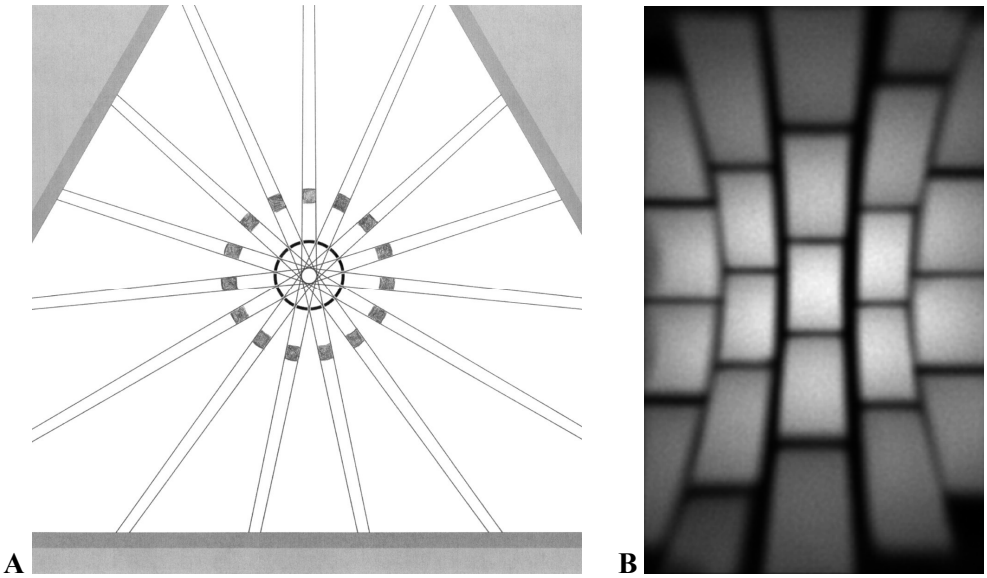

Figure 2: Illustration of the highly focusing pinhole geometry of U-SPECT-I. A cross section through one of the five rings with pinholes is shown in Frame A. Lines emerging from the central circle mark the triangular cross sections of beams in which emitted gamma quanta can travel from the animal towards the detector. Pinholes in all rings focus on the center in order to maximize detection yield. A lead cylinder with square holes shown in grey is placed around the tungsten cylinder with pinholes to prevent projection overlap. In Frame B the radiation intensity on one of the three detectors is displayed when a bottle with a Tc-99m solution is imaged. It demonstrates how the large detector is divided into a large number of small sub-cameras.

Image reconstruction and calibration

Image reconstruction for U-SPECT-I was performed using 150 iterations Maximum Likelihood Expectation Maximization (ML-EM, [20]). Point spread functions (PSFs) of the system are used during ML-EM reconstruction to model the probabilities that a photon from a certain object position will be detected in a specific detector pixel. PSFs were measured using a 60 MBq point source. The point source is produced from a chromatographic bead, which has the size of one voxel approximately. Small amounts (10 to 15 µl) of concentrated (approx. 4 GBq/ml) pertechnetate are added 10 to 15 times and the liquid evaporates by heating to about 60 degrees C. The point source is attached to its holder by a fast-curing epoxy resin.

Each PSF is part of the transition matrix which is entirely stored on disk. Because entire PSFs are taken into account during reconstruction instead of assuming a line integral through the center of each pinhole, the effects of blurring due to

pinhole diameter and pinhole penetration as well as intrinsic detector blurring are corrected for during reconstruction. Another advantage of directly measuring the PSFs is that it obviates the need for (i) separately calibrating mechanical (detector and collimator) and electronics offsets, and (ii) uniformity and linearity corrections.

The measured PSFs over all voxels in the cylinder together represent the entire system matrix that is needed during iterative reconstruction of the image. A similar method has been used to calibrate the Fast-SPECT system at the University of Arizona [18]. With the U-SPECT-I system, the voxel size used in reconstructions is very small (0.1875 mm). The projection pixel size used for all measurements reported in this chapter was 0.898 mm. Since it would be very time consuming to measure the PSF for each voxel position in the pinhole cylinder separately, we measure the PSF in a subset of voxels in the object using an *x, y, z* stage and a grid of 7 × 7 × 11 points with a spacing of 3 mm, 3 mm and 1.5 mm, respectively. For each measured PSF we first estimate four basic properties: the coordinates of the maximum on the detector, the flux, and the width. Using linear interpolation and extrapolation the properties of the missing PSFs are estimated and stored.

Study of system characteristics

Position-dependent point-source sensitivity in the collimator ring was measured using the same scanning point source as used for system calibration. Sensitivity profiles presented in Figure 3 were acquired over three mutually perpendicular axes, each crossing the center of the field-of-view, and were obtained with a 15% energy window.

A miniature acrylic resolution phantom (”Derenzo phantom”) was manufactured. It contains six sectors with equally-sized sets of capillaries (0.4, 0.5, 0.6, 0.7, 0.8, and 1.0 mm) within each sector. Each capillary is 10 mm long, the total activity in all capillaries together was 11.1 MBq Tc-99m, and the data acquisition time was 30 minutes. The distance between the rods equals the rod diameter. The phantom diameter is 12 mm. The spatial resolution in such phantoms is often defined by the size of capillaries that can be observed separately.

Animal studies

Animal studies were conducted following protocols as approved by the Animal Research Committee of the University Medical Center Utrecht. Three-months-old C57BL/6JO1aHsd mice (Harlan, The Netherlands, 25-30 g) were anesthetized with a mix of 2.5 ml/kg Hypnorm (Janssen, fentanyl 0.315 mg/ml and fluarisone 10 mg/ml), 2.5 ml/kg dormicum (Roche; midazolam 5 mg/ml) and 5 ml/kg aquadest i.p.. Thereafter the radio-nuclide of interest (0.2 ml solution) was injected into the tail vein. Radio-nuclides tested were Tc-99m hydroxy-methylene diphosphonate (Tc-99m-HDP) for bone imaging and Tc-99m tetrofosmin for cardiac perfusion imaging. During the entire procedure the animal body temperature was kept at 37 degrees Celsius.

Results

Ultra-high system sensitivity and image resolution

Sensitivity, here expressed in the percentage of emitted gamma quanta that are detected, depends on the pinhole diameter, the number of pinholes and the distance of the pinholes to the object [21, 22]. The peak sensitivity with 0.6 mm pinholes was measured to be 0.22 % in the central field-of-view and remains 0.12 % within a central trans-axial disc with a 12 mm diameter (Figure 3). Sensitivities of other small animal SPECT systems are typically more than an order of magnitude lower when compared at equal geometrical system resolution, because of a low number of pinholes or the less focusing architecture. High sensitivity is crucial to avoid noisy data and therefore avoids excessive resolution degrading low-pass filtering operations for enhancing visual appearance of otherwise noisy reconstructed images. For any pinhole system, the sensitivity can be increased at the cost of system resolution, by enlarging the pinholes.

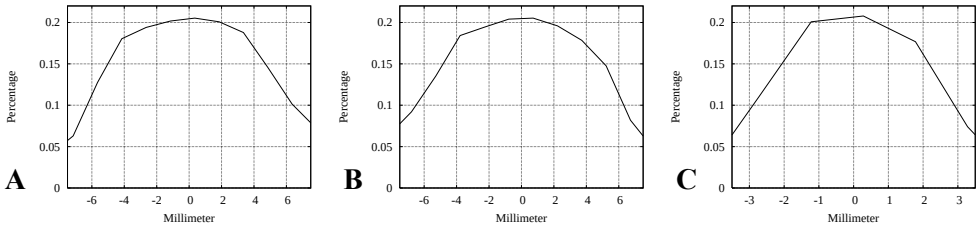

Figure 3: Demonstration of the high sensitivity of U-SPECT-I. Sensitivity profiles along mutually orthogonal lines that cross the center of the field-of-view, obtained with a scanning point source. Profile (A) is lying along the x-axis, (B) along the y-axis, and (C) along the trans-axial axis (z-axis).

Imaging of miniature resolution phantom during 30 minutes resulted in reconstructions clearly resolving the set of 0.5 mm capillaries (Figure 4). Even some of the 0.4 mm capillaries could be identified. This result indicates that differences in molecule uptake between tiny neighboring tissue volumes in the order of 0.1 micro-liter can be readily distinguished. Note that the smallest capillaries resolved with state-of-the-art PET scanners are approx. one mm [7] when advanced statistical reconstruction is applied.

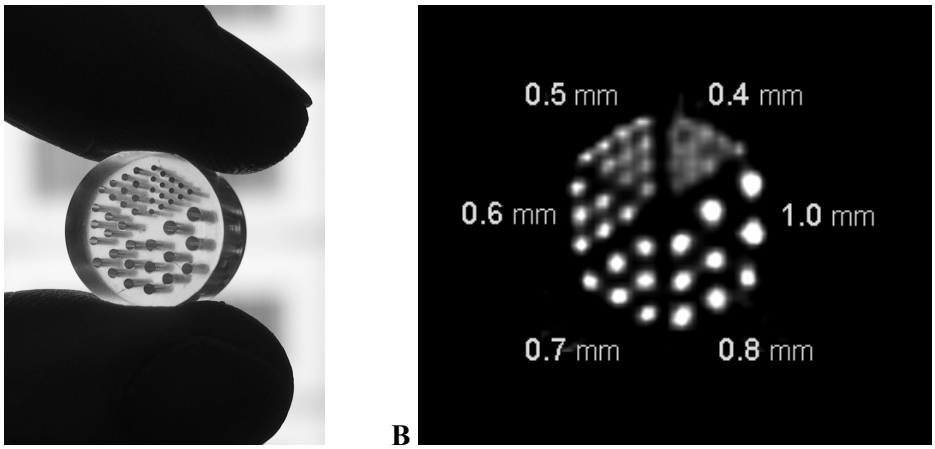

Figure 4: Demonstration of sub-mm resolution of U-SPECT-I images. (A) Photograph of miniature acrylic resolution phantom with capillaries used as test object. (B) Reconstructed cross sectional images with a slice thickness of 0.5 mm of the phantom shown in (A). The 0.5 mm capillaries are clearly separated in the image.

Ultra-high resolution images of radio-molecules in the living mouse

To show that highly detailed imaging can be extrapolated from test objects to living animals, we acquired images in mice with two different tracers often used in clinical SPECT studies. Figure 5 shows three perpendicular cross sections of a myocardial perfusion volume image obtained with Tc-99m-tetrofosmin. Myocardial perfusion in both the left and right ventricular wall is clearly visible. Perfusion in the anterior papillary muscle within the left ventricle was readily distinguished in the short-axis slice (arrow). The level of detail presented here may lead to new experimental opportunities in cardiology.

A second experiment was performed to show bone metabolism within a mouse lumbar spine (Figure 6). Frame (A) shows three orthogonal slices through the spine, with a slice thickness of 0.25 mm. A projection of local image maxima (maximum intensity projections, left) and iso-surface renderings of tracer concentrations (right), calculated from the same reconstructed 3D tracer distribution (Frame B). Tc-99m-HDP-uptake in tiny parts of the individual processes and other tiny vertebral parts was readily visualized. Also, the spaces between and in the vertebrae, the intervertebral foramen and vertebral foramen, that do not take up HDP were clearly distinguished from bone tissue, particularly in the iso-surface renderings. Since uptake of HDP-like agents is very much influenced by changes in bone remodulation, such as caused by mechanical strain or tumor growth, the type of detailed imaging shown here may initiate new research opportunities in locomotion, bone, and cancer research.

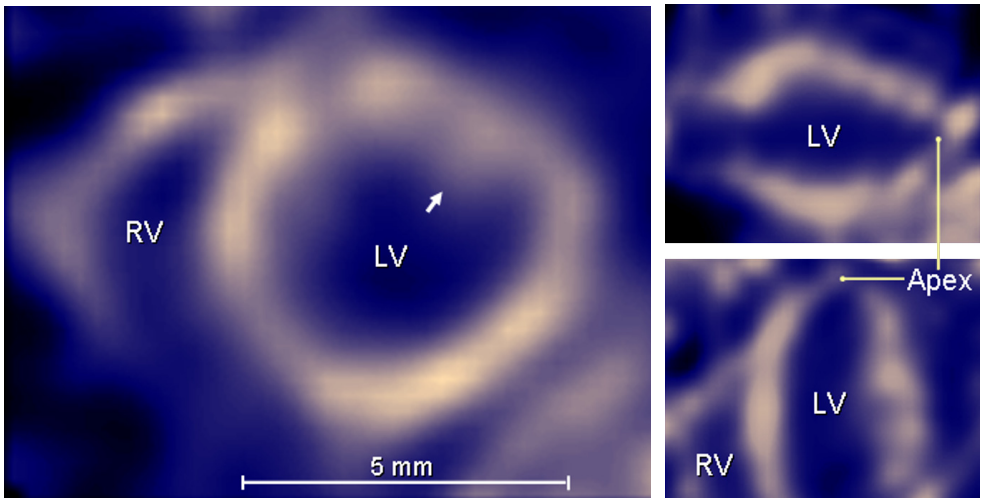

Figure 5: Mutual perpendicular cross sections through a sub-mm resolution 3D myocardial perfusion image volume of the living mouse (Animal co-image of the year, Society of Nuclear Medicine, Philadelphia 2004). Image data was acquired during 30 minutes, starting 30 min after administration of 222 MBq (6 mCi) Tc-99m-tetrofosmin. Left frame: short-axis slice shows myocardial perfusion in the right ventricular (RV) and left ventricular (LV) wall. Perfusion in the anterior papillary muscle (arrow) can be distinguished from the other parts of the left ventricular wall. Top right: vertical long-axis slice. Bottom right: horizontal long-axis slice. Color figure available in appendix.

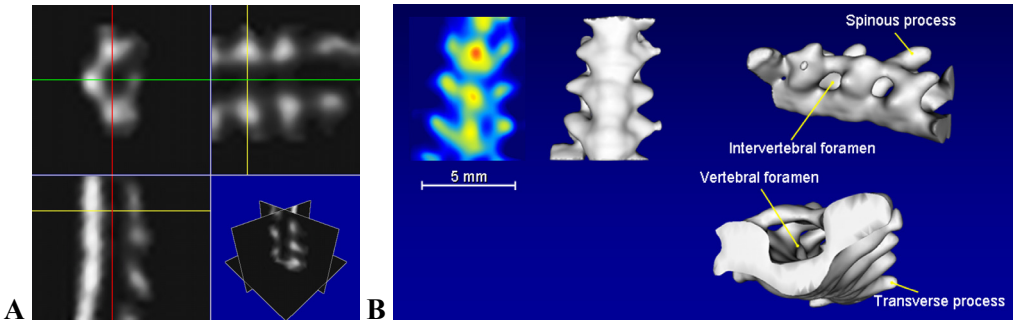

Figure 6: Different representations of a reconstructed image volume of the lumbar spine, acquired during 22 minutes, two hours after the injection of 148 MBq (4 mCi) Tc-99m-HDP. Frame (A) shows three different orthogonal cross-sections. In Frame (B) both a projection of local image maxima (upper left) and three iso-surface renderings of tracer concentrations in the same spinal section are displayed (Animal co-image of the year, Society of Nuclear Medicine, Philadelphia 2004). Color figure available in appendix.

Discussion

In this chapter we have described a new SPECT system that has a highly focused pinhole architecture resulting in high-resolution molecular imaging. Even with standard detectors with an intrinsic resolution of 3.2 mm, SPECT images with a resolution better than 0.5 mm were obtained, without the optimizing of pinhole diameters yet. U-SPECT-I, and its successors with an even higher resolution, will allow the three-dimensional assessment of distributions of a wide range of radio-labeled tracers. Labor intensive *in vitro* or *ex vivo* methods may be replaced in several cases by the imaging of intact animals on the sub-millimeter level. This will also allow for accurate longitudinal study designs, instrumental for development of new diagnostic or therapeutic agents. Importantly, U-SPECT-I allows non-invasive imaging in mice with radionuclides and associated radiomolecules of which many are already approved for clinical use. On the other hand, novel imaging applications and tracer biology developed in mice can be readily translated into clinical application where radionuclide imaging methods such as SPECT are already in common use.

The present U-SPECT system has an outstanding sensitivity/resolution trade-off, with a field-of-view that is large enough to cover most essential mouse organs, like the entire mid-brain, the mouse heart or the lumbar spine. Often only small fields-of-view are required. The advantage of the focusing set-up is that one can acquire many photons from a specific area of interest. As we have shown, this helps to produce a high image resolution. It is possible to extend the field-of-view without changing the pinhole geometry: the bed has then to be shifted in order to focus the pinholes on different areas of the animal. As a result, the area with highest sensitivity scans through the volume-of-interest in the animal. The most trivial way to extend the field-of-view is to stitch the smaller images calculated from separate acquisitions together, as is often done in clinical procedures. However, we have devised a more promising solution, which consists of a combined reconstruction and acquisition strategy that simultaneously takes into account all projection data from different bed positions and produces the entire image volume from a single reconstruction [23]. With this method, it may be possible to extend the useful field-of-view to the entire central nervous system of a mouse by using no more than two bed positions. Positions can be alternated sufficiently rapidly by shifting the tiny bed back and forth instead of the heavy detectors. This will enable dynamic studies with an extended field-of-view.

Another way to extend the field-of-view of the U-SPECT system is the removal of the cylindrical shielding between the pinholes and the detector (figure 2A). This will result in a certain amount of overlap of the projections that depends on the shape of the pinholes, such as the opening angle and edge-type. Systems with overlapping projections (e.g.[30,31]) have another interesting feature: they can detect a larger fraction of the emitted photons, while activity that is concentrated in very small areas like small tumors can still be projected on separate areas on the detector. On the other hand, for extended distributions that are more common in biology, the overlap of

patterns on the detector will lead to significant information loss about the emission direction of each detected gamma-quantum. Whether the increase in detection probability obtained by overlap will compensate for such an information loss strongly depends on the specific distribution of the molecules to be imaged, on the amount of projection overlap and the number of detected photons. These will be important factors determining if the same increase of sensitivity might be better obtained by using larger pinholes instead of more pinholes combined with allowing overlap. Comparisons of the image quality of systems with overlapping projections and with non-overlapping projections will be a research subject of continuing interest. In addition, several novel (hybrid) projection strategies are currently developed in our lab.

An important cause for the low sensitivity of previously proposed pinhole SPECT systems is that the gamma detection depends on traditional Anger scintillation cameras with a typical intrinsic resolution of approx. 2.0 – 4.0 mm. Higher resolution detectors are still extremely expensive if they are required to cover a large area. The problem of limited detector resolution is bypassed with pinhole SPECT, through the application of a significant magnification of the animal via the pinhole on the detector. For adequately magnified projection of a large part of the animal, one needs a large detector surface area. This is why in almost all systems only a few pinhole cameras are placed around the animal; more pinholes would cause overlapping of the projections. With a few pinholes, the resulting bulky cameras need to be rotated in order to obtain projections at a sufficient number of different angles. The required mechanics complicate these SPECT systems and makes them difficult to calibrate. In addition, systems requiring detector rotation have only limited flexibility to acquire and process dynamic series.

The design of U-SPECT allows for stationary acquisition of projection data similar to the FastSPECT system [18] and PET systems. Together with the high sensitivity achieved with the high number of pinholes, U-SPECT will enable researchers to perform dynamic studies in mice; users will have a greater flexibility to choose frame time a posteriori. Additionally, the design without moving parts will reduce maintenance requirements and may simplify system calibration.

Previously performed simulation studies [14] of stationary micro-SPECT devices have shown that better resolution detectors will enable significant improvements over the results presented here, and that the focused pinhole geometry with non-overlapping projection views brings us closer to satisfying the Orlov conditions for adequate sampling of data [24] than traditional pinhole SPECT systems and that this is important for producing better results than is possible with traditional pinhole SPECT systems which acquire projections over a single orbit.

U-SPECT-I is based on the use of the triangular scintillation detector set-up ”borrowed” from a system that is currently still in use for routine clinical SPECT scanning. The entire transformation from U-SPECT-I back to a clinical system takes about 10 minutes, and no extra calibrations are required between the switching from clinical to animal imaging device. Therefore, the U-SPECT design is extremely cost-

effective and can be universally applied to clinical SPECT systems. Ultimately however, stationary SPECT systems may comprise of a detector ring or a spherical layer (a sphere concluded by two planes), approximated by a polygon that is formed by high-resolution detectors, such as in the U-SPECT-III design [14]. High-resolution detectors are under development in several groups (e.g., [25-29]). A next step in U-SPECT evolution will be the application of such detectors.

U-SPECT-III was already tested in simulations, but the costs and availability of detectors are presently restricting factors. Simulation results point to marked progress in small animal SPECT instrumentation over the next couple of years.

Conclusion

U-SPECT-I defines a new front line in micro-SPECT imaging. It is a fully functional, dedicated animal SPECT system with an outstanding volumetric resolution of the order of 0.1 µl. Results indicate that U-SPECT-I provides a significant resolution improvement over state-of-the-art small animal SPECT and PET systems. The system allows for assessing tracer dynamics in sub-organs of the living mouse, as was illustrated by *in vivo* images showing sub-mm details of molecular uptake in the myocardium and vertebrae.

The high resolution, high sensitivity and relatively low hardware costs of U-SPECT-I should now allow detailed molecular imaging to be applied successfully to a wide range of study types, thus creating a broad range of new experimental opportunities. Significant improvements in image quality are expected when the triangular detector set-up of U-SPECT will be replaced by high resolution detectors.

Acknowledgments

This work was sponsored by the Medical Council of the Netherlands Organization for Scientific Research, grant 917.36.335. We thank Dr. Lars Furenlid for showing us how to make concentrated point sources and Dr. Simon Cherry for introducing FB to the micro-imaging world. Gijs van der Wilt, Cees van der Linden, Henk te Biesebeek, Jan Brakkee and Cora de Bruijn are thanked for technical assistance. Dr. Theo van Walsum is thanked for assistance with image display.

References

[1] King MA, Pretorius PH, Farncombe T, Beekman FJ, ‘Introduction to the physics of molecular imaging with radioactive tracers in small animals’ *J. Cell. Biochem*. 2002; suppl. 39: 221–230.

[2] Gambhir SS, Herschman HR, Cherry SR, et al., ‘Imaging transgene expression with radionuclide imaging technologies’ *Nature Neoplasia*. 2000; 2(1): 118–138.

[3] Phelps ME, 'Inaugural article: positron emission tomography provides molecular imaging of biological processes' *Proc. Natl. Acad. Sci. USA*. 2000; 97: 6226–6233.

[4] Weissleder R, 'Scaling down imaging: molecular mapping of cancer in mice' *Nature Rev. Cancer*. 2002; 2(1): 11–18.

[5] Rudin M, Weissleder R, 'Molecular imaging in drug discovery and development' *Nature Rev. Drug Discov*. 2003; 2(2): 123–31.

[6] Shah K, Jacobs A, Breakefield XO, Weissleder R, 'Molecular imaging of gene therapy for cancer' *Gene Ther*. 2004; 11(15): 1175–1187.

[7] Yang Y, Tai YC, Siegel S, et al., 'Optimization and performance evaluation of the microPET II scanner for *in vivo* small-animal imaging' *Phys. Med. Biol.* 2004; 49(12): 2527–2545.

[8] Jaszczak RJ, Li J, Wang H, Zalutsky MR, Coleman RE, 'Pinhole collimation for ultra-high-resolution small-field-of-view SPECT' *Phys. Med. Biol.* 1994; 39: 425–37.

[9] Ishizu K, Mukai T, Yonekura Y, et al., 'Ultra-high-resolution SPECT system using four pinhole collimators for small animal studies' *J. Nucl. Med.* 1995; 26: 2282–2289.

[10] Weber DA, Ivanovic M, 'Ultra-high-resolution imaging of small animals: implications for preclinical and research studies' *J. Nucl. Card.* 1999; 6: 332–344.

[11] Wu MC, Tang HR, Gao DW, et al., 'ECG gated pinhole SPECT in mice with millimeter resolution' *IEEE Trans. Nucl. Sci.* 2000; 47: 1218–1227.

[12] Meikle SR, Fulton RR, Eberl S, Dahlbom M, Wong K. P, Fulham MJ, 'An investigation of coded aperture imaging for small animal SPECT' *IEEE Trans. Nucl. Sci.* 2001; 48: 816–821.

[13] McElroy DP, MacDonald LR, Beekman FJ, et al., 'Performance evaluation of A-SPECT: A high resolution desktop pinhole SPECT system for imaging small animals' *IEEE Trans. Nucl. Sci.* 2002; 49: 2139–2147.

[14] Beekman FJ, Vastenhouw B, 'Design and simulation of a high-resolution stationary SPECT system for small animals' *Phys. Med. Biol.* 2004; 49: 4579–4592.

[15] Chatziioannou A, 'Molecular imaging of small animals with dedicated PET tomographs' *Eur. J. Nucl. Med. Mol. Im.* 2002; 29: 98–114.

[16] Beekman FJ, McElroy DP, Berger F, Gambhir SS, Hoffman EJ, Cherry SR, 'Towards *in vivo* nuclear microscopy: I-125 imaging in mice using micro-pinholes' *Eur. J. Nucl. Med. Mol. Im*. 2002; 29(7): 933–938.

[17] Rowe RK, Aarsvold JN, Barrett HH, et al., 'A stationary hemispherical SPECT imager for three-dimensional brain imaging' *J. Nucl. Med.* 1993; 34: 474–480.

[18] Liu Z, Kastis GA, Stevenson GD, et al., 'Quantitative analysis of acute myocardial infarct in rat hearts with ischemia-reperfusion using a high-resolution stationary SPECT system' *J. Nucl. Med.* 2002; 43(7): 933–939.

[19] van der Have F, Beekman FJ, 'Photon penetration and scatter in micro-pinhole imaging: a Monte Carlo investigation' *Phys. Med. Biol.* 2004; 49: 1369–1386.

[20] Lange K, Carson R, 'E.M. reconstruction algorithms for emission and transmission tomography' *J. Comput. Assist. Tomo*. 1984; 8: 306–316.

[21] Metzler SD, Bowsher JE, Smith MF, Jaszczak RJ, 'Analytic determination of pinhole collimator sensitivity with penetration' *IEEE Trans. Med. Im.* 2001; 20: 730–741.

[22] Accorsi R, Metzler SD, 'Analytic determination of the resolution-equivalent effective diameter of a pinhole collimator' *IEEE Trans. Med. Im.* 2004; 23(6): 750–763.

[23] Beekman FJ, Vastenhouw B, van der Have F, 'Towards 3D nuclear microscopy using locally focusing many-pinhole SPECT' *Proceedings of the 2003 International Meeting on Fully Three-Dimensional Image Reconstruction in Radiology and Nuclear Medicine*, 2004.

[24] Orlov SS, 'Theory of three-dimensional reconstruction. I. conditions for a complete set of projections' *Soviet Phys. Crystallogr*. 1975; 20: 429–433.

[25] Matherson KJ, Barber HB, Barrett HH, et al., 'Progress in the development of larger-area modular 64x64 CdZnTe imaging arrays for nuclear medicine' *IEEE Trans. Nucl. Sci.* 1998; 45: 354–358.

[26] He Z, Li W, Knoll GF, Wehe DK, Stahle CM, '3-D position sensitive CdZnTe gamma-ray spectrometers' *Nucl. Instr. Meth. A*. 1999; 422: 173–178.

[27] Llopart X, Campbell M, Dinapoli R, Segundo DS, Pemigotti E, 'Medipix2: a 64-k pixel readout chip with 55-μm square elements working in single photon counting mode' *IEEE Trans. Nucl. Sci.* 2002; 49(5): 2279–2283.

[28] Pani R, Pellegrini R, Cinti MN, et al., 'New devices for imaging in nuclear medicine' *Cancer Biother. Radio*. 2004; 19(1): 121–128.

[29] de Vree GA, Westra AH, Moody I, van der Have F, Ligtvoet CM, Beekman FJ, 'Photon-counting gamma camera based on an electron-multiplying CCD' *IEEE Trans. Nucl. Sci.* 2005; 52(3):580-588.

[30] Meikle SR, Fulton RR, Eberl S, Dahlbom M, Wong KP, Fulham MJ, 'An investigation of coded aperture imaging for small animal SPECT' *IEEE Trans. Nucl. Sci*. 2001; 48 (3):816-821.

[31] Meikle SR, Kench P, Weisenberger AG, Wojcik R, Smith MF, Majewski S, Eberl S, Fulton RR, Rosenfeld AB, Fulham MJ, 'A prototype coded aperture detector for small animal SPECT' *IEEE Trans. Nucl. Sci*. 2002; 49(5): 2167-2171.

Chapter 3

System Calibration and Statistical Image Reconstruction for Ultra-high Resolution Stationary Pinhole SPECT

Frans van der Have, Brendan Vastenhouw, Mart Rentmeester and Freek J. Beekman

IEEE Transactions on Medical Imaging, 2008; 27: 960-971.

Abstract

For multi-pinhole SPECT, iterative reconstruction algorithms are preferred over analytical methods, because of the often complex multi-pinhole geometries and the ability of iterative algorithms to compensate for effects like spatially variant sensitivity and resolution. Ideally, such compensation methods are based on accurate knowledge of the position-dependent point spread functions (PSFs) specifying the response of the detectors to a point source at every position in the instrument.

This chapter describes a method for model-based generation of complete PSF lookup tables from a limited number of point-source measurements for stationary SPECT systems and its application to a sub-mm resolution stationary small-animal SPECT system containing 75 pinholes (U-SPECT-I). The method is based on the generalization over the entire object to be reconstructed, of a small number of properties of point-source responses which are obtained at a limited number of measurement positions. The full shape of measured point-source responses can almost be preserved in newly created PSF tables.

We show that these PSFs can be used to obtain high-resolution SPECT reconstructions: the reconstructed resolutions judged by rod visibility in a micro Derenzo phantom are 0.45 mm with 0.6 mm pinholes and below 0.35 mm with 0.3 mm pinholes. In addition, we show that different approximations, such as truncating the PSF kernel, with significant reduction of reconstruction time, can still lead to acceptable reconstructions.

Introduction

Single Photon Emission Computed Tomography (SPECT) permits *in vivo* volumetric imaging of 3D distributions of radio-labeled molecules. Pinhole-collimated SPECT is particularly suitable for studying laboratory animals such as mice and rats, because for small objects it can achieve both a high spatial system resolution and a high sensitivity when compared to parallel-hole collimated SPECT. Several SPECT systems using pinhole collimation have been developed [1–7] (for reviews see [8–11] and for design considerations see [12]). Stationary systems (that do not need to rotate their detectors) with tens up to hundreds of pinholes have been designed [13–17]. A high number of pinholes results in a high sensitivity which can be traded for a higher system resolution by decreasing the pinhole diameter. The stationary designs provide excellent stability and unique capabilities to perform fast dynamic studies, e.g. [13, 18, 19].

Today, iterative reconstruction algorithms are prominent in SPECT. Iterative algorithms have the advantage that they can benefit from accurate models of the photon transport in the SPECT system and they can handle a large variety of detector-collimator geometries. In addition, they can deal with noise better than direct methods of reconstruction. Several papers have shown that the more accurate photon transport is modeled during iterative reconstruction the more accurate the reconstructed images

will be, not only in terms of resolution and quantitative accuracy but also in terms of signal-to-noise ratio and lesion detectability, e.g. [20–24]. An important advantage of iterative reconstruction is that no explicit mathematical expression for the inverse transformation is required. Iterative algorithms only need a way to predict the detector response to a given radio nuclide distribution in the object. To this end, the object space is most times divided into volume elements (voxels) and the total detector response is assumed to be the sum of the responses to small radioactive sources in all of the voxels. A specific detector response to a point source is known as the point spread function (PSF). The individual PSFs for all voxels collectively contain the entire information to set up the "system matrix" or "transition matrix" $\boldsymbol{M}$ of the SPECT system. Each matrix element $\boldsymbol{M_{ji}}$ represents the likelihood that a photon emitted in voxel i is detected in detector pixel j. Then, the activity distribution $\boldsymbol{a}$ is estimated from $\boldsymbol{p = M \cdot a + n}$ where $\boldsymbol{p}$ is the measured projection and $\boldsymbol{n}$ represents the noise in each pixel.

The PSFs for SPECT are sometimes calculated analytically [4, 25–27], given "known" properties of the system. Pinhole collimators make the detector response very sensitive to some parameters, e.g. the exact position, orientation, size, and shape of each pinhole aperture in the system. Methods for the calibration of rotating pinhole SPECT systems (based on calibration systems for cone-beam SPECT with similar geometry) have been proposed, e.g. [26, 28–33], that can determine the acquisition geometry (e.g. the position of the pinhole with respect to the axis of rotation and the position, tilt and twist of the detector) using one up to three point sources. These systems still use an analytical model to estimate the pixel values in a PSF. In stationary pinhole systems, it is feasible to determine the PSFs themselves experimentally with a large number of point-source measurements. This has the advantage that the actual positions, orientations, and sizes of the pinholes and detector pixel sensitivities are accurately incorporated into the PSF tables. Difficulties in manufacturing precise pinhole positions and shapes with exactly the specified diameter (which is only a few tenths of a mm for high-resolution SPECT in mice) could make analytically predicted PSFs deviate from reality. The approach of measuring the complete matrix with a point source was developed at the University of Arizona and was used to calibrate different SPECT systems [14, 15, 34, 35].

Recently, resolutions of small-animal SPECT systems have improved from typically a few mm to sub-half-mm resolution [11, 16, 17, 36, 37], which makes it hard to measure the PSF for each voxel: up to millions of tiny voxels are needed to represent the high-resolution images. Then, it is impractical to put a point source that is approximately the size of one voxel at every voxel position. The maximum achievable concentration of radioactivity and the number of counts that have to be acquired from every point position, make it a prohibitively long measurement. In addition, the point source may need to be replaced many times predictably at a precisely known position. Apart from a high number of voxels, a high-resolution scanner may also need a relatively high number of pixels. This combination could mean that the intermediate storage of all raw data requires enormous amounts of disk

space on systems where the acquisition hardware or software does not permit the acquired data to be directly stored in other formats than raw pixelized images.

Here we propose and validate an efficient and accurate method to obtain the position-sensitive PSF tables for a high-resolution many-pinhole system [16, 17]. We explain how the full system matrix can be determined from measurements at a limited number of positions. In addition, we will present examples to give an impression of the accuracy of estimated PSFs as well as reconstructed images. The trade-off between truncation of the PSF kernel and the reconstruction speed was also investigated. Reconstructed images are presented for a capillary resolution phantom with different numbers of acquired counts.

Methods

The method described in this chapter is developed for the stationary pinhole SPECT systems U-SPECT-I and U-SPECT-II [16, 36, 38]. These systems have 75 focusing pinholes in a cylindrical configuration with 5 rings of 15 pinholes each (see figure 1). The collimator cylinder is placed in the center of three gamma camera heads. Each of the camera heads is divided into a large set of mini gamma cameras, each dedicated to the projection through one pinhole. We ensure that the projection areas are non-overlapping by means of a shielding tube [16,39,40]. Figure 2 shows how this results in dividing the three large detectors in many small cameras. It also shows an image obtained by placing a bottle with Tc-99m pertechnetate in the scanner as well as an image from a point source.

The method described here for obtaining the PSF tables is based on calculating a number of defining properties at the detector segments (namely the position on the detector, the flux, and the spatial extent) for each measured point-source response. The available data are then used to fit a parametric model of these properties and the fit results are used to predict the PSFs for all voxels.

Full PSF tables (representing the system matrix) are obtained out of a set of point-source responses in four steps:

1. Noise suppression and identification of areas that contain the local maximum of a point-source response.
2. Characterizing the PSFs using Gaussian modeling.
3. Generalization of the PSFs model over the object space using an analytical pinhole model.
4. Calculation of the supplementary PSFs for storage in tables.

These steps are explained in more detail in the subsections below.

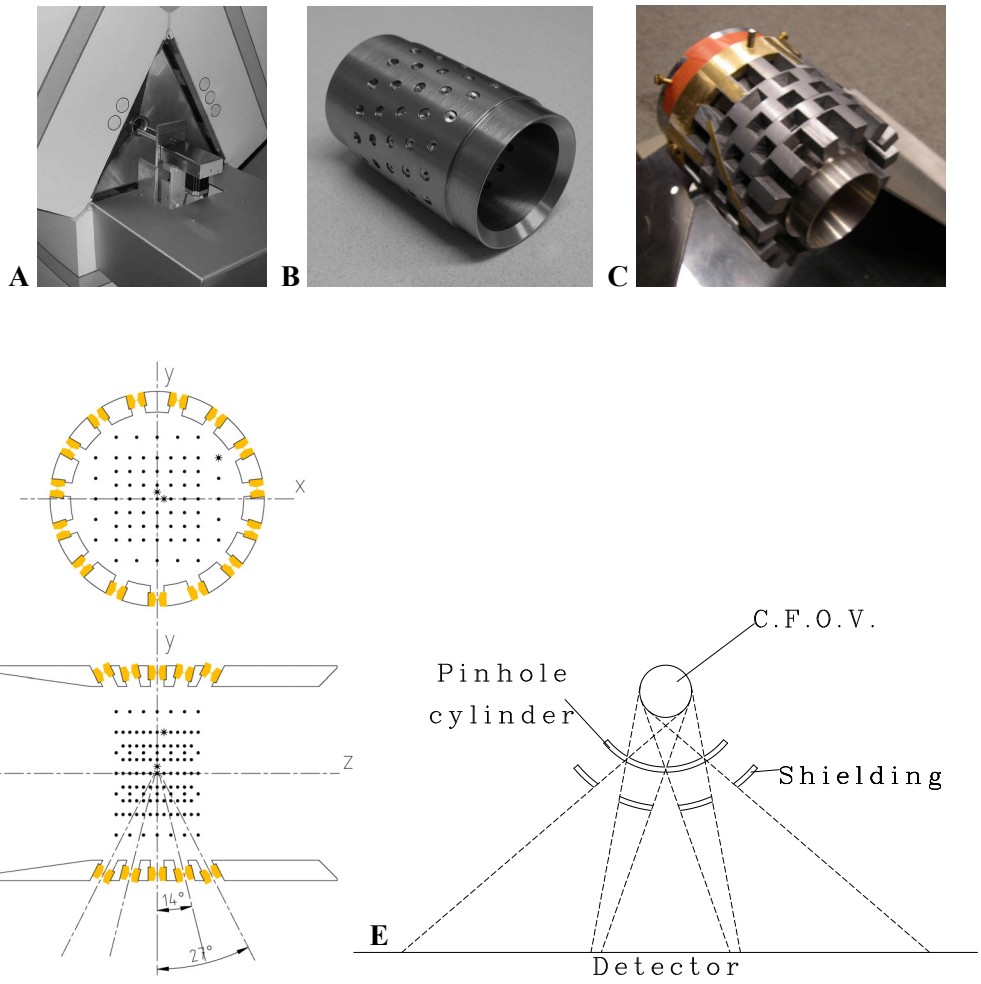

Figure 1: (A) The U-SPECT-I system. Triangular-shaped lead shielding is placed in between three camera heads. A tungsten cylinder containing pinholes is placed in the center of the three detectors. An XYZ-stage with attached bed is placed in front of the lower detector. (B) Cylinder with 75 gold pinhole apertures. (C) The cylinder with pinholes surrounded by the shielding that prevents projections to overlap. (D) Cross-section of the cylinder with focusing pinholes. x, y and z define the coordinate system used in the object space. Solid circles indicate the positions of the point source used for calibration. Stars indicate the example point source positions for validation. (E) Schematic cross-section of the shielding tube that prevents projections from overlapping.

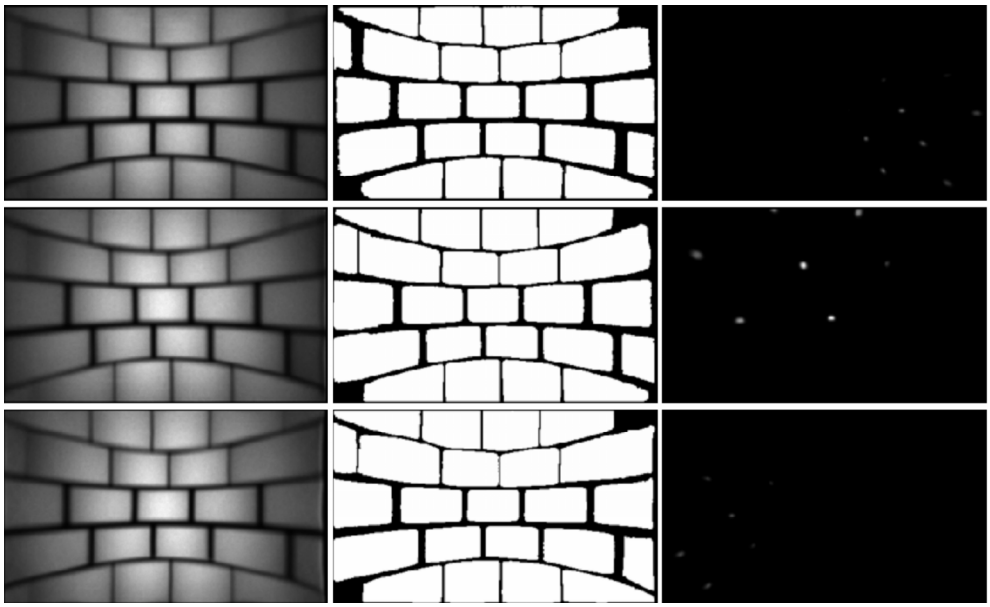

Figure 2: (A) Measurement with extended source. (B) Segmentation of the three detectors into mini gamma cameras. (C) Projection of a single point source on the mini cameras.

Noise suppression and identification of areas that contain the local maximum of a point-source response

High-frequency noise in the point-source projections is suppressed by a fit procedure that is based on fitting Gaussian basis functions with a certain width to the data using a Maximum Likelihood Expectation Maximization (ML-EM) algorithm. This is equivalent to Richardson-Lucy deconvolution [41,42] followed by one convolution with the same Gaussian kernel. More details about the procedure can be found in [43]. In contrast to low-pass filtering, this procedure does not degrade the resolution of the measurements, since the width of the convolution kernel (3.0 mm FWHM) is chosen slightly smaller than the detectors' intrinsic resolution (3.2 mm FWHM). The result of the procedure is demonstrated in figure 3.

Each detector segment should contain either one or no projected point source. The "worst case" situation resulting in the lowest number of counts per pixel is considered. That is when the point source is located at the measurement position that is the farthest away from the pinhole and at the maximum angle from the pinhole's axis. Based on the maximum pixel value in that situation, a threshold level is chosen. Only those detector segments where at least one pixel is above this local threshold are assumed to contain a PSF.

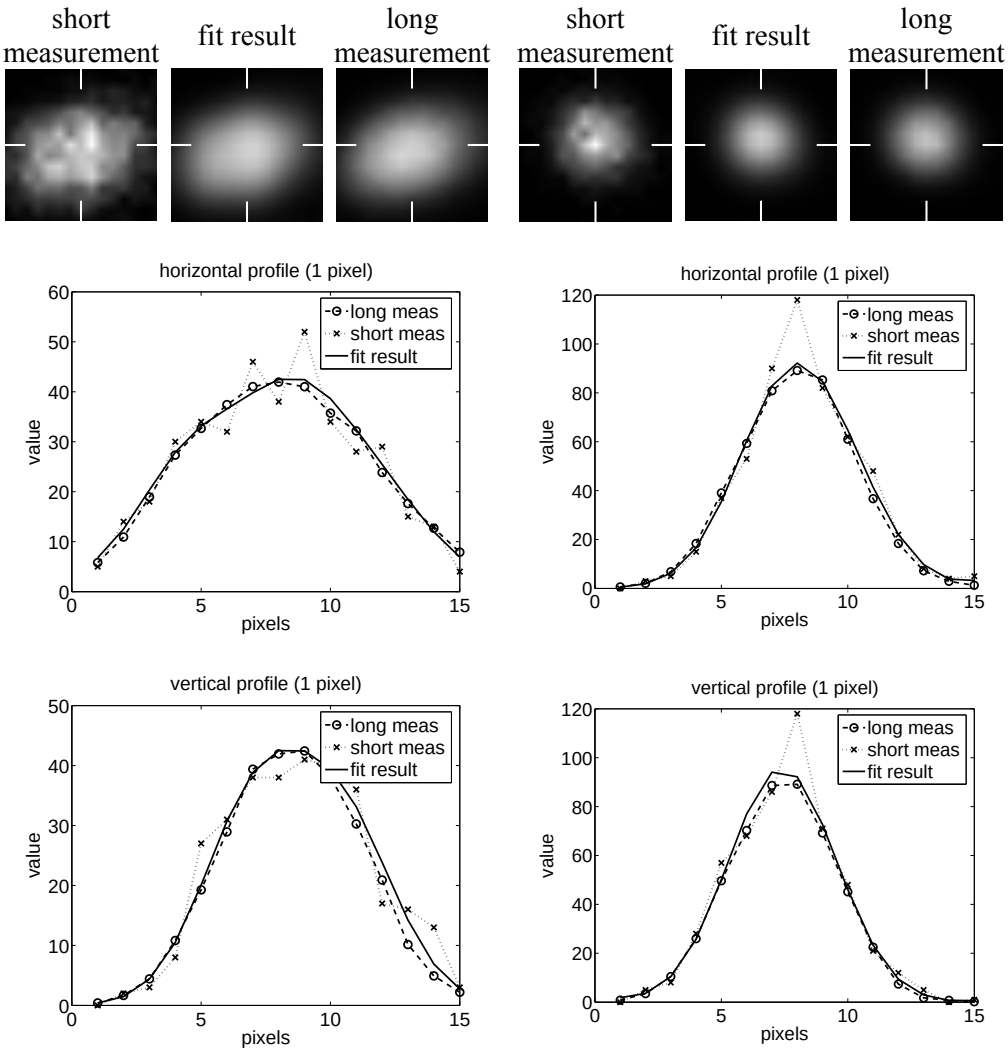

Figure 3: Effect of the noise-suppression procedure for two point-source projections. The image after fitting is close to a reference image that has a 40 times longer acquisition period. Horizontal and vertical profiles show the values of a single row and column of pixels through the maximum, indicated by white markers.

Characterizing the PSFs using Gaussian modeling

As the next step, each measured point-source response is divided pixel-by-pixel by a high-count projection image of a cylindrical reservoir (bottle) that was filled homogeneously with Tc-99m. To avoid undesirable truncation effects the bottle is a few times larger than the central field-of-view of the system. The high-count bottle

projection contains information about the partial shielding of pixels at segment edges as defined by the baffles that prevent overlapping of projections.

Division by the bottle projection converts the relative intensities of neighboring edge pixels to approximately what they would have been if there were no baffles. It does not take into account scattered photons and photons that penetrate the shielding, but the relative contribution of those photons is low [44]. Figure 4 illustrates the effect of the division. The procedure enables pixels near the segment edges to be used for reconstruction, but introduces a low-frequency change in the PSF. The division of the angular response of the pinhole by the projection of a cylindrical activity distribution may reduce the curvature of the low-frequency response, as illustrated by figure 4, which shows a profile with the shape of a strongly bent arc being transformed into a profile with less pronounced curvature. Later in the calibration procedure, the pixel values will be multiplied again by the same extended homogeneous source projection. This restores the original scaling and recovers the appropriate pixel values in the PSFs. Therefore the low-frequency change induced by the division does not end up in the final PSF tables.

After noise suppression and after division by the high-count uniform source projection, for each segment the position of the maximum on the detector (ξ, η), the amplitude A, and the width σ are estimated for each point-source measurement using the Powell fitting algorithm [45]. This is an unweighted least-squares fit of a two-dimensional circular Gaussian:

$$A \cdot \exp\left(-\frac{(i-\xi)^2 + (j-\eta)^2}{2\sigma^2} \right)$$

where i and j are the varying pixel indices.

The detector position of the maximum (ξ, η) is determined to sub-pixel level. The flux (total number of counts) Φ is estimated by $\Phi = 2\pi \cdot A \cdot \sigma^2$. This is an approximation, but it has the advantage that it also works when part of the PSF is outside the detector segment and therefore missing from the measurement.

The property values can only be determined reliably if a large enough fraction of the PSF is located within the detector segment. In order to guarantee this, the properties of a PSF are only determined and used for generalizing the PSF if the pixel with the highest value (after noise suppression) is not on or outside a segment edge, but surrounded by pixels that are inside the segment on all sides.

The PSFs are very localized on the detector. Including all pixels in a detector segment in the fit procedure may reduce the accuracy of the fit result because the "empty" parts of the detector still contain noise. Therefore, only the area surrounding the maximum is taken into account. The number of pixels included needs to be larger for wide PSFs than for narrow ones. Therefore, the fit is done twice. In the first instance all pixels that are both within the segment and within a fixed 15 × 15 square of pixels (13 × 13 mm) around the maximum are used. The result of the first fit is used to obtain an approximate value for σ which is subsequently used to determine

which pixels are taken into account for the second fit: a square area of $2\sigma \times 2\sigma$, rounded off to an odd-valued integer, and centered around the maximum.

For each detector segment, four 3D arrays are created where the values of the PSF properties are stored as a function of the *x, y, z* coordinates of the measurement grid in the SPECT system. These arrays are from here on referred to as "property volumes".

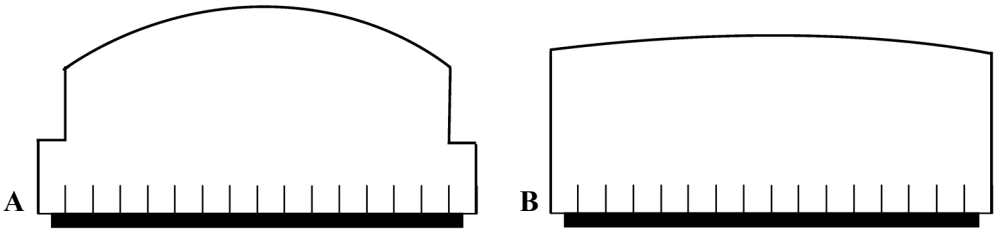

Figure 4: Effect of the projection division by a homogeneous source image: (A) profile of the projection of an extended object before division. The part of the detector that is not blocked by the shielding is represented by the black rectangle. The short vertical lines indicate the pixel boundaries. The outermost pixels are covered by the shielding for part of their surface, in this example half of it. (B) Profile of the same object projection, but after the division.

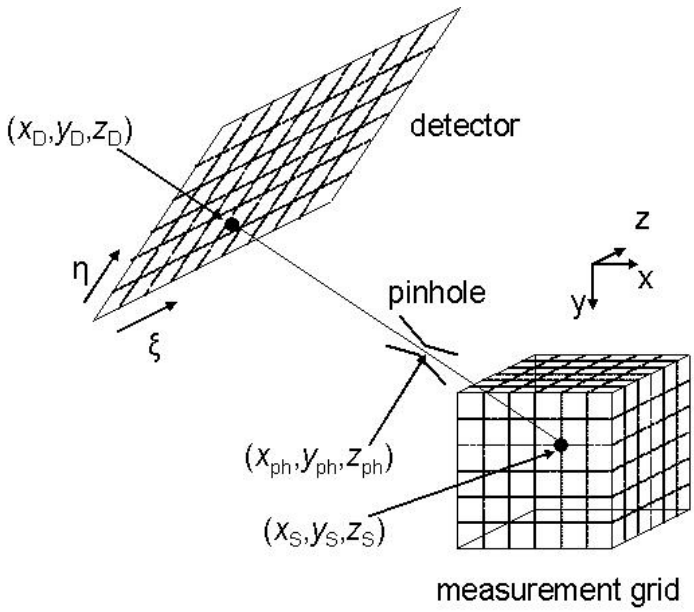

Figure 5: The geometry of the model for the ξ and η position on the detector. A certain source location (x_S, y_S, z_S) is projected through the pinhole center onto a detector plane, the location of detection is at x_D, y_D, z_D.

Generalization of the PSF's model over the object space using an analytical pinhole model

One would like to limit the number of measurement points to a few hundred. On the other hand, PSFs must be available for all points that can be observed by one or more pinholes. When the voxel size is 0.125 mm, this means that less than one out of every 6000 voxels is a measurement position. The addition of a limited amount of geometrical information (see also the discussion) is required.

Position of the PSF maximum on the detector

The geometry of the detector position model is illustrated in figure 5. The point-source activity is projected through the pinhole onto a detector segment of which the orientation is not precisely known. The effective position of detection is determined by the fit procedure which has three variables (the point source's position x_S, y_S, z_S) and nine parameters: the pinhole's position (x_{PH}, y_{PH}, z_{PH}), the position (x_T, y_T, z_T) of the origin of the detector's coordinate system expressed in the coordinate system of the measurement grid, and three rotation or Euler angles (φ, θ, ψ) for the detector orientation.

In order to build a mathematical model suitable for fitting, the available measured quantities need to be linked to the model's parameters and variables. The position of the point of detection (x_D, y_D, z_D) in the measurement grid's coordinate system can be related to the pinhole position (x_{PH}, y_{PH}, z_{PH}) and the source position (x_S, y_S, z_S) by assuming that the detection point, the center of the pinhole and the source are situated on the same line:

$$\frac{x_s - x_{PH}}{x_{PH} - x_D} = \frac{y_s - y_{PH}}{y_{PH} - y_D} = \frac{z_s - z_{PH}}{z_{PH} - z_D} \qquad \textbf{(1)}$$

The coordinates (x_D, y_D, z_D) in the measurement grid's coordinate system of the point of detection are also related to the coordinates of this point in the detector's coordinate system (ξ, η) via translation and rotation:

$$R \cdot \begin{pmatrix} \xi \\ \eta \\ 0 \end{pmatrix} + \begin{pmatrix} x_T \\ y_T \\ z_T \end{pmatrix} = \begin{pmatrix} x_D \\ y_D \\ z_D \end{pmatrix} \qquad \textbf{(2)}$$

where R is a standard rotation matrix expressed in terms of the Euler angles φ, θ, and ψ. Note that equating the third coordinate of the detection point in the detector's coordinate system to zero effectively means that all detections are in a plane; i.e. the model approximates the detection volume in the scintillation crystal, which has a finite thickness and is expected to be slightly curved due to depth-of-interaction effects, by a single plane.

By combining equations **(1)** and **(2)** and eliminating x_D, y_D, and z_D it is possible to express the available data (ξ and η of each point-source projecting through the pinhole of this mini-camera) in terms of the model's variables and parameters. This is the desired form of a mathematical model in order to be suitable for parameter estimation by fitting. Fitting was performed using the Levenberg-Marquardt algorithm. The initial guess can be obtained by assuming that the pinhole location is on the surface of a cylinder, as seen from the center in the direction of the measurement grid position where the measured intensity is highest. For the initial guess of the detector's position and orientation, the detector can be assumed to be behind the pinhole, perpendicular to the pinhole axis at the average of the minimum and maximum pinhole-to-detector distances that occur in the U-SPECT-I system.

The flux model

Like the position of the center of the PSF, the flux is also generalized using a parametric model and the same nonlinear fit routine. The geometry explaining the flux model is illustrated in figure 6. A coordinate system is defined with one axis (denoted "r") approximately along the pinhole axis. To find it without specifying the pinhole axis explicitly, we use the fact that the axis must go through the center of the pinhole as found in the position fit. The axis is assumed to go through the center of gravity of the cloud of measurement points as well. The other two axes (denoted "u" and "v") are orthogonal to the pinhole axis and to each other. The flux Φ in a certain voxel is modeled:

$$\Phi = \frac{1}{r^2}\left(A + B\cdot\theta_u + C\cdot\theta_v + D\cdot\theta_u^2 + E\cdot\theta_v^2 + F\cdot\theta_u\cdot\theta_v\right) \qquad \textbf{(3)}$$

where r is the component along the pinhole axis of the distance between the voxel and the pinhole position, obtained from the position fit carried out previously, and θ_u and θ_v are the distances from the voxel to the pinhole in the u and v directions, expressed as angles.

Perpendicular to the pinhole axis, the flux is modeled by the general paraboloid of equation **(3)**. If θ is the angle between the pinhole axis and the line connecting the voxel and the pinhole center, then one might expect a $\cos^3(\theta)$ dependency. However, the projection data have been divided by the projection of an extended homogeneous source before the flux was measured so the flux data are not exactly described by the $\cos^3(\theta)$ fall-off away from the pinhole axis. The fall-off is in fact still very smooth, however, and can be approximated by a paraboloid.

Using fitted parameter values A – F the flux value can be calculated for each voxel in the object space.

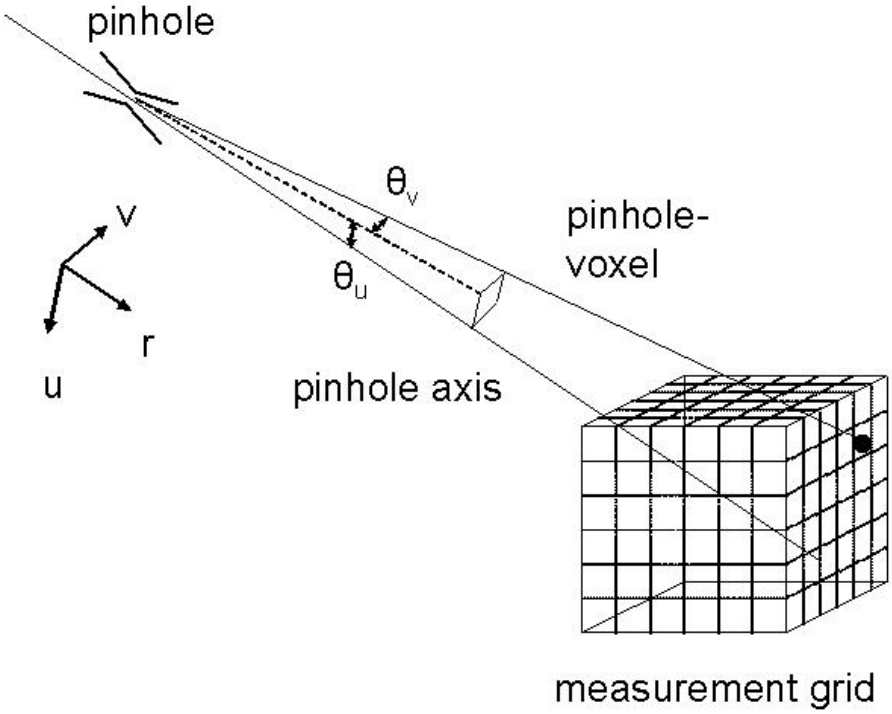

Figure 6: The geometry for modeling the flux.

The width

The width σ of each PSF is described as:

$$\sigma = \sqrt{\left(D_{\text{eff,R}} \cdot \frac{l+r}{r}\right)^2 + R^2}$$

where $D_{\text{eff,R}}$ describes the effective pinhole diameter with respect to resolution, l is the distance from the pinhole to the detector, projected along the pinhole axis, and r is the distance from the point source to the pinhole, projected along the pinhole axis. The first term under the square root describes the effective pinhole diameter, projected magnified onto the detector as seen from the source. The second term R describes the camera's intrinsic resolution. Again, the pinhole position is taken from the position fit and the axis is assumed to go through the center of gravity of the cloud of measurement points. $D_{\text{eff,R}}$, R, and l are used as parameters in a fit using the Levenberg-Marquardt algorithm. Once their value has been determined for the current mini-camera (using r and σ as data), the width σ can be calculated for each voxel in the object space.

Calculation of the supplementary PSFs for storage in tables

Since a low-noise (by means of the noise suppression described earlier) version of measured PSFs is available, we choose to use those measured PSFs to get the correct overall shape. To estimate a "missing" PSF (for a voxel location not in the measurement grid), the measured PSF whose corresponding point source location is nearest to the missing voxel location is used. That PSF is displaced on the detector to the location specified by the ξ and η values in the property volumes at the missing voxel location. The PSF is then stretched or contracted using the ratio of σ at the missing point source position to σ of the measured PSF in both directions. The number of pixels incorporated in the newly created PSF can be varied. We define the "tail size" to be the diameter of the PSF on the detector, where nonzero pixel values are created. It is expressed as the number of times that the Full Width Half Maximum (FWHM) of the PSF fits in this diameter. Finally, all pixel intensities in the newly created PSF are scaled such that their sum equals the flux specified by the flux volume at the missing point source location. After the PSF has been created in this way, the pixel intensities should be multiplied by the extended homogeneous source measurement to undo the effect of the division by this measurement at the stage where the properties were determined. According to this procedure, a PSF is calculated for all missing point source positions. These are stored on disk to be used in the image reconstruction algorithm.

Validation

We have validated the proposed generalization of PSFs by measuring some additional PSFs to the ones used to generate the PSF tables. These are compared to the corresponding PSFs in the PSF tables. The system is calibrated using 679 measurement positions, indicated by solid circles in figure 1. The spacing in the central part is 3 mm in the x and y (transaxial) directions and 1.5 mm in the z (axial) direction. The outer positions are at x or y = 13.5 mm, spaced 4.5 mm in the x, y plane and 3 mm in the z-direction.

Another validation approach is to verify that the calibration method as a whole produces high resolution reconstructed images, which will also be described in the next section, using a capillary mini-Derenzo phantom as shown in figure 7 as the object.

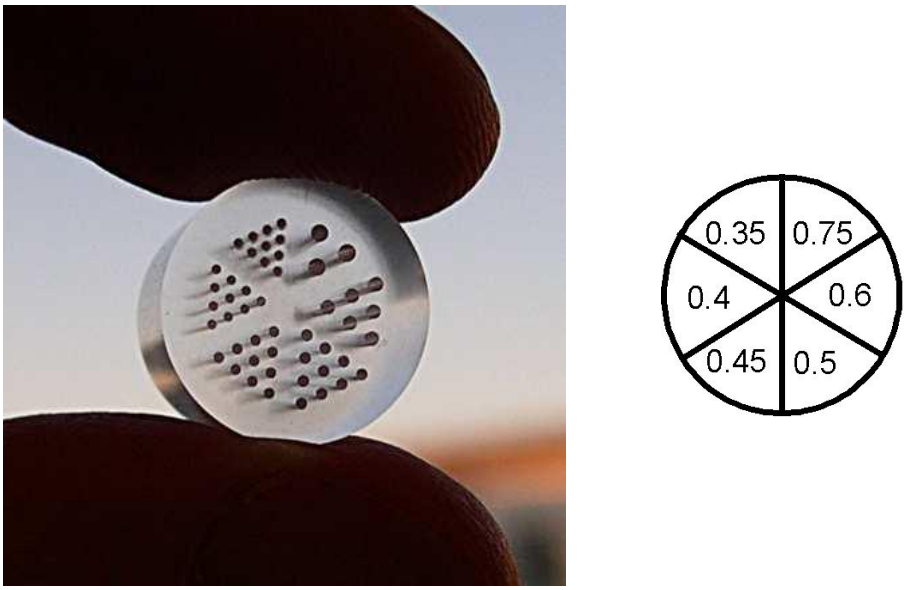

Figure 7: Photograph and drawing of the capillary hot-rod phantom used in the experiments. The minimum distance between capillaries is equal to the diameter. Capillary sizes of this phantom range from 0.35 to 0.75 mm.

Results

Validation in the projection domain

Figure 8 presents some examples of PSFs from the PSF tables generated by the procedure, alongside experimentally measured PSFs at the corresponding voxel location. Horizontal and vertical profiles through the center are shown that are summed over 3 pixels. The point source was at x, y, z = (0, 1.5, 0) mm in the first example, at (1.5, 0, 0) mm for the second and third example, and at (13.5, 9, 1.5) mm for the fourth example. The latter projects to a segment near to the edge of the detector. The first three examples show that in the central field-of-view (the volume seen by all pinholes), there is a good agreement between the measured PSFs and the PSFs from the PSF tables. Therefore, the position, flux and width are all correctly predicted by the model. The fourth example shows a small position mismatch in the vertical direction, on the order of 0.5 mm on the detector. This remains well below the detector's intrinsic resolution and would lead to a positioning error in the object space of less than 0.1 mm. This example also shows an underestimation of the flux. This still leads to good reconstructions, as will be shown further on in this chapter for small objects. Applications to objects larger than the central field-of-view are shown in [36].

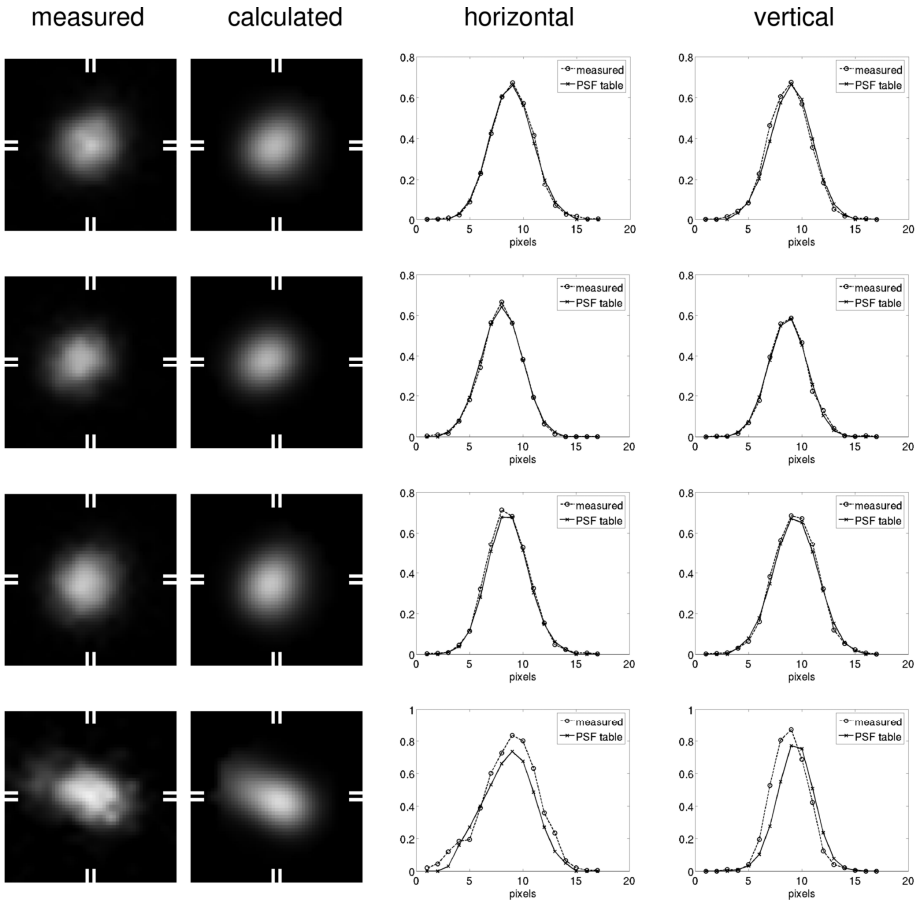

Figure 8: Four examples of a measured PSF, obtained at a location non on the grid that was used to create the PSF tables, with the corresponding PSFs from the PSF tables. The first three examples are from the central area, where the PSFs from the PSF tables predict the position and shape very well. The last example was obtained at a location more towards one side of the cylinder. Because it was also close to the edge of a camera head, at non-perpendicular incidence, its shape is more elongated.

Reconstruction quality versus PSF extent

There is an important trade-off in reconstruction methods, including the iterative statistical method we use, between reconstruction accuracy and matrix size. To investigate one aspect of this trade-off, the 'tail size' that was used when PSFs were created, was varied. The diameter of the detector area for which the PSF was created, was proportional to the generalized σ of the PSF. The PSF generation is implemented in such a way that there is always at least one pixel in each PSF. For example, in the limiting case where the PSF diameter is 0× the FWHM (δ-response),

all PSFs are created as the single pixel that is closest to the specified ξ, η location, containing the total specified flux. Figures 9–11 give reconstructed results for 50,100, and 150 iterations, while the tail size incorporated in the PSF is 0× FWHM, 0.43× FWHM, 0.68× FWHM, and 1.1× FWHM. Figure 9 is for the 0.3 mm pinholes and 0.1875 mm voxel size, figure 10 is for 0.6 mm pinholes and 0.1875 mm voxel size, and figure 11 is for 0.6 mm pinholes and 0.375 mm voxel size. The results are all compared at a slice thickness of 0.375 mm. The resulting matrix sizes on disk are given for reference as well as example reconstruction times on a 2.66 GHz Xeon system. This system had 8 Gb of memory, such that in all cases the matrix needed to be read from disk only once. The matrices used were available for a much larger voxel extent than the capillary phantom shown, which means that they would also be suitable for total-body mouse imaging [36] for example. The reconstruction times were all obtained with the same fairly straightforward implementation of the Maximum Likelihood Expectation Maximization (ML-EM) algorithm which was not optimized for speed. The results show that the largest PSF width of 1.1× FWHM resulted in the reconstruction that allows the best visual distinction of rods. Wider PSFs were also tested, but did not lead to better results.

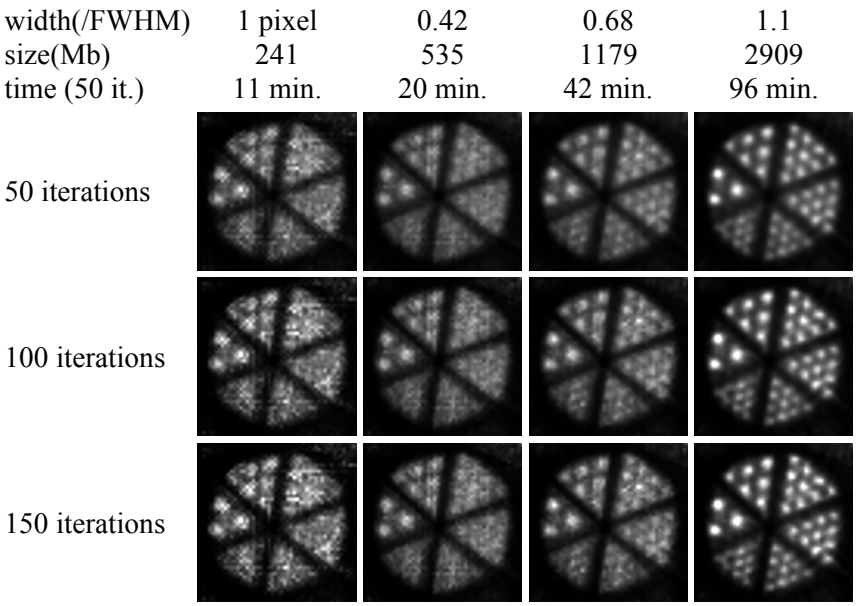

Figure 9: Reconstruction for different PSF tail sizes obtained with 0.3 mm pinholes. Voxel size 0.1875 mm. Slice thickness 0.375 mm. Numbers at the top represent the full width of the truncated PSF expressed in units of its FWHM, the resulting matrix size on disk in megabytes, and an example reconstruction time for 50 iterations. Vertically the number of iterations is varied: 50, 100, 150. Phantom capillary sizes are 0.75, 0.6, 0.5, 0.45, 0.4, and 0.35 mm.

Voxel size has a big impact on matrix size and thus reconstruction time, because of the cubic power relation between voxel size and matrix size. The effect of doubling the voxel size (leading to an eight-fold reduction in matrix size) on image quality for the case of 0.6 mm pinholes can be seen by comparing figures 10 and 11. While the smaller voxel size results look better, the difference is not so dramatic that the coarser voxels are useless; in some applications the images with the coarser voxels may be considered good enough — estimating the total amount of activity in a fairly large region-of-interest over multiple points in time for example — where the gain in speed could make it worthwhile to use coarse voxels.

With 0.3 mm pinholes smaller rods can be distinguished than with the 0.6 mm pinholes, which may not be surprising. What may not be obvious a priori is that the 0.6 mm pinholes actually require at least the same PSF size in units of FWHM as the 0.3 mm pinholes in order to reach the highest achievable resolution, while each FWHM is already larger than the corresponding PSF from a 0.3 mm pinhole because of the larger diameter. This makes the 0.3 mm pinholes matrix smaller than the 0.6 mm pinholes matrix, when comparing at equal voxel and pixel size, by a factor of approximately 2 in the given examples.

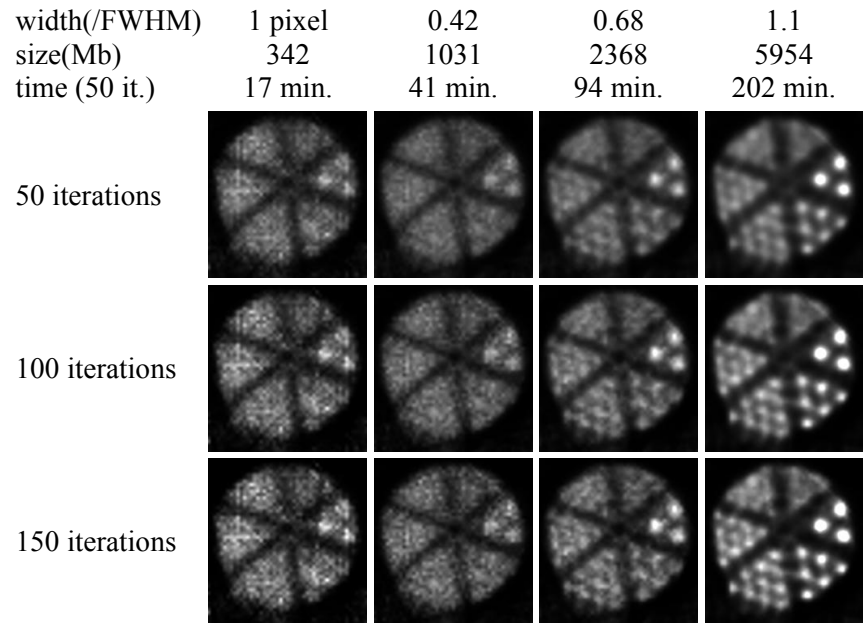

Figure 10: Like figure 9, but for 0.6 mm pinholes. Voxel size is 0.1875 mm.

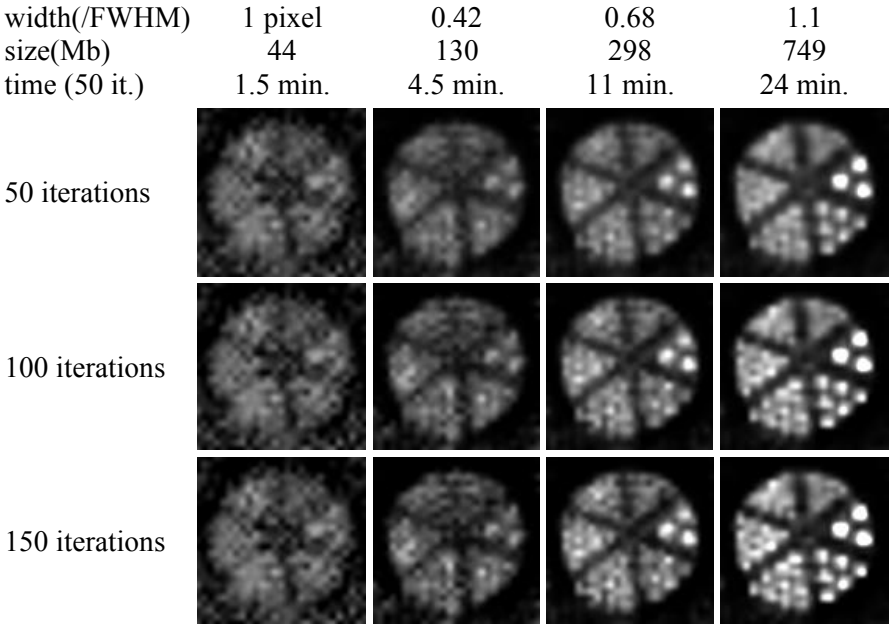

Figure 11: Like figure 10, but for 0.375 mm voxel size. Slice thickness is also 0.375 mm.

Reconstruction with different acquisition times for two pinhole diameters

Figure 12 shows the hot-rod resolution phantom images compared for different acquisition times. The activity concentration was 300 MBq/ml Tc-99m (25 MBq in total in the capillaries). The acquisition times can of course be scaled if one wants to have an impression of the achievable resolution at other concentrations. The experiment was done with both the 0.3 and the 0.6 mm pinholes and after reconstruction, the results are displayed for a slice thickness of 0.375 mm and 3.75 mm for each pinhole diameter. Visually the 0.3 mm pinholes yield a superior resolution for acquisition times down to 1 minute (or even shorter if the larger slice thickness is viewed). Only for extremely short acquisition times (below 1 minute) do the 0.6 mm pinholes produce superior results, because the 0.3 mm pinholes collect too few counts. For 10 seconds acquisition time, it is still possible to obtain 0.75 mm reconstructed resolution for the 0.6 mm pinholes. The best achievable resolution, on the other hand, is seen to be 0.45 mm for the 0.6 mm pinholes and below 0.35 mm for the 0.3 mm pinholes.

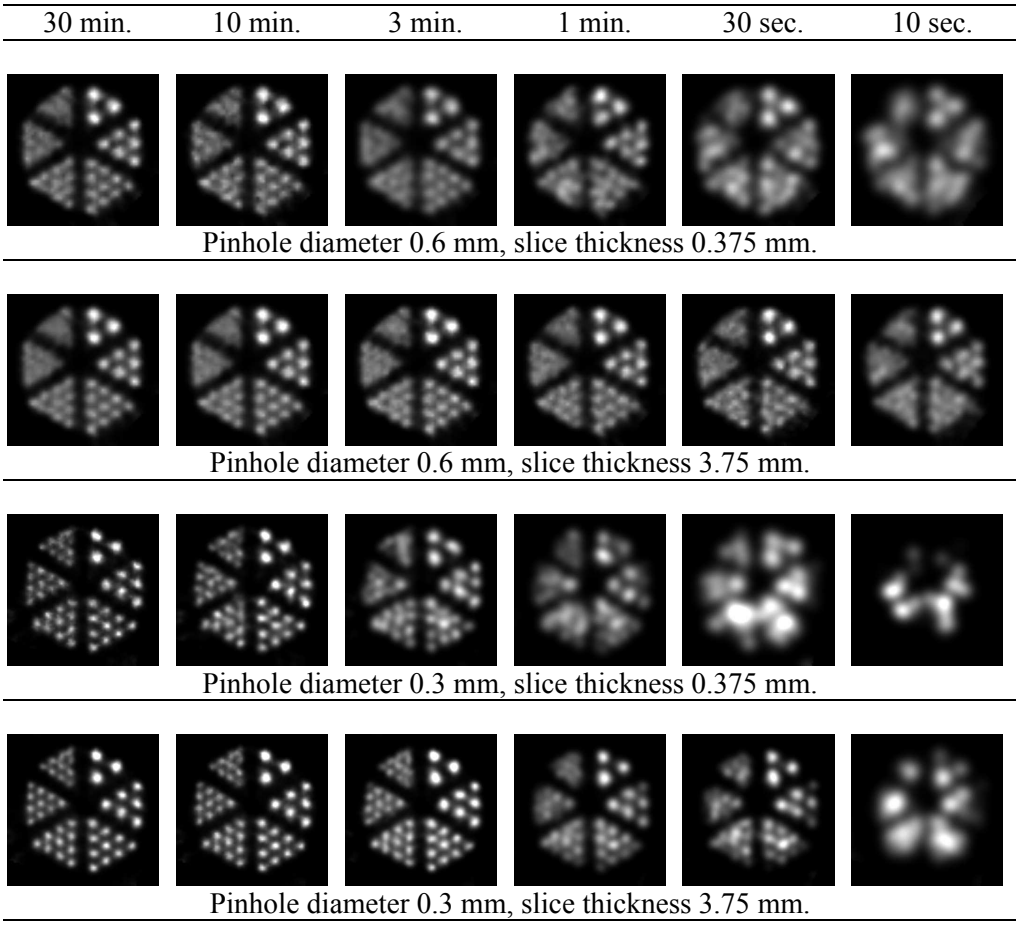

Figure 12: The influence of acquisition time (total number of detected counts) on the reconstructed image. This panel shows that with 0.3 mm pinholes a resolution of < 0.35 mm (0.04 µl) can be obtained. At extremely short acquisition times a resolution of 0.75 mm can still be reached. Acquisition times range from half an hour down to 10 seconds.

Discussion

In this chapter we have presented a method to obtain full PSF tables (i.e. calibrate a multi-pinhole system) based on a limited number of measurements and generalization of PSF properties over the object space. When using a scanning-focus method [36] to image a volume that is larger than the central field-of-view of the scanner, the PSFs need to be available throughout the collimator cylinder, including the outer area close behind the pinholes. Some geometrical information about the

system needs to be added for a generalization algorithm to be able to correctly find especially the position on the detector of each PSF. Therefore, we have added some geometrical information in our model, but not as much as specifying the exact location, orientation and shape of every pinhole. The uncertainty in those is one of the reasons to use experimentally determined PSFs in the first place. Trying to find a balance between adding too little and too much geometrical information we have arrived at the parametric fit procedure described earlier.

The required accuracy of the whole process also puts some demands on the mechanical accuracy of the robotic XYZ-stage that is used to step the point source through the collimator. The most important requirement of its accuracy and alignment is that the relative positions of the grid of points used to calibrate the system are accurate to sub-voxel level. The absolute position of the grid as a whole and its alignment with respect to the collimator are important to a lesser degree.

The system matrix is determined experimentally (as opposed to, e.g., analytically calculated) because this automatically takes into account most physical effects that influence detection. Wide-angle scatter is not incorporated in the PSF tables. However, the effects of object attenuation and scatter are much less severe in small-animal imaging as in human imaging. Pinhole aperture scattering typically amounts to a few percent of the total detected counts when Tc-99m is used [44].

The example reconstruction times that were indicated, were obtained with a straightforward implementation of the ML-EM algorithm. By using block-iterative algorithms (e.g. Ordered-Subsets EM) together with faster processors with parallel processing, the reconstruction can be accelerated by more than two orders of magnitude. Since it is not always given that OS-EM methods will converge in the same way as ML-EM, and the way to optimally implement them for a system such as U-SPECT is a topic of investigation in itself, we chose to use a “clean” ML-EM algorithm for the comparisons and results in this chapter.

Conclusion

This chapter presents a method to create full PSF tables for a small-animal SPECT scanner from a limited number of measurements with a point source. It is based on determining four properties of a PSF and generalizing those properties to include all locations where no point-source measurement is available. In this way the measurement of the PSF for all individual voxels is unnecessary. The full shape of measured PSFs can be used in generating full PSF tables (the system matrix). It is shown that the method correctly estimates the PSF at a “missing” location in a number of examples and leads to PSF tables that give sub-half-mm reconstruction results.

Using 0.6 mm pinholes, it is possible to combine sub-minute acquisition times with sub-mm resolution. PSF tables that model the actual system more accurately, e.g. by incorporating more of the tails, lead to better images at the cost of system matrix size.

Acknowledgements

This work was supported by the Netherlands Organization for Scientific Research (NWO), grant 917.36.335. The authors want to thank Dr. Lars R. Furenlid (University of Arizona) for his advice on producing the point sources used for calibration.

References

[1] Ishizu K, Mukai T, Yonekura Y, Pagani M, Fujita T, Tamaki N, Shibasaki H, Konishi J, 'Ultra-high-resolution SPECT system using four pinhole collimators for small animal studies', *J. Nucl. Med.* 1995; 26: 2282–2289.

[2] Meikle SR, Fulton RR, Eberl S, Dahlbom M, Wong KP, Fulham MJ, 'An investigation of coded aperture imaging for small animal SPECT', *IEEE Trans. Nucl. Sci.* 2001; 48: 816–821.

[3] McElroy DP, MacDonald LR, Beekman FJ, Wang Y, Patt BE, Iwanczyk JS, Tsui BMW, Hoffman EJ, 'Performance evaluation of A-SPECT: A high resolution desktop pinhole SPECT system for imaging small animals', *IEEE Trans. Nucl. Sci.* 2002; 49: 2139–2147.

[4] Metzler SD, Jaszczak RJ, Patil NH, Vemulapalli S, Akabani G, Chin BB, 'Molecular imaging of small animals with a triple-head SPECT system using pinhole collimation', *IEEE Trans. Med. Im.* 2005; 24 (7), 853–862.

[5] Schramm NU, Ebel G, Engeland U, Schurrat T, Béhé M, Behr TM, 'High-resolution SPECT using multipinhole collimation', *IEEE Trans. Nucl. Sci.* 2003; 50: 315–320.

[6] Lackas C, Schramm NU, Hoppin JW, Engeland U, Wirrwar A, Halling H, 'T-SPECT: A novel imaging technique for small animal research', *IEEE Trans. Nucl. Sci.* 2005; 52: 181–187.

[7] Goertzen AL, Jones DW, Seidel J, Li K, Green MV, 'First results from the high-resolution mouseSPECT annular scintillation camera', *IEEE Trans. Med. Im.* 2005; 24: 863–867.

[8] Meikle SR, Kench P, Kassiou M, Banati RB, 'Small animal SPECT and its place in the matrix of molecular imaging technologies', *Phys. Med. Biol.* 2005; 50: R45– R61.

[9] Peremans K, Cornelissen B, Bossche BVD, Audenaert K, Wiele CV, 'A review of small animal imaging, planar and pinhole spect gamma camera imaging', *Veterinary radiology and ultrasound.* 2005; 46: 162–170.

[10] Tsui BMW and Wang YC, 'High-resolution molecular imaging techniques for cardio-vascular research', *J. Nucl. Cardiol.* 2005; 12: 261–267.

[11] Beekman FJ and van der Have F, 'The pinhole: Gateway to ultra-high resolution three-dimensional radio-nuclide imaging', *Eur. J. Nucl. Med. Molec. Im.* 2007; 34(2): 151–161, 2007.

[12] Vunckx K, Bequé D, Defrise M, Nuyts J, 'Single and multipinhole collimator design evaluation method for small animal SPECT', *IEEE Trans. Med. Im.* 2008; 27(1): 36–46.

[13] Rowe RK, Aarsvold JN, Barrett HH, Chen JC, Klein WP, Moore BA, Pang IW, Patton DD, White TA, 'A stationary hemispherical SPECT imager for three-dimensional brain imaging', *J. Nucl. Med.* 1993; 34: 474–480.

[14] Liu Z, Kastis GA, Stevenson GD, Barrett HH, Furenlid LR, Kupinski MA, Patton DD, Wilson DW, 'Quantitative analysis of acute myocardial infarct in rat hearts with ischemia-reperfusion using a high-resolution stationary SPECT system', *J. Nucl. Med.* 2002; 43(7): 933–939.

[15] Furenlid LR, Wilson DW, Chen YC, Kim H, Pietraski PJ, Crawford MJ, Barrett HH, 'FastSPECT II: A second-generation high-resolution dynamic SPECT imager', *IEEE Trans. Nucl. Sci.* 2004; 51(3):631–635.

[16] Beekman FJ, van der Have F, Vastenhouw B, van der Linden AJA, van Rijk PP, Burbach JPH, Smidt MP, 'U-SPECT-I: A novel system for submillimeter-resolution tomography with radiolabeled molecules in mice', *J. Nucl. Med.* 2005; 46(7): 1194 –1200.

[17] Beekman FJ and Vastenhouw B, 'Design and simulation of a high-resolution stationary SPECT system for small animals', *Phys. Med. Biol.* 2004; 49: 4579–4592.

[18] Kastis GK, Barber HB, Barrett HH, Gifford HC, Pang IW, Patton DD, Stevenson G, Wilson DW, 'High resolution SPECT imager for three-dimensional imaging of small animals (abstract)', *J. Nucl. Med.* 1998; 39: 9P.

[19] Vastenhouw B, van der Have F, van der Linden AJA, von Oerthel L, Booij J, Burbach JPH, Smidt MP, Beekman FJ, 'Movies of dopamine transporter occupancy with ultra-high resolution focusing pinhole SPECT', *Molecular Psychiatry*. 2007; 12: 984–987.

[20] Ficaro EP, Fessler JA, Shreve PD, Kritzman JN, Rose PA, Corbett JR, 'Simultaneous transmission/emission myocardial perfusion tomography. Diagnostic accuracy of attenuation-corrected 99mTc-sestamibi single-photon emission computed tomography', *Circulation.* 1996; 93: 463–473.

[21] Beekman FJ, Kamphuis C, Frey EC, 'Scatter compensation methods in 3D iterative SPECT reconstruction: A simulation study', *Phys. Med. Biol.* 1997; 42: 1619–1632.

[22] Floyd CE, Jaszczak RJ, Greer KL, Coleman RE, 'Inverse Monte Carlo as a unified reconstruction algorithm for ECT', *J. Nucl. Med.* 1986; 27(10): 1577–1585.

[23] Kadrmas DJ, Frey EC, Karimi SS, Tsui BMW, 'Fast implementation of reconstruction based scatter compensation in fully 3D SPECT image reconstruction', *Phys. Med. Biol.* 1998; 43: 857–873.

[24] Tsui BMW, Frey EC, LaCroix KJ, Lalush DS, McCarthy WH, King MA, Gullberg GT, 'Quantitative myocardial perfusion SPECT', *J. Nucl. Card.* 1998; 5: 507–522.

[25] Metzler SD, Bowsher JE, Greer KL, Jaszczak RJ, 'Analytic determination of the pinhole collimator's point-spread function and RMS resolution with penetration', *IEEE Trans. Med. Im.* 2002; 21: 878–887.

[26] Bequé D, Nuyts J, Bormans G, Suetens P, Dupont P, 'Characterization of pinhole SPECT acquisition geometry', *IEEE Trans. Nucl. Sci.* 2003; 22(5): 599–612.

[27] Accorsi R and Metzler SD, 'Analytic determination of the resolution-equivalent effective diameter of a pinhole collimator', *IEEE Trans. Med. Im.* 2004; 23(6): 750–763.

[28] Li JY, Jaszczak RJ, Wang HL, Greer KL, Coleman RE, 'Determination of both mechanical and electronic shifts in cone-beam SPECT', *Phys. Med. Biol.* 1993; 38(6): 743–754.

[29] Rizo P, Grangeat P, Guillemaud R, 'Geometric calibration method for multiple-head cone-beam SPECT system', *IEEE Trans. Nucl. Sci.* 1994; 41(6): 2748–2757.

[30] Noo F, Clackdoyle R, Mennessier C, White TA, Roney TJ, 'Analytic method based on identification of ellipse parameters for scanner calibration in cone-beam tomography', *Phys. Med. Biol.* 2000; 45(11): 3489–3508.

[31] Bequé D, Nuyts J, Suetens P, Bormans G, 'Optimization of geometrical calibration in pinhole SPECT', *IEEE Trans. Med. Im.* 2005; 24(2): 180–190.

[32] Metzler SD, Greer KL, Jaszczak RJ, 'Determination of mechanical and electronic shifts for pinhole SPECT using a single point source', *IEEE Trans. Med. Im.* 2005; 24(3): 361–370.

[33] Metzler SD and Jaszczak RJ, 'Simultaneous multi-head calibration for pinhole SPECT', *IEEE Trans. Nucl. Sci.* 2006; 53(1): 113–120.

[34] Chen YC, Furenlid LR, Wilson DW, Barrett HH, 'Small-Animal SPECT imaging', *New York Springer.* 2005; ch. 12: 195–201.

[35] Hesterman JY, Kupinski MA, Furenlid LR, Wilson DW, Barrett HH, 'The multi-module, multi-resolution system (M3R): A novel small-animal SPECT system', *Med. Phys.* 2007; 34(3): 987–993.

[36] Vastenhouw B and Beekman FJ, 'Submillimeter total-body murine imaging with U- SPECT-I', *J. Nucl. Med.* 2007; 48(3): 487–493.

[37] van der Have F, Vastenhouw B, Rentmeester MCM, Beekman FJ, 'System calibration and statistical image reconstruction for sub-mm stationary pinhole SPECT', *Conference Record of the 2005 Nuclear Science Symposium and Medical Imaging Conference, Puerto Rico.* 2005: M11–291.

[38] van der Have F, Vastenhouw B, Beekman FJ, 'U-SPECT-II: a versatile sub-half-mm resolution small animal SPECT system', *Society of Nuclear Medicine conference.* 2007, Washington D.C., 2007.

[39] Beekman FJ, 'A method for obtaining a tomographic image, including an apparatus', *PCT-application WO02093195.* 2002, Submission May 8.

[40] ——, 'Werkwijze voor het verkrijgen van een tomografische afbeelding, alsmede een inrichting', *Dutch patents 1018060 and 1019666, US patent US7145153 B2 granted 2006-12-05*. 2001, Submission May 11.

[41] Richardson WH, 'Bayesian-based iterative method of image restoration', *J. Opt. Soc. Am.* 1972; 62: 55–59.

[42] Lucy LB, 'An iterative technique for the rectification of observed distributions', *Astron. J.* 1974; 79: 745–754.

[43] Colijn AP and Beekman FJ, 'Accelerated simulation of cone beam X-ray scatter projections', *IEEE Trans. Med. Im.* 2004; 23(5): 584–590.

[44] van der Have F and Beekman FJ, 'Photon penetration and scatter in micro-pinhole imaging: a Monte Carlo investigation', *Phys. Med. Biol.* 2004; 49: 1369–1386.

[45] Press WH, Flannerly BP, Teukolsky SA, Vetterling WT, 'Numerical Recipes in C'. *Cambridge University Press.* 1988.

Chapter 4

Submillimeter total-body murine imaging with U-SPECT-I

Brendan Vastenhouw and Freek J. Beekman

The Journal of Nuclear Medicine, 2007; 48: 487-493.

Abstract

Recently, we launched a stationary SPECT system (U-SPECT-I) dedicated to small-animal imaging. A cylinder with 75 gold micropinhole apertures that focus on a mouse organ was used to maximize the detection yield of gamma-photons. Image resolutions of approximately 0.45 and 0.35 mm could be achieved with 0.6 mm and 0.3 mm pinholes, respectively. Here, we present a combined acquisition and reconstruction strategy that allowed us to perform full-body imaging with U-SPECT-I. **Methods:** The bed was stepped in the axial and transaxial directions so that the pinholes collected photons from the entire animal (scanning focus method, or SFM). Next, a maximum-likelihood expectation maximization algorithm exploited all projections simultaneously to reconstruct the entire volume sampled. The memory required for image reconstruction was dramatically reduced by using the same transition submatrix for each of the bed positions. This use of the same submatrix was possible because the submatrix acted on subvolumes that were shifted during reconstruction to match the corresponding location of the focus. **Results:** In all cases, SFM clearly improved on the method that involves stitching separate reconstructions of subvolumes obtained from the different bed positions. SFM suffered less from noise, streak artifacts, and improper background activity. In a mouse-sized phantom containing a capillary-resolution insert, sets of radioactively filled capillaries as small as 0.45 mm separated by 0.45 mm could be distinguished. Total-body mouse bone imaging using 99mTc-hydroxymethylene diphosphonate showed that uptake in very small structures, such as parts of the vertebral processes, could be distinguished. **Conclusion:** In addition to providing ultra-high resolution images of mouse organs, focusing SPECT pinhole systems are also suitable for submillimeter resolution total-body imaging of mice.

Introduction

Dedicated Single Photon Emission Computed Tomography (SPECT) and Positron Emission Tomography (PET) instruments [1] in concert with the radiolabeling of small molecules, antibodies, peptides, and probes for gene expression have facilitated the *in vivo* assessment of molecular mechanisms and the development of new tracers and pharmaceuticals [2-8]. Small animal SPECT systems are typically based on the pinhole imaging principle [9-24]. With micropinhole radionuclide imaging it becomes possible to obtain high spatial resolution projection data, particularly in small organs that can be positioned close to the pinholes. Until recently the drawback of most pinhole SPECT systems compared to PET was their limited ability to detect a significant fraction of the emitted gamma-photons, particularly when small pinholes are used. Several groups proposed methods that use multiple pinholes to obtain a high sensitivity [17-27].

Recently, we introduced novel stationary SPECT systems (U-SPECT) dedicated to small animal imaging. The U-SPECT systems maximize the sensitivity by focusing the pinholes on a small area, just big enough to contain the tissue of interest [10,18,19]. The focusing designs allow for large magnification of the object under investigation, enabling one to exploit the high resolution content of pinhole projection data even when low-cost, commonly available clinical Anger cameras are used. Similar to FastSPECT-I and -II (introduced by the University of Arizona [23,24]), U-SPECT-I is stationary in the sense that there is no need to move any of the parts such as the detector, the collimator or the animal. These stationary systems have advantages with respect to (i) system stability, (ii) simplicity of the system design, (iii) flexibility to perform dynamic studies with any frame-time [18,19,25,28], and (iv) animal handling and positioning.

So far, submillimeter images were only obtained with U-SPECT-I for a limited volume of interest, for instance the heart or the brain of a mouse. The goal of the present work is to present and evaluate a combined acquisition/reconstruction method that drastically extends the reconstructed field-of-view even up to full-body imaging. The method is validated using simulation studies, physical phantom experiments as well as total-body *in vivo* mouse imaging.

Materials and Methods

In this section we briefly summarize the design of U-SPECT-I, describe the acquisition method for total-body imaging and describe the image reconstruction methods used. The simulation and physical phantom experiments performed will be explained, as well as the animal studies used to validate the system performance.

Design and geometry of U-SPECT-I

Figure 1A shows an overview of the U-SPECT-I system, in which the detectors of a triple head SPECT system surround the pinhole apertures. A tungsten cylinder containing 75 gold pinholes (figure 1B) is mounted in the center of the triangle and acts as a collimator. Each pinhole projects onto a separate part of the detector area, which results in 69 independent pinhole cameras (some pinholes illuminate a dead area). Overlap of the projections is prevented by placing a lead tube with 75 rectangular holes around the tungsten pinhole cylinder. Details of the system design and the collimation are described in [19].

Two collimator tubes are currently available, one containing 0.3 mm pinholes and one with 0.6 mm pinholes. Recent results show that an image resolution of approximately 0.45 mm can be reached with 0.6 mm pinholes and resolutions below 0.35 mm are reachable when 0.3 mm pinholes are mounted [10,29]. However, because a relative high sensitivity is required for total-body imaging, the 0.6 mm pinholes are used for all studies and simulations in this chapter.

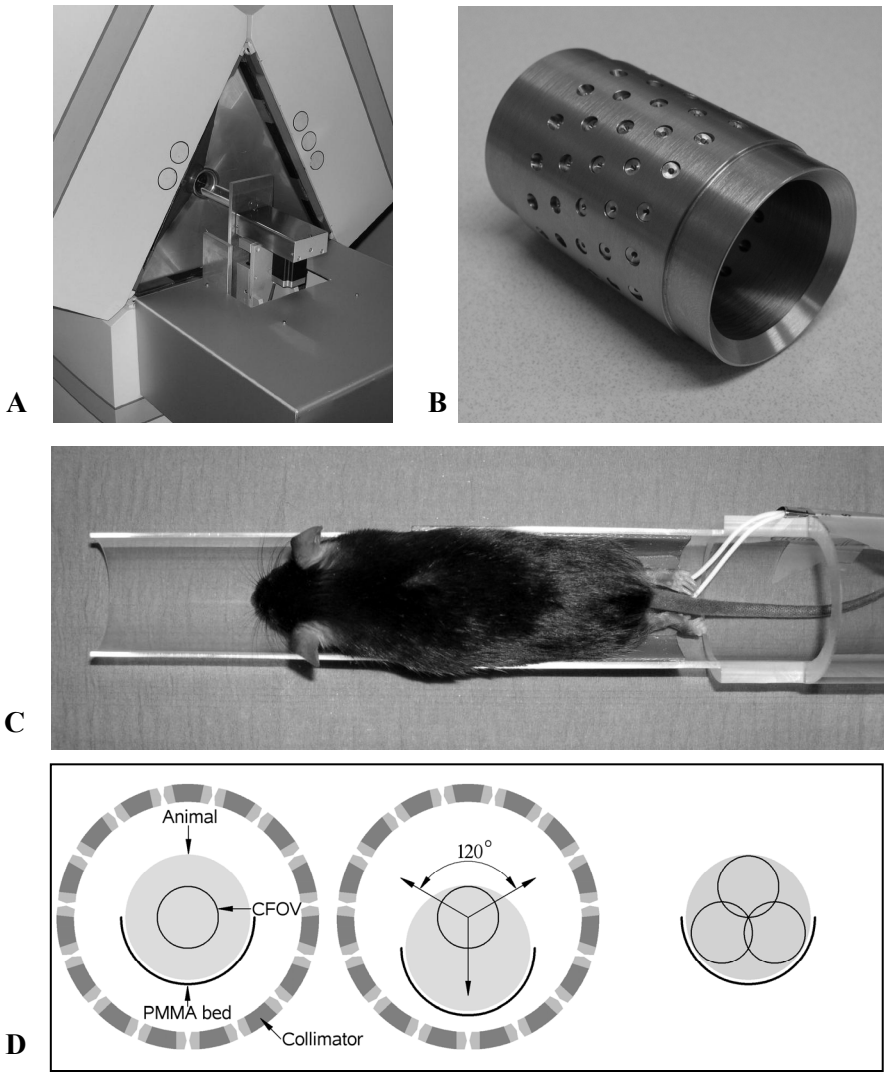

Figure 1: (A) Overview of the U-SPECT-I system. A triangular-shaped lead shielding with a cylindrical pinhole collimator is placed in a triple detector set-up. The XYZ-stage with a bed attached, is placed in front of the detectors to accurately transport the animal through the collimator tube. (B) The tungsten collimator with 75 gold pinholes. (C) Thin-walled half-cylindrical PMMA bed with heating mat. (D) (Left) Cross section through the collimator (inner diameter 41 mm) and the animal on top of the bed. The inner circle represents the central-field-of-view (CFOV). (Middle) When the bed is positioned in the lower part of the collimator, the CFOV is located in the upper part of the animal. (Right) With 3 focus positions one can cover almost the entire animal with the CFOV.

Scanning focus acquisition

The animal to be scanned is placed on a thin half-cylindrical PMMA bed (figure 1C). The cylindrical shaped central-field-of-view (CFOV) is shown in figure 1D (left). This area (approximately 11 mm diameter and 10 mm length) indicates the extent of the imaging space that is visible through all pinholes, which allows for proper image reconstruction. Note that complete data in the sense of Orlov is also available in the immediate neighborhood of the CFOV, which explains that not each point to be reconstructed needs to be located exactly inside the CFOV. It is obvious that the CFOV does not cover the entire animal (figure 1D (left)). However, by translating the bed towards the bottom of the pinhole tube, the CFOV is repositioned more towards the upper part of the animal (figure 1D (middle)). In this respect, repositioning of the bed inside the pinhole cylinder is equivalent to repositioning the CFOV within the animal.

During acquisition, the focus steps through the animal using a motor-controlled XYZ stage. This enables us to collect a sufficient number and variety of projections from all parts of the animal.

Image reconstruction

Image reconstruction for the U-SPECT system is performed using Maximum Likelihood Expectation Maximization (ML-EM, [30]). The activity distribution $\boldsymbol{a}$ is estimated from the matrix equation: $\boldsymbol{p} = \boldsymbol{ma} + \boldsymbol{n}$, with $\boldsymbol{p}$ the projection data, $\boldsymbol{m}$ the matrix that projects the activity distribution onto the projections and $\boldsymbol{n}$ the noise in the projections. The matrix elements $\boldsymbol{m}_{ji}$ represent the probability that a photon emitted in voxel i is detected in pixel j. These elements are measured with a point source and only nonzero elements are stored on disk [19,29].

When multiple focus positions are used to extend the field-of-view, there are several ways to reconstruct the entire volume sampled. For example, parts of the activity distribution associated with each focus position can be reconstructed independently, followed by stitching of these subvolumes to obtain the overall volume. However, the extra information in a subvolume of the activity distribution which is also available from other focus positions is not fully exploited in this way. Lack of complete data in the outer parts of an individual reconstruction can even lead to artifacts at the edges of the subvolume, which will also be present in the final stitched volume.

An alternative to stitching is to exploit all acquired projections simultaneously for reconstructing the complete volume scanned. The combination of scanning multiple focus positions and simultaneous reconstruction of all projection data is referred to as the Scanning Focus Method (SFM). The reconstruction problem can then be written in matrix form as shown in figure 2, using a matrix $\boldsymbol{M}$ that is much larger than matrix $\boldsymbol{m}$. However, $\boldsymbol{M}$ can be divided into smaller submatrices $\boldsymbol{m}^{(k)}$ corresponding to the part in focus for the different bed positions. Matrix elements of submatrix $\boldsymbol{m}_{ji}^{(k)}$ represent the probability that a photon emitted in voxel i is detected in pixel j for bed position k. Here, $\boldsymbol{a}$ again denotes the activity in voxels which are now

distributed over the entire mouse and $\boldsymbol{p}^{(k)}$ contains the projection data obtained at focus position k.

The submatrix $\boldsymbol{m}^{(k)}$ acts on part of the activity distribution $\boldsymbol{a}$ and projects exclusively to the projection set $\boldsymbol{p}^{(k)}$ acquired in bed position k. In principle, a different submatrix $\boldsymbol{m}^{(k)}$ is needed for each of the k focus positions. However, when we restrict the shifts of the focus positions to an integer times the voxel size, the reconstruction can be performed with the same submatrix $\boldsymbol{m}$ when the forward-projection and the back-projection act on a shifted voxel volume [31]. This, in combination with sparse matrix storage, reduces the total memory requirements from 6.4 terabytes (for brute force storage of all matrix elements of $\boldsymbol{M}$) to approximately 4 gigabytes (for storing only $\boldsymbol{m}$), which easily fits in the memory of a modern computer.

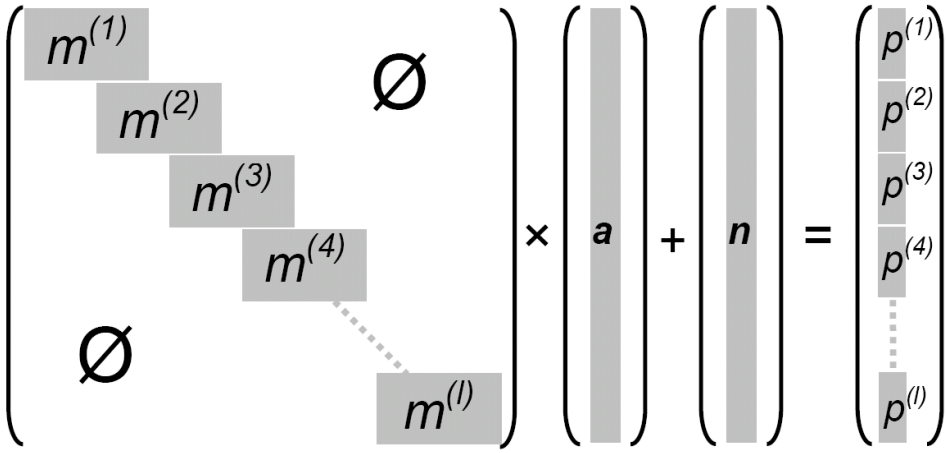

Figure 2: Matrix representation of the statistical reconstruction problem with multiple focus positions *(1), …, (l)*.

The reconstructed images obtained with the stitching method are compared with the images reconstructed using SFM. Prior to image reconstruction, the projections were corrected for decay. Reconstruction for SFM is performed using 150 iterations of the ML-EM algorithm employing all shifted volumes. For stitching, each subvolume is reconstructed separately, again using 150 iterations of standard ML-EM. After reconstruction, the data from the individual subvolumes is combined to form the complete stitched volume. For the stitching of the subvolumes, the following procedure is used: If a voxel is in the CFOV for one of the subvolumes, it is copied to the stitched volume. When a certain voxel is present in the CFOV of more subvolumes, its value is averaged over all available subvolumes. This will be the case when the CFOV's of the different positions overlap. If a voxel is not in the CFOV of any subvolume, we take the voxel from the subvolume of which the distance to the CFOV is smallest.

The voxel size used for reconstructions was 0.1875 mm^3 and the projection pixel size used for all measurements was 0.9 mm. Better images are often obtained by over iterating followed by filtering than by early stopping (e.g. [32,33]). In this case, the reconstructions are post-filtered using a three-dimensional Gaussian with an FWHM of 0.375 mm. Attenuation and scatter of photons in the object are not modeled in the current system, since these two phenomena are expected to be negligible for small objects such as mice.

No acceleration techniques such as ordered subsets are used. Currently, with non-optimized code the time required for reconstruction using a computer with a 2 GHz AMD Opteron processor and a voxel grid of 0.1875 mm^3, is approximately 18 minutes for a single position and approximately 330 minutes for a total-body scan consisting of 60 positions. However, these reconstruction times dramatically decrease by using a coarser grid: for example a speed up with an order of magnitude can be achieved by using a voxel size of 0.375 mm^3.

Phantom studies

Digital mouse phantom

For a simulation study of a mouse bone scan, we used the digital mouse whole-body phantom (MOBY, [34]). The CFOV of the system is approximately 1 ml, so about 30 focus positions are needed to cover the entire mouse body. Data were simulated for two protocols having different numbers of bed positions, but the total acquisition time was one hour for both cases. The first protocol had a total of 36 focus positions (with 100 seconds acquisition per bed position). Twelve different axial positions were used. At each axial position three transaxial bed positions were employed, all three at a distance of 5 mm from the center separated by an angle of 120 degrees: the first directed downwards, the second to the upper right and the third to the upper left (as indicated by the arrows in figure 1D (middle)). The positions of the CFOV in the animal corresponding with these translations are show in figure 1D (right). For a second protocol, the same three transaxial translations are used but the number of axial positions was increased to twenty, resulting in a total of 60 bed positions (with 60 seconds acquisition at each position).

Physical uniform phantom

The uniformity of a scan consisting of multiple focus positions was tested by scanning a large uniformly filled phantom (figure 3A). A Perspex cylinder with an inner diameter of 18 mm and 50 mm length (approximately the size of a small mouse body) was filled with 450 MBq of Tc-99m and scanned for one hour using 60 focus positions. The same positioning scheme was used as described above for the digital mouse phantom study with 60 positions.

Physical resolution phantom

A miniature resolution phantom (”Derenzo phantom”) was used in this study (figure 3B). This Perspex insert has six sectors; each sector contains a set of equal-sized capillaries (0.35, 0.4, 0.45, 0.5, 0.6 and 0.75 mm). The distance between the rods in a sector equals the rod diameter in that sector. The outer diameter of the insert is 12 mm and each capillary is 10 mm long. The spatial resolution is often defined by the size of capillaries that can be observed separately in such phantoms.

A phantom was constructed to test the spatial resolution for total-body scanning. This phantom (figure 3C) consists of a uniformly filled cylinder containing a cylindrical holder (figure 3D) with the resolution insert inside. This setup was filled in such a way that activity concentrations are comparable to those in the animal bone study (using 470 MBq) described in the next subsection. The concentrations were derived as follows: The total bone mass of a mouse is approximately 3 percent of its total weight [35], and the uptake in the bone is about 50 percent of the administered activity [36]. A 32 gram mouse will have approximately 0.53 cm^3 bone (density of bone is approximately 1.8 g/cm^3) containing half the injected activity, so the activity concentration in the bone is 441 MBq/cm^3. The capillaries of the resolution insert were filled with this concentration (in total 39 MBq is present, divided over all capillaries) to represent small bone structures of the animal. The large cylinder was filled with 120 MBq to represent the background activity present in other tissues.

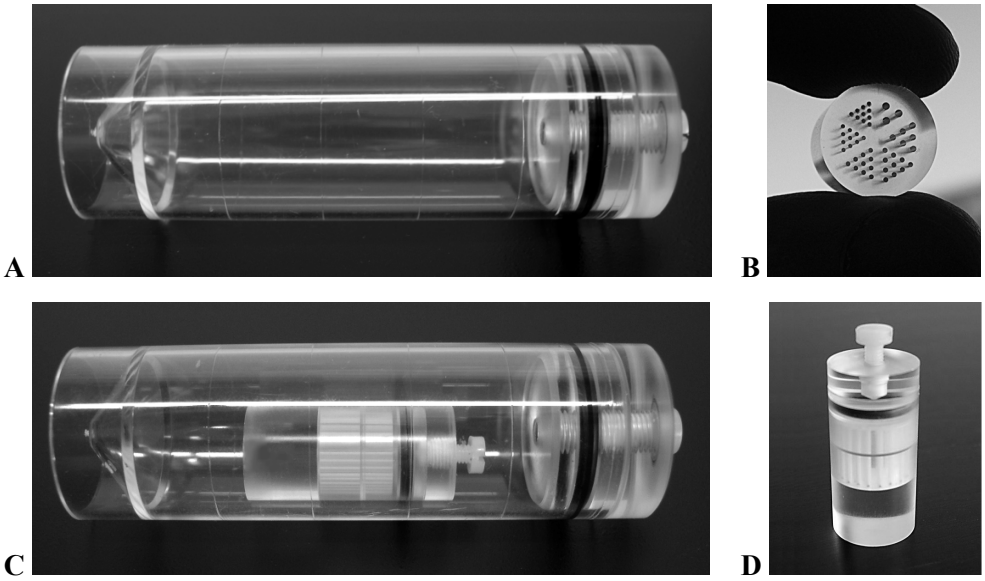

Figure 3: (A) Uniformly filled cylinder phantom. (B) Miniature resolution insert. (C) Total-body phantom consisting of a uniformly filled cylinder with a resolution phantom inside. (D) Resolution phantom: a small holder containing the resolution insert.

Animal studies

A total-body mouse bone scan with 470 MBq Tc-99m hydroxy-methylene diphosphonate (Tc-99m-HDP) was performed using 60 focus positions. The total acquisition time was one hour. The animal study was conducted following protocols as approved by the Animal Research Committee of the University Medical Center Utrecht. A 4½ month old mouse (C57BL/6JO1aHsd, Harlan, The Netherlands) of 32 gram was anesthetized with a mixture of 2.5 ml/kg Hypnorm (Janssen, fentanyl 0.315 mg/ml and fluarisone 10 mg/ml), 2.5 ml/kg dormicum (Roche; midazolam 5 mg/ml) and 5 ml/kg aquadest i.p. The Tc-99m-HDP (concentrated in a total volume of 0.2 ml) was injected in the tail vein of the animal. Two hours and 15 minutes after injection, the acquisition started. During the entire procedure the animal body temperature was kept at ± 37 degrees Celsius using a thin heating mat under the mouse body (figure 1C).

We like to note that radiation dose issues in small animal SPECT imaging can be important [37], particularly in longitudinal studies. Therefore we emulated a scan with a more than ten times lower activity than used in our animal study; the projection data of the animal study were down-scaled by a factor of ten (by multiplying each pixel with a factor of 0.1) after which Poisson noise was generated. The reconstructed images obtained in this way, will have the animal in exactly the same position as the reconstruction of the original data, which allows for direct comparison.

Results

Simulated total-body bone scan

The results of the simulated bone scan are presented in figure 4. Maximum intensity projections are shown for SFM and stitched reconstructions for 36 focus positions (top) and 60 focus positions (bottom). It is clear that noise, streak artifacts and improper background activity have all been reduced when SFM is used instead of stitching. For both methods, the images from a large number of positions suffer slightly less from reconstruction artifacts and have a higher contrast than the images obtained with a small number of positions, if the total acquisition time is kept equal. To quantify the magnitude of the stitching artifacts, we calculated the Mean Square Error (MSE) between the know configuration of the phantom and the images produced by each of the four different types of reconstruction (figure 4). The MSE of the SFM based reconstructions was typically 300 to 500 times lower than for stitched reconstructions.

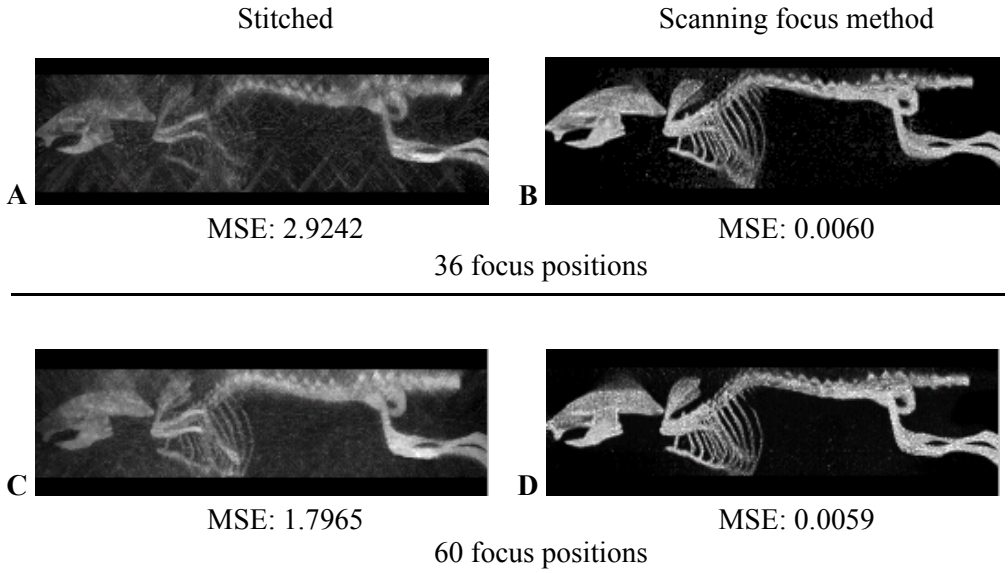

Figure 4: Maximum intensity projections of the reconstructed images obtained with SFM (B and D) show significant improvements compared to stitched reconstructions (A and C).

Phantom experiments

Both transaxial and axial slices through the reconstructed images of the homogeneously filled cylinder phantom are shown in figure 5. SFM clearly outperforms stitching, showing better overall uniformity. The total acquisition time was 60 minutes for both methods.

A slice of the reconstructed total-body resolution phantom and a profile through this slice are presented in figure 6. One can resolve the set of 0.45 mm capillaries of the miniature resolution insert. The image was obtained using SFM with 60 positions.

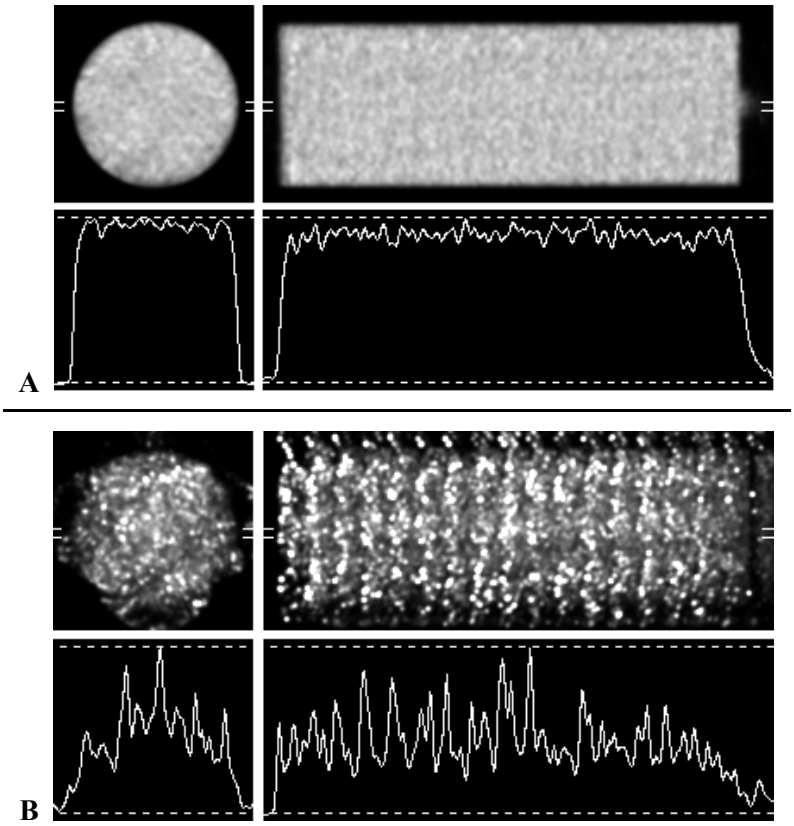

Figure 5: Reconstructed images (and image profiles) of a uniformly filled cylinder obtained using 60 focus positions. (A) scanning focus method. (B) stitching.

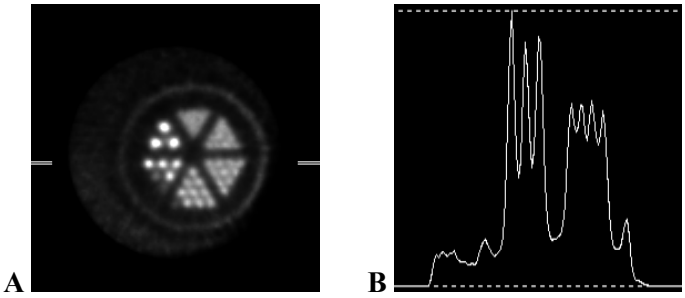

Figure 6: (A) Reconstruction of the total-body phantom: 0.375 mm thick slice showing the resolution insert in the phantom. (B) Profile through the sections with 0.6 and 0.45 mm capillaries. (Note that not all capillaries were properly filled in the lower left part of the insert).

Animal studies

Total-body mouse images with Tc-99m-hydroxy-methylene diphosphonate (Tc-99m HDP) are shown in figure 7. For visualization purposes of these maximum intensity projections, the hot bladder has been removed from the volume. This was done by segmenting the bladder with a region growing algorithm and setting the voxels in the segmented volume to zero. High uptake of HDP in the liver of the animal is visible. Small details of the skeleton are clearly defined: For example, uptake down to the level of vertebral processes, ribs, and tiny joints can be readily distinguished. Slices through the volume confirm the high resolution obtained with the SFM method (figures 8A and 8B). The slice thickness was 0.75 mm for both images (four reconstructed slices of 0.1875 mm each were summed to obtain the 0.75 mm thick slices).

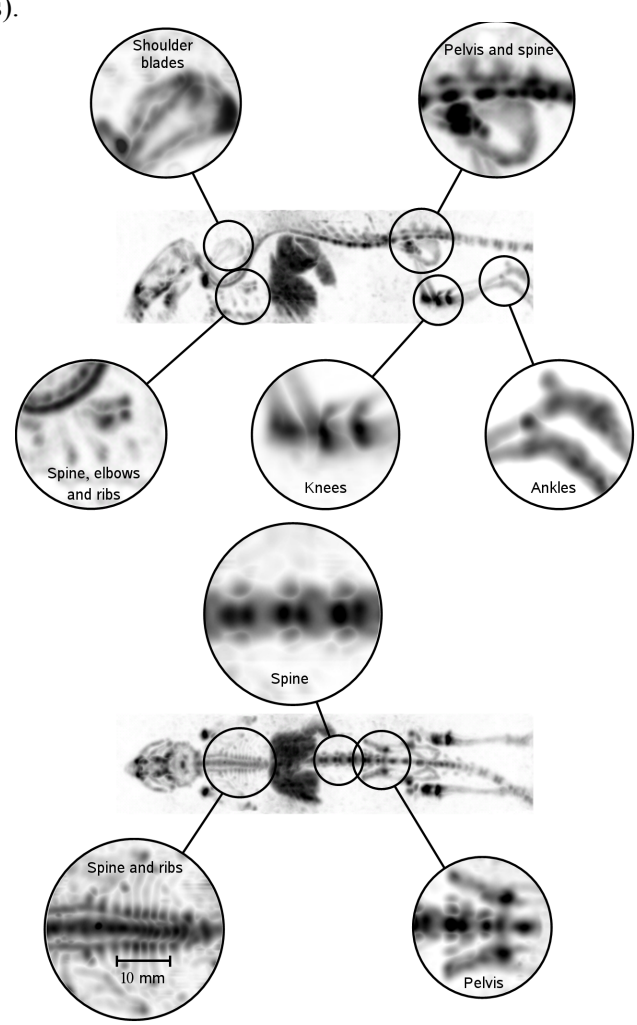

Figure 7: Total-body bone scan of a living mouse acquired using 470 MBq Tc-99m HDP with 60 focus positions.

Figure 8 also shows the effects of having a more than ten times lower dose than used for creating the image in figure 7. This “lower dose” study was derived from the high count mouse data by down scaling the projection data by a factor ten, followed by adding Poisson noise. Since the high count study was not noise free, the projections contain slightly more noise than a study with an exactly ten times lower dose. Particularly thin structures like the shoulder blades and small bones are visually affected by the lower dose.

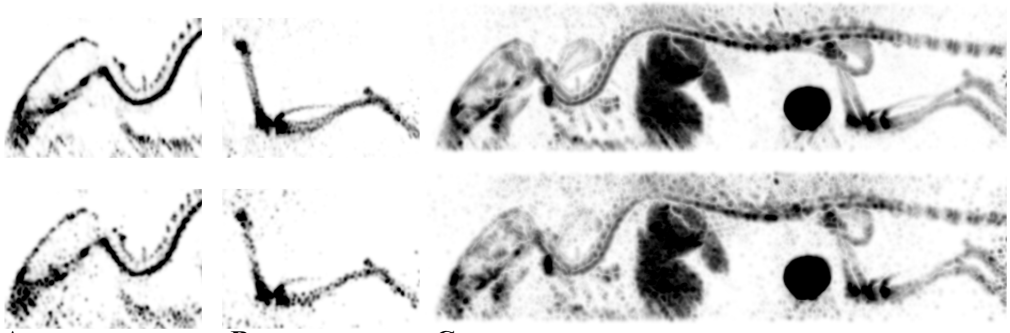

Figure 8: Top: High count study using 470 MBq Tc-99m HDP (reference). Bottom: Emulated low dose study. Slices through the head (A) and leg (B) and maximum intensity projections of the complete volume (C) show a high level of detail in the skeleton of a living mouse for both cases.

Discussion

The highly focusing design of the U-SPECT-I system has unsurpassed sensitivity in a field-of-view large enough for imaging small animal organs. As a result, very high resolution animal images have been produced with this system. Initial critics were concerned about the limited field-of-view. With the scanning focus method proposed in the present chapter, we have shown that highly focusing SPECT systems are also suitable for imaging larger volumes up to total-body animal imaging.

The stationary set-ups of systems such as U-SPECT and Fast-SPECT are very suitable for dynamic imaging [19]. Fast dynamic imaging of an area larger than the field-of-view (covered by a single bed position) is also possible: Since the translations of the mouse bed are small, the bed can be shifted from one focus position to another in a very short period of time. For example, when an area has to be imaged in six positions one needs less than six seconds for the bed movement. This means that for a dynamic study with a time resolution of one minute, only 10 % of the acquisition time is lost. In most dynamic studies (such as in the heart, brain, or in tumors) fewer positions are required, which indicates that even a sub-minute time resolution is possible with SFM.

In a few aspects, SFM is related to the T-SPECT technique described in [22]. Both methods use multipinhole collimation where the detectors are placed in a stationary setup and only the object under investigation is translated. For the T-SPECT system, the object is moved within the field-of-view to increase the sampling information needed for reconstruction, while our primary goal for using translations is to extend the field-of-view of the U-SPECT system. Both methods have the advantage that the heavy detectors don't have to be translated or rotated.

In addition to the *in vivo* mouse study using Tc-99m-HDP, we have shown that 0.45 mm capillaries can still be distinguished in a mouse body-size phantom. The activity concentrations in this phantom were representative for a mouse bone study with 470 MBq Tc-99m-HDP.

We are currently developing an additional pinhole tube for rat imaging. A total of two tubes will be sufficient to perform imaging of mouse and rat organs like heart and brain without moving the animal or detectors at all. With semistationary protocols such as SFM it is possible to perform larger field-of-view imaging studies up to total-body rat imaging. Dedicated acquisition software has recently been developed in our lab. This software contains a method to synchronize projection acquisition with the bed movement as well as the automatic calculation of the sequence of bed positions needed to scan a specified volume-of-interest. This makes extended field-of-view imaging with SFM very user friendly and accurate.

Correction for attenuation and scatter of photons in the object was not applied, since these two effects are often small in animal imaging, for the majority of isotopes used. However, in the case of I-125, which emits photons of only approximately 30 keV), the images can be seriously affected by attenuation. When a density distribution of the object is available (i.e. from a registered microCT scan) methods for attenuation and scatter correction can be implemented.

The reconstruction software we developed for the use with SFM does not impose any restrictions on the scanning scheme; only the coordinates for each focus position are required. An efficient implementation of the ML-EM algorithm shifts the reconstruction volume to match the focus. Even with a large number of focus positions, the reconstruction time does not increase dramatically, since the re-projection data for all voxels shifted to one position can be generated in parallel. However, we will explore how reconstruction time can be decreased, for example by using block-iterative methods in image reconstruction [38-40]. We expect that the required reconstruction time of several hours could be reduced significantly to about ten minutes. This estimation follows from the fact that acceleration factors of 10 to 20 are typical when the ordered subset algorithm is applied in emission computed tomography. Another means of acceleration concerns the sequence of bed positions. The present acquisition scheme is based on three different transaxial bed positions per axial bed position. One could also try other orbits where each point on the bed describes a spiral, possibly requiring fewer bed positions. This may not reduce the total acquisition time, but it could result in improved sampling of each point in the animal or faster reconstruction since fewer re-projections need to be generated.

Conclusion

Previously we have shown that U-SPECT-I allows for discriminating between molecular concentrations in adjacent volumes as small as about 0.1-0.04 microliters, depending on the pinhole diameters used [19,29,31]. In simulation studies and experiments using both phantoms and mice we have been able to demonstrate that U-SPECT-I is capable of total-body imaging with a resolution better than 0.5 mm. The ML-EM algorithm developed for this goal was compared to stitching of the individually ML-EM reconstructed subvolumes and is found to be superior in terms of noise, contrast, lack of streak artifacts and improper background activity as well as computer memory required.

Acknowledgements

This work was sponsored by the Medical Council of Netherlands Organization for Scientific Research, grant 917.36.335. We are grateful to Frans van der Have for technical assistance and fruitful discussions. We would like to thank Annemarie van der Linden, Henk te Biesebeek and Kees van der Linden for technical support.

References

[1] King MA, Pretorius PH, Farncombe T, Beekman FJ, 'Introduction to the physics of molecular imaging with radioactive tracers in small animals', *J. Cell. Biochem.*, 2002; suppl. 39: 221–230.

[2] Gambhir SS, Herschman HR, Cherry SR, et al., 'Imaging transgene expression with radionuclide imaging technologies', *Nature Neoplasia.* 2000; 2(1): 118–138.

[3] Phelps ME, 'Inaugural article: positron emission tomography provides molecular imaging of biological processes', *Proc. Natl. Acad. Sci. USA.* 2000; 97: 6226–6233.

[4] Weissleder R, 'Scaling down imaging: molecular mapping of cancer in mice', *Nature Rev. Cancer.* 2002; 2(1): 11–18.

[5] Rudin M, Weissleder R, 'Molecular imaging in drug discovery and development', *Nature Rev. Drug. Discov.* 2003; 2(2): 123–31.

[6] Shah K, Jacobs A, Breakefield XO, Weissleder R, 'Molecular imaging of gene therapy for cancer', *Gene Ther.* 2004; 11(15): 1175–1187.

[7] Chatziioannou A, 'Molecular imaging of small animals with dedicated PET tomographs', *Eur. J. Nucl. Med. Mol. Im.* 2002; 29: 98–114.

[8] Yang Y, Tai YC, Siegel S, et al., 'Optimization and performance evaluation of the microPET II scanner for *in vivo* small-animal imaging', *Phys. Med. Biol.* 2004; 49(12): 2527–2545.

[9] Jaszczak RJ, Li J, Wang H, Zalutsky MR, Coleman RE, 'Pinhole collimation for ultra-high-resolution small-field-of-view SPECT', *Phys. Med. Biol.* 1994; 39: 425–37.

[10] Beekman FJ, van der Have F, 'The pinhole: gateway to ultra-high resolution three-dimensional radio-nuclide imaging', *Eur. J. Nucl. Med. Mol. Im.* 2007; 34: 151–161.

[11] Beekman FJ, McElroy DP, Berger F, Gambhir SS, Hoffman EJ, Cherry SR, 'Towards *in vivo* nuclear microscopy: I-125 imaging in mice using micro-pinholes', *Eur. J. Nucl. Med. Mol. Im.* 2002; 29(7): 933–938.

[12] Wu MC, Tang HR, Gao DW, et al., 'ECG gated pinhole SPECT in mice with millimeter resolution', *IEEE Trans. Nucl. Sci.* 2000; 47: 1218–1227.

[13] Meikle SR, Kench P, Kassiou M, Banati RB, 'Small animal SPECT and its place in the matrix of molecular imaging technologies'. *Phys. Med. Biol.* 2005; 50(22): R45-R61.

[14] Meikle SR, Fulton RR, Eberl S, Dahlbom M, Wong KP, Fulham MJ, 'An investigation of coded aperture imaging for small animal SPECT', *IEEE Trans. Nucl. Sci.* 2001; 48 (3): 816-821.

[15] McElroy DP, MacDonald LR, Beekman FJ, et al., 'Performance evaluation of A-SPECT: A high resolution desktop pinhole SPECT system for imaging small animals', *IEEE Trans. Nucl. Sci.* 2002; 49: 2139–2147.

[16] Pani R, Pellegrini R, Cinti MN, et al., 'New devices for imaging in nuclear medicine', *Cancer Biother. Radio.* 2004; 19(1): 121–128.

[17] Ishizu K, Mukai T, Yonekura Y, et al., 'Ultra-high-resolution SPECT system using four pinhole collimators for small animal studies', *J. Nucl. Med.* 1995; 36: 2282–2289.

[18] Beekman FJ, Vastenhouw B, 'Design and simulation of a high-resolution stationary SPECT system for small animals', *Phys. Med. Biol.* 2004; 49: 4579–4592.

[19] Beekman FJ, van der Have F, Vastenhouw B, van der Linden AJA, van Rijk PP, Burbach JPH, Smidt MP, 'U-SPECT-I: A Novel System for Submillimeter-Resolution Tomography with Radiolabeled Molecules in Mice' *J. Nucl. Med.* 2005; 46(7): 1194-1200.

[20] Metzler SD, Jaszczak RJ, Patil N.H. Vemulappalli S, Akabani G, Chin BB, 'Molecular Imaging of Small Animals With a Triple-Head SPECT System Using Pinhole Collimation', *IEEE Trans. Med. Im.* 2005; 24(7): 853-862.

[21] Schramm NU, Ebel G, Engeland U, Schurrat T, Béhé M and Behr TM, 'High-Resolution SPECT Using Multipinhole Collimation', *IEEE Trans. Nucl. Sci.* 2003; 50(3): 315-320.

[22] Lackas C, Schramm NU, Hoppine JW, et al., 'T-SPECT: A Novel Imaging Technique for Small Animal Research', *IEEE Trans. Nucl. Sci.* 2005; 52(1): 181-187.

[23] Furenlid LR, Wilson DW, Chen YC, Kim H, Pietraski PJ, Crawford MJ, Barrett HH, 'FastSPECT II: A second-generation high-resolution dynamic SPECT imager', *IEEE Trans. Nucl. Sci.* 2004; 51(3): 631-635.

[24] Kastis GK, Barber HB, Barrett HH, Gifford HC, Pang IW, Patton DD, Sain JD, Stevenson GD, Wilson GW, 'High resolution SPECT imager for three-dimensional imaging of small animals (abstract)', *J. Nucl. Med.* 1998; 39 (5-suppl): 9.

[25] Rowe RK, Aarsvold JN, Barrett HH, et al., 'A stationary hemispherical SPECT imager for three-dimensional brain imaging', *J. Nucl. Med.* 1993; 34: 474–480.

[26] Rogulski MM, Barber HB, Barrett HH, Shoemaker RL, Woolfenden JM, 'Ultra-high-resolution brain SPECT: simulation results', *IEEE Trans. Nucl. Sci.* 1993; 40: 1123-29.

[27] Cao Z, Bal G, Accorsi R, Acton PD, 'Optimal number of pinholes in multi-pinhole SPECT for mouse brain imaging - a simulation study', *Phys. Med. Biol.* 2005; 50(19): 4609-24.

[28] Liu Z, Kastis GA, Stevenson GD, et al., 'Quantitative analysis of acute myocardial infarct in rat hearts with ischemia-reperfusion using a high-resolution stationary SPECT system' *J. Nucl. Med.* 2002; 43(7): 933–939.

[29] van der Have F, Vastenhouw B, Rentmeester M, Beekman FJ, 'System Calibration and Statistical Image Reconstruction for Sub-mm Stationary Pinhole SPECT', *Conference Record of the 2005 Nuclear Science Symposium and Medical Imaging.* 2005; M11-291: 2653-2658.

[30] Lange K, Carson R, 'E.M. reconstruction algorithms for emission and transmission tomography', *J. Comput. Assist. Tomo.* 1984; 8: 306–316.

[31] Beekman FJ, Vastenhouw B, van der Have F, 'Towards 3D nuclear microscopy using locally focusing many-pinhole SPECT', *Proceedings of the 2003 International Meeting on Fully Three-Dimensional Image Reconstruction in Radiology and Nuclear Medicine. 2003,* PM1-6.

[32] Miller TR, Wallis JW, 'Clinically important characteristics of maximum-likelihood reconstruction', *J. Nucl. Med.* 1992; 33(9): 1678-1684.

[33] Beekman FJ, Slijpen ETP, Niessen WJ, 'Selection of task-dependent diffusion filters for the post-processing of SPECT images', *Phys. Med. Biol.* 1998; 43(6): 1713-1730.

[34] Segars WP, Tsui BMW, Frey EC, Johnson GA, Berr SS, 'Development of a 4D digital mouse phantom for molecular imaging research', *Mol. Imaging. Biol.* 2004; 6(3): 149-159.

[35] Lochmuller EM, Jung V, Weusten A, Wehr U, Wolf E, Eckstein F, 'Precision of high-resolution dual energy X-ray absorptiometry of bone mineral status and body composition in small animal models', *Eur. Cell. Mater.* 2001; 1: 43-51.

[36] Davis MA, Jones AL, 'Comparison of 99mTc-labeled phosphate and phosphonate agents for skeletal imaging', *Semin. Nucl. Med.* 1976; 6(1): 19-31.

[37] Funk T, Sun M, Hasegawa BH, 'Radiation dose estimate in small animal SPECT and PET', *Med. Phys.* 2004; 31(9): 2680-2686.

[38] Hudson HM, Larkin RS, 'Accelerated image reconstruction using ordered subsets of projection data', *IEEE Trans. Med. Im.* 1994; 13: 601-609.

[39] Hutton BF, Hudson HM, Beekman FJ, 'A Clinical Perspective of Accelerated Statistical Reconstruction', *Eur. J. Nucl. Med.* 1997; 4: 797-808.

[40] Leahy RM, Byrne CL, 'Recent Developments in iterative Image Reconstruction in PET and SPECT', *IEEE Trans. Med. Im.* 2000; 19: 257-260.

Chapter 5

U-SPECT-II: an ultra-high resolution device for molecular small-animal imaging

Frans van der Have, Brendan Vastenhouw, Ruud M. Ramakers, Woutjan Branderhorst, Jens O. Krah, Changguo Ji, Steven G. Staelens and Freek J. Beekman

Submitted.

Abstract

Major breakthroughs in biomedical science and clinical practice were accomplished with the development of techniques to image radio-labeled molecule distributions *in vivo*. However, limits in temporal and spatial resolution have hampered these molecular imaging applications to small experimental animals. We present a new rodent SPECT system (U-SPECT-II) enabling radio-molecular imaging of murine organs down to sub-half millimeter resolution as well as high resolution full total body imaging. **Methods:** The high performance of U-SPECT-II is based on a triangular stationary detector setup, an XYZ-stage to translate the animal during scanning and differently sized interchangeable cylindrical collimators for both mouse and rat imaging, each with 75 pinhole apertures. A novel graphical user interface incorporating pre-selection of the field-of-view with the aid of optical images of the animal allows for focusing the pinholes to the structure of interest thereby maximizing sensitivity for the task at hand. Digital inputs enable trigger signals to be incorporated in the acquisition data, which is stored in list mode format. Three-dimensional molecular distributions are iteratively estimated using statistical reconstruction that takes system blurring into account to increase resolution. **Results:** Tc-99m data (energy window of 20 %) are reconstructed using an ordered subset algorithm and the resolution is determined with Jaszczak capillary phantoms. Reconstructed resolutions are < 0.35 mm and 0.45 mm using the mouse collimator with 0.35 mm and 0.6 mm pinholes (PH) respectively. Using the rat collimator with 1.0 mm PH a resolution of < 0.8 mm is obtained. The peak geometric sensitivity is 0.07 % and 0.18 % for the mouse collimator with 0.35 mm and 0.6 mm PH respectively, and 0.09 % for the rat collimator. Resolution with I-125 and In-111 was only barely degraded compared to that of Tc-99m. *In vivo* cardiac, kidney, tumor, and bone images show that U-SPECT-II can be used for novel applications in the study of dynamic biological systems and (radio) pharmaceuticals at the sub-organ level. **Conclusions:** U-SPECT-II allows for discrimination of molecule concentrations between adjacent volumes as small as about 0.04 micro-liters (mice) and 0.5 micro-liters (rats), which is significantly better than existing Positron Emission Tomography (PET) or commercial SPECT systems.

Introduction

Biomedical research strongly benefits from quantitative *in vivo* techniques and the ability to perform longitudinal studies in individual animals. For example, radiolabeling of small molecules, cells, peptides, antibodies, or probes for gene expression [1-16] have made it feasible to investigate molecular mechanisms in living tissue and to evaluate new pharmaceuticals *in vivo*. Employing radio-labeled molecules effectively in rodent models requires Single Photon Emission Computed Tomography (SPECT) and Positron Emission Tomography (PET) instruments that

are dedicated for imaging small animals. For clinical imaging (i.e. in humans) standard SPECT is known to have a relatively poor spatial resolution and improving the spatial resolution of SPECT for animal research is an ongoing challenge. Especially the increasing availability of (genetically modified) mice as models for human disease necessitates the development of instruments with a much better spatial resolution and dynamic capabilities than those until recently available. Several small-animal SPECT instruments have been developed over the last 15 years. For a more beneficial resolution-sensitivity trade-off most dedicated small-animal SPECT systems employ pinhole collimation instead of the clinically used parallel-hole collimation. Introductions to the subject of pinhole SPECT can be found in [17,18] and [19].

In order to be able to enable proper tomographic image reconstruction, projections of the object must be available from a sufficient number of different angles. Most SPECT systems achieve this by rotating either the detector or the object [20-27]. Stationary small animal pinhole SPECT systems [28-32] avoid the need for rotation by using detector set-ups that cover 360 degrees and the use of many pinholes to provide a large number of angles under which the animal is observed. They have fewer moving parts and therefore are less prone to mechanical problems and need for time consuming calibration procedures. They also provide the advantage that one can do dynamic imaging with arbitrarily short frame lengths [12,30,32]. The full 360 degrees coverage in combination with many focusing micro-pinholes and a high magnification factor to maximize the information content per photon provides a reconstructed image resolution that can be significantly better than state-of-the-art small-animal PET (e.g. [19,34]).

The aim of our present work is to describe a dedicated and user friendly ultra-high-resolution multi-pinhole SPECT scanner (U-SPECT-II, figure 1A) suitable for dynamic imaging of small experimental animals such as rats and mice. The system is equipped with unique tools to maximize focusing capabilities and the associated sensitivity when imaging a part of the animal. This and other new features makes that U-SPECT-II is a significant improvement over its experimental prototype (U-SPECT-I [12,31,35]), which was based on a Picker 3000 triple head clinical camera that was converted back and forth from a clinical to a high- resolution pre-clinical system and was only suitable for imaging mouse organs. In the present work we characterize the performance of U-SPECT-II with respect to sensitivity and resolution for different mouse and rat collimators using phantom experiments. Several animal scans demonstrate the wide variety of unique imaging capabilities of U-SPECT-II.

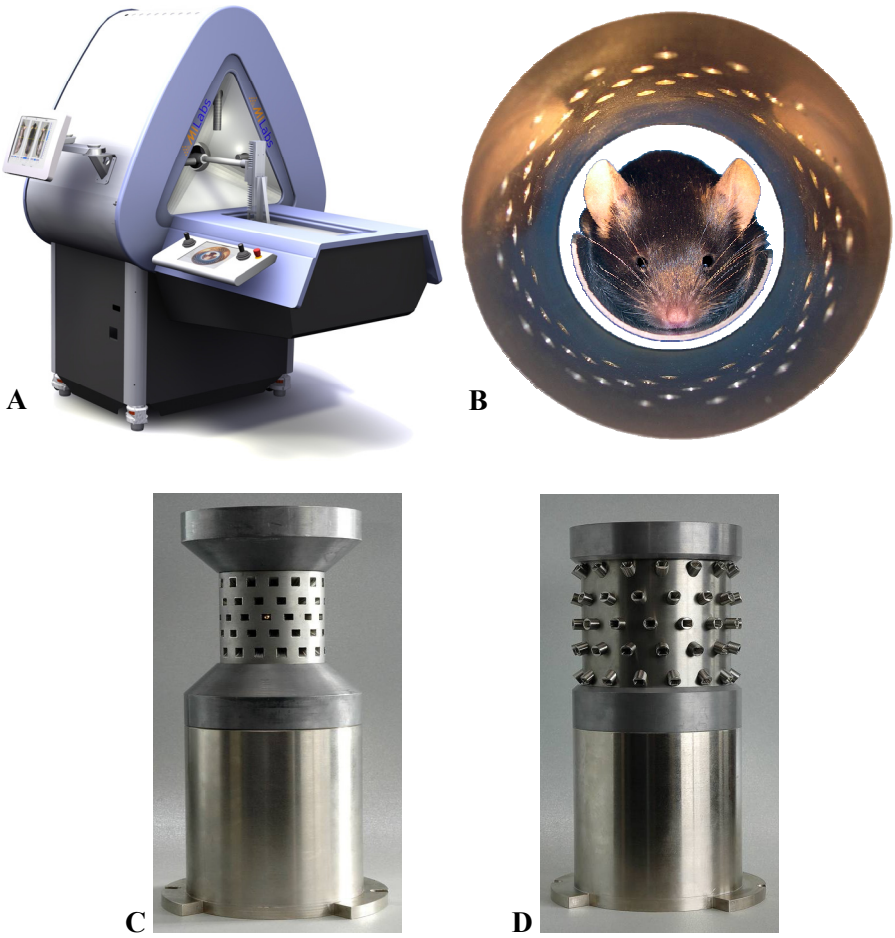

Figure 1: (A) U-SPECT-II system. (B) Collimator tube with mouse. (C) Mouse collimator and shielding tube. (D) Rat collimator and shielding tube. Color figure available in appendix.

Materials and Methods

System description

In U-SPECT-II, different multi-pinhole collimators, together with shielding parts to prevent overlap, are easily exchangeable in order to facilitate optimal imaging for differently sized animals and different scanning times and tracer doses. The sizes of the tubes (44 mm and 98 mm diameter) are optimized for imaging mouse- or rat-sized animals respectively (figure 1C and D). Except for an XYZ stage that moves the bed, the design of the scanner is completely stationary, meaning that there is no need to move the collimator, detectors or the animal, when a specific organ that fits inside

the field-of-view (FOV) is being imaged. If a larger volume of interest (up to total-body imaging) is desired, the animal bed is translated in three dimensions using the stage. For most cases this can be done quickly enough to still enable a combination of multiple-position acquisition with dynamic imaging at a timescale of tens of seconds up to a few minutes. By using large scintillation detectors that are divided up into non-overlapping mini gamma cameras, the design allows to obtain a high resolution and a high sensitivity at the same time (see for example the mathematical analysis of [36]). In our system, each mini-camera focuses on a small FOV through a separate micro-pinhole. List mode acquisition provides flexibility in processing the data afterwards, e.g. for retrospective (multiple) gating, choice of time frame length, and selection of energy windows for single and multi-isotope imaging and scatter correction.

The collimators presented here all consist of a tungsten cylinder with 5 rings of 15 pinhole apertures. The pinhole positions in each ring are rotated with respect to the pinhole positions in adjacent rings in order to increase angular sampling of the object (figure 1B). All pinholes focus on a single volume (i.e. the central FOV) in the center of the tube. As shown in figure 1C the mouse collimator is surrounded with tungsten shielding that prevents the projections on the detector from overlapping. In the rat collimator this shielding is implemented in a different way (figure 1D). The division of the detector in mini-gamma cameras can be visualized by placing a bottle with uniformly distributed activity that is larger than the field-of-view in the collimator tube and acquiring the projection image (figure 2).

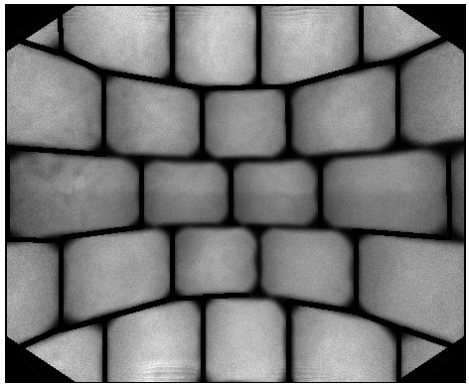

Figure 2: Image from an extended source, showing how one large gamma camera is divided up into many mini gamma cameras. Each segment of the detector corresponds to a projection through a single pinhole.

Using switches the system automatically (i) distinguishes which of the collimators and beds are mounted, and (ii) restricts the motion of the translation stage to prevent collisions. The mounting mechanism of the bed to the robot is made such that the bed is locked in place and can be unlocked and transferred to another scanner, for example to a micro-CT scanner, while keeping the animal in position. This

approach [37,38] combined with a calibration phantom can be used to get registered images from independent imaging modalities without the use of fiducial markers.

Before the animal is moved into the scanner, it is placed between three optical cameras that acquire ordinary visible light images from the two sides and from the top (see figure 3A). In the side and top view, users can select which area (volume) needs to be scanned by moving sliders (see figure 3B). The system's software then calculates the sequence of positions necessary to acquire data from this volume and automatically moves the animal through the focus during the acquisition using this sequence [35]. The selection of the region of interest in the graphical user interface [35,39,40] makes the system as a whole very user-friendly.

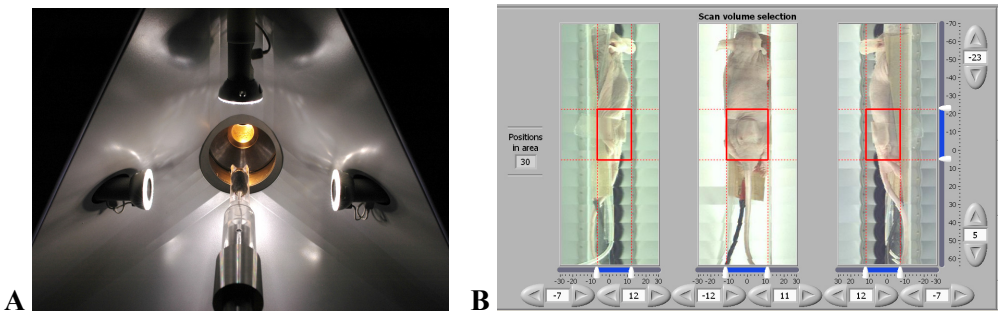

Figure 3: (A) Mouse observed with three optical cameras for region-of-interest selection. (B) User interface allows for selecting the region-of-interest that will be scanned. In this case the region of interest is a tumor of which images are shown in figure 12. Color figure available in appendix.

Image reconstruction is performed with an ordered subset algorithm and a pre-calculated "system matrix" which is created in a calibration procedure that is based on a high number of point source measurements and advanced interpolation techniques [34].

Table 1 lists the features of the U-SPECT-II system, compared to its predecessor, U-SPECT-I. A first notable difference is the much larger surface area of the detectors. The other design parameters are chosen such that the peak sensitivity and resolution are approximately the same in U-SPECT-II as they were in U-SPECT-I, but the field-of-view seen in a single position is significantly larger, effectively increasing the sensitivity in multi-position scans. At the same time, the inner diameter of the mouse collimator has been slightly enlarged to ensure total-body imaging of adult mice can comfortably cover the entire body. The shielding parts (in front of and to the back of the collimator) and the collimators have been made significantly thicker than in U-SPECT-I, which is relevant mostly for imaging higher-energy isotopes and isotopes with high-energy emissions outside the photopeak (e.g. I-123). Important other differences include the availability of list mode data, retrospective dual gating availability, and webcam based navigation of the pinhole focus using a graphical user interface.

	U-SPECT-I	U-SPECT-II
Detectors		
Crystal dimensions L × W × Th (mm)	410 × 250 × 9.5	508 × 381 × 9.5
Number of detectors	3	3
Number of PMTs per detector	49	55
PMT readout method	Analogue, resistor network	Each PMT signal digitized
Data collection	Planar pixel image	List mode data
Pinhole collimator configuration		
Number of rings and pinholes per ring	5 × 15	5 × 15
Mouse single bed position FOV diameter (mm)	10.5	12
Mouse single bed position FOV axial (mm)	5	7
Rat single bed position FOV diameter (mm)	N/A	27
Rat single bed position FOV axial (mm)	N/A	11
Mouse collimator bore diameter (mm)	39	44
Mouse radial position of pinholes (mm)	22	24
Rat collimator bore diameter (mm)	N/A	98
Rat radial position of pinholes (mm)	N/A	53
Mouse pinhole material and diameters (mm)	Au, 0.3, 0.6	Au, 0.35, 0.6
Rat pinhole material and diameters (mm)	N/A	W, 0.7 – 1.5, (Au optional)
Mouse pinhole tube material	W	W
Mouse shielding tube material	Pb	W
Rat collimator tube material	N/A	W
General features		
Mouse collimator 0.6 mm pinholes peak efficiency (%)	0.22	0.18
Mouse collimator 0.35 mm pinholes peak efficiency (%)	0.07	0.07
Rat collimator 1.0 mm pinholes peak efficiency (%)	N/A	0.09
Gating possible	No	Yes, dual
Dead time between measurements (s)	12	2
Dynamic sequence imaging	manual start	automatic
Coordination of scan sequence with acquisition	manual	automatic
GUI based navigator available	No	Yes

Table 1: Comparison of U-SPECT-I to U-SPECT-II features.

The U-SPECT-II detectors

The three scintillation gamma camera heads have sodium iodide (NaI) crystals with a thickness of 3/8 inch (9.5 mm) and a useful detection area of 510 × 381 mm. Each crystal is read out by 55 photomultiplier tubes (PMTs) with the aid of digital read-out electronics. The signal of each individual PMT is digitized, and the electronics in the camera heads, together with the device driver code in the acquisition computer, apply linearity correction, energy correction, and uniformity correction. The detected events are sent to the acquisition computer via a gigabit Ethernet connection and stored in list mode format, containing the horizontal and vertical position (12 bits), energy, and a time stamp for each event.

Performance characterization

Sensitivity

The sensitivity of the system along the axial and trans-axial directions was measured by scanning a Tc-99m point source of known activity through the center of the field-of-view.

Reconstructed spatial resolution

The reconstructed spatial resolution was characterized by using Jaszczak capillary resolution phantoms. For the mouse collimator tubes (pinhole diameters 0.35 and 0.6 mm), the capillary diameters in the six different segments were 0.25, 0.3, 0.35, 0.4, 0.5, and 0.6 mm. The distances between capillaries in a segment equal the capillary diameter within that segment. For the rat collimator, they were 0.7, 0.8, 0.9, 1.0, 1.2 and 1.5 mm. With 600 MBq/ml of Tc-99m, the phantoms were scanned for 2 hours. In order to compare the performance of the system for different isotopes in terms of resolution, the small phantom was filled with 74 MBq/ml of I-125, Tc-99m and In-111 respectively, and subsequently scanned for two hours in the mouse 0.6 mm pinhole collimator.

Scanning Focus Mode

When the animal is step-wise moved through the pinhole focus during acquisition, the reconstruction algorithm needs to combine the data acquired at multiple positions of the animal. We developed a method to take the data from all positions into account simultaneously. This is an improvement over reconstructing each animal position separately and subsequently “stitching together” partial reconstructions [35,41].

Initial animal experiments

Animal studies were conducted following protocols as approved by the Animal Research Committee of the University Medical Center Utrecht and the University of Ghent. To emulate either a proportionally shorter scan time or lower activity without having to scan more animals some of the data sets were reconstructed using the full scan time, and also using 33 % and 10 %, or even 3.3 % and 1 % of the counts from the list mode data. This method saves animals and allows a comparison of images of different acquisition times or doses with the animal in exactly the same position.

Mouse cardiac scan

A 30 g male C57Bl/6 mouse was injected intravenously with 190 MBq of Tc-99m-tetrofosmin and anesthetized using KMA. 45 minutes after injection, the mouse was imaged for 1 hour using the 0.6 mm pinhole mouse collimator. During acquisition an ECG trigger signal was acquired (BioVet, m2m imaging) and incorporated in the list mode data. A gated reconstruction (12 gates) was performed.

Mouse bone scan

A male 28 g C57Bl/6 mouse was injected intravenously with 370 MBq of Tc-99m-hydroxy methylene diphosphonate (HDP). It was anesthetized using ketamine-medetomidine-atropine (KMA) anesthesia. 2.5 hours after radioligand injection, the mouse was imaged for 1.5 hours in the U-SPECT-II system covering the entire body (except for the tail) followed by a scan with the U-CT (MILabs, The Netherlands). The reconstructed SPECT and CT images were co-registered using PMOD software (PMOD Technologies, Zurich, Switzerland).

Rat bone scan

A 279 g male Wistar rat was injected with 1740 MBq of Tc-99m-HDP, and anesthetized with KMA anesthesia. Three hours and twenty minutes after radioligand injection it was imaged for 1 hour in the U-SPECT-II scanner using the 1.0 mm diameter pinhole rat collimator tube.

Mouse kidney scan

A male 30 g C57Bl/6 mouse was anesthetized with isoflurane and injected intravenously with 138 MBq of Tc-99m-dimercapto succinic acid (DMSA). One hour after injection, it was scanned for one hour in the U-SPECT-II using the 0.35 mm pinhole mouse collimator tube. This scan was reconstructed both using all of the data (100 %) and using only 10 % of the counts.

Mouse tumor imaging

A 27 g athymic mouse was inoculated to have a 0.5 g Capan-1 pancreatic tumor in the thigh. After tail-vein injection with 22.2 MBq of ^{111}In-DTPA-14C5 (14C5 is a monoclonal antibody which is over expressed on the (pancreatic) tumor surface). Four days after injection (while the maximal uptake is at 72 hours), the animal was imaged for 30 minutes using the 0.6 mm pinhole mouse collimator. The animal was sacrificed afterwards and the tumor was surgically removed.

Results

Sensitivity measurements

For Tc-99m, the system sensitivity is shown in figure 4 for the mouse collimator with 0.6 and 0.35 mm pinholes and for the rat collimator with 1.0 mm pinholes. The *z*-axis is the axis parallel to the long axis of the collimator cylinder and the *x*- and *y*-axes lie in the radial plane perpendicular to it. For the mouse collimators, the sensitivity is nearly constant within an ellipsoidal shaped area (the central field-of-view) with a diameter of around 12 mm in the *x* and *y* direction and 7 mm in the *z* direction. For the rat collimator, this ellipsoid is approximately twice as large in the *x* and *y* direction and more than twice as large in the *z* direction. The sensitivities in the central field-of-view area for a Tc-99m point source are 1500 cps/MBq (0.18 % geometric) for the mouse collimator with 0.6 mm pinholes, 525 cps/MBq (0.07 %) for the mouse collimator with 0.35 mm pinholes, and around 700 cps/MBq (0.09 %) for the rat collimator with 1.0 mm pinholes.

Figures 5 and 6 show reconstructions of the Jaszczak phantom for an indication of the spatial resolution. Figure 5 shows the maximum achievable resolution for each of the three collimators, using 600 MBq/ml Tc-99m. Figure 6 shows the difference between the isotopes I-125, Tc-99m, and In-111 in the case of the mouse collimator with 0.6 mm pinholes. The concentration for figure 6 was 74 MBq/ml for each isotope and the scan time two hours. The smallest readily discernable rod sizes for the collimators in figure 5 are 0.35, 0.4, and 0.8 mm respectively. At least some of the 0.35 mm rods are still visible with the 0.6 mm pinholes, and some of the 0.3 mm rods are visible with the 0.35 mm pinholes.

From the comparison of the isotopes in figure 6, the rod visibility for In-111 is not appreciably worse than for Tc-99m. For I-125 it is worse, but still well below one mm and approaching 0.5 mm. Since the system was calibrated with a Tc-99m point source [34] without correcting the system matrix for other isotopes, it would be expected that the performance for other isotopes than Tc-99m is not as good. A low photon energy (I-125) would suffer from a poorer detector resolution and more object scatter, and a higher energy (In-111) suffers more from penetration (not corrected for) and collimator scatter (corrected window-based) effects. Considering this disadvantage, the resolution compared to that of Tc-99m is surprisingly good.

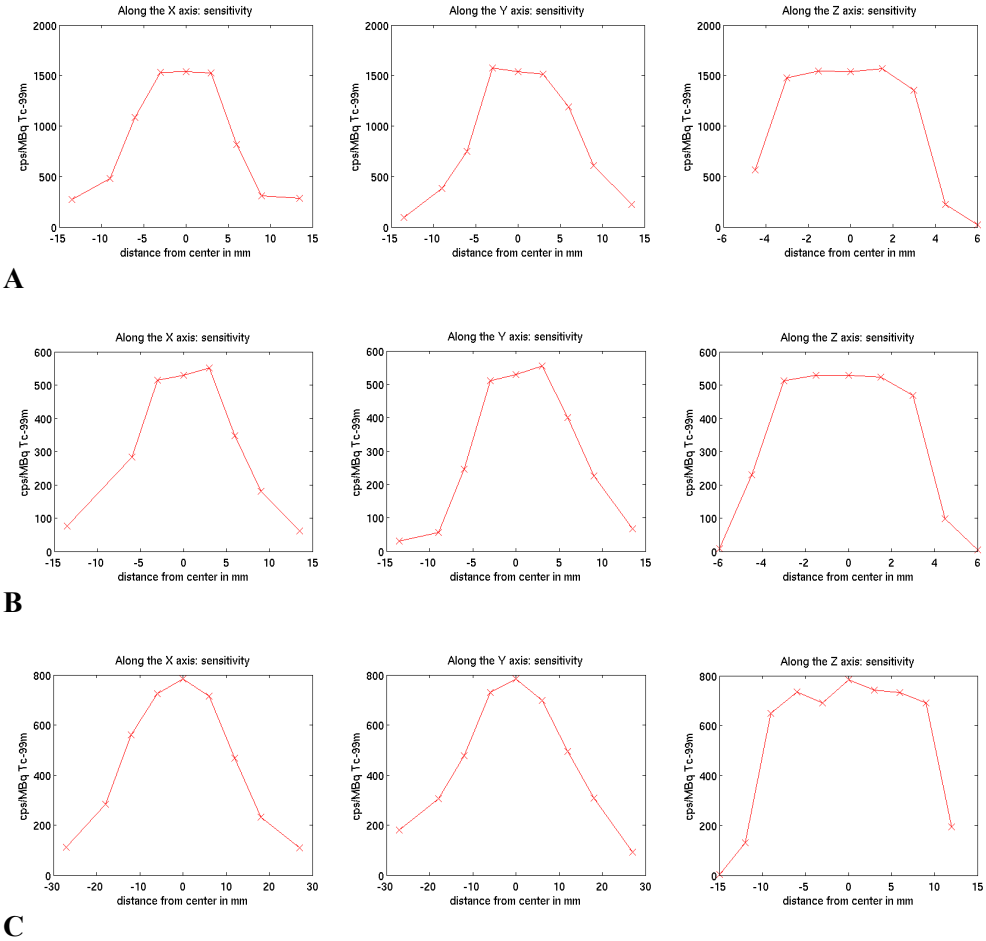

Figure 4: The measured sensitivity for a Tc-99m point source along the *x*-axis (left), the *y*-axis (center) and *z*-axis (right) of the system, expressed in cps/MBq. The *z*-axis is the axis of the cylindrical collimator. Note the different horizontal scale of the plots along the *z*-axis. (A) Sensitivity of the mouse collimator with 0.6 mm pinholes. (B) Sensitivity of the mouse collimator with 0.35 mm pinholes (C) Sensitivity of the rat collimator with 1.0 mm pinholes.

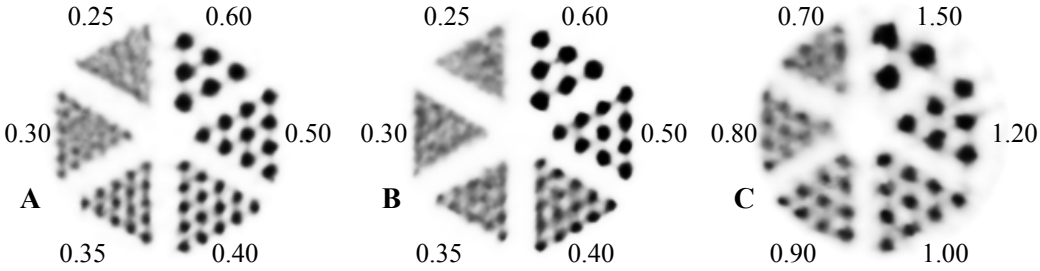

Figure 5: Capillary phantom reconstructions for Tc-99m, 600 MBq/ml, 2 hours scan time. The slice thickness is 3 mm. (A) 0.35 mm pinholes mouse collimator (B) 0.6 mm pinholes mouse collimator (C) 1.0 mm pinholes rat collimator. The smallest discernable rod sizes are 0.35, 0.40 and 0.80 mm respectively.

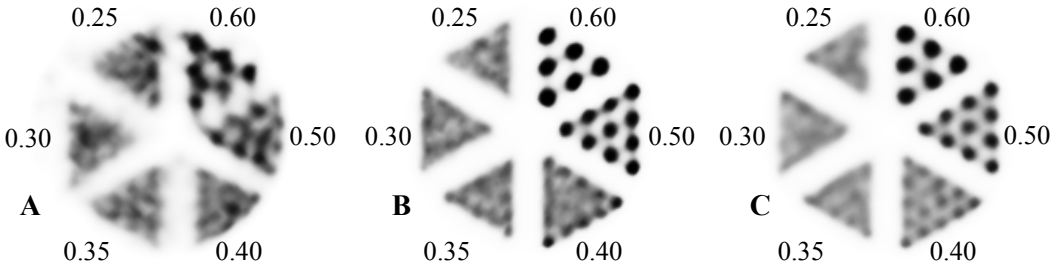

Figure 6: Capillary phantom reconstructions for the 0.6 mm pinhole mouse collimator, obtained with 74 MBq/ml and 2 hours scan time. The slice thickness is 3 mm. (A) I-125 (B) Tc-99m (C) In-111.

Initial animal experiments

Mouse cardiac imaging

Figure 7 shows the end-diastole and end-systole phases of the cardiac cycle in a mouse heart (short-axis view). In both images, the right ventricular wall can be distinguished, as well as the both papillary muscles inside the left ventricle. A movie showing all 16 gates can be found online at http://www.isi.uu.nl/People/Freek.

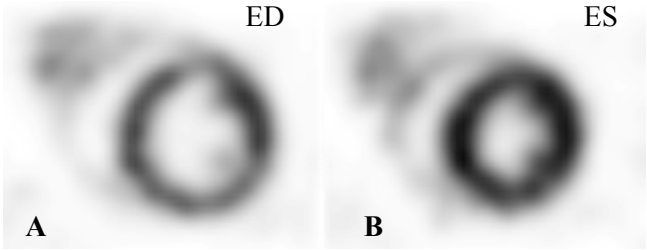

Figure 7: Mouse cardiac gated reconstruction, short axis slices. Frame (A) shows the end diastole and frame (B) the end systole phase of the cardiac cycle.

Mouse bone scan

Figure 8 shows the results of the mouse bone scan, combining SPECT and CT. After registration, the same slice is shown for (A) CT only, (B) SPECT only, and (C) SPECT and CT fused. The data from the SPECT scan were reconstructed using all data, 33% of the data and 10% of the data. Maximum intensity projections (MIPs) from these reconstructed volumes are shown in figure 9. They emulate an injected activity of 370 MBq and scan times of 90 minutes, approximately 30 minutes, and approximately 9 minutes, or alternatively, they emulate a scan time of 90 minutes and injected activities of 370, 123, and 37 MBq respectively. The 3D Gaussian blurring applied to the reconstructed data was increased for lower dose to deal with increasing noise: the FWHMs used were of 0.28, 0.41 and 0.61 mm respectively.

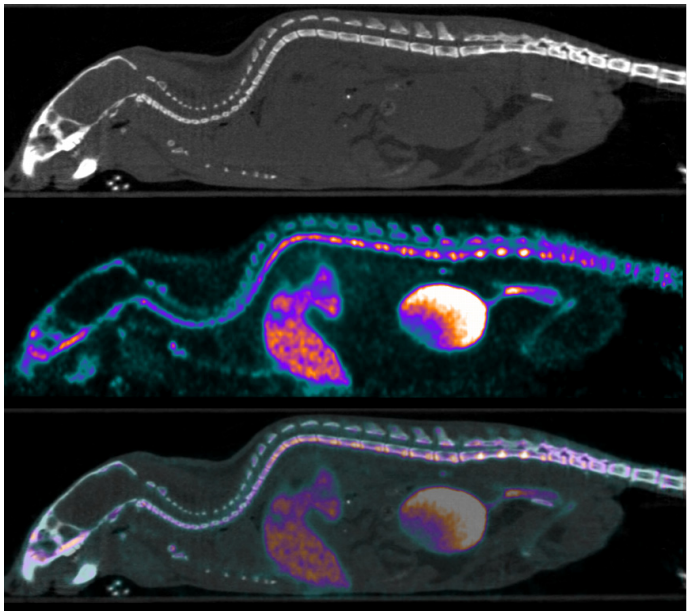

Figure 8: SPECT-CT saggital images of a mouse: (A) CT only (B) SPECT bone scan obtained with ^{99m}Tc-HDP on the U-SPECT-II system (C) fused SPECT/CT image. Registration was done by the method of Chow et al [37]. Color figure available in appendix.

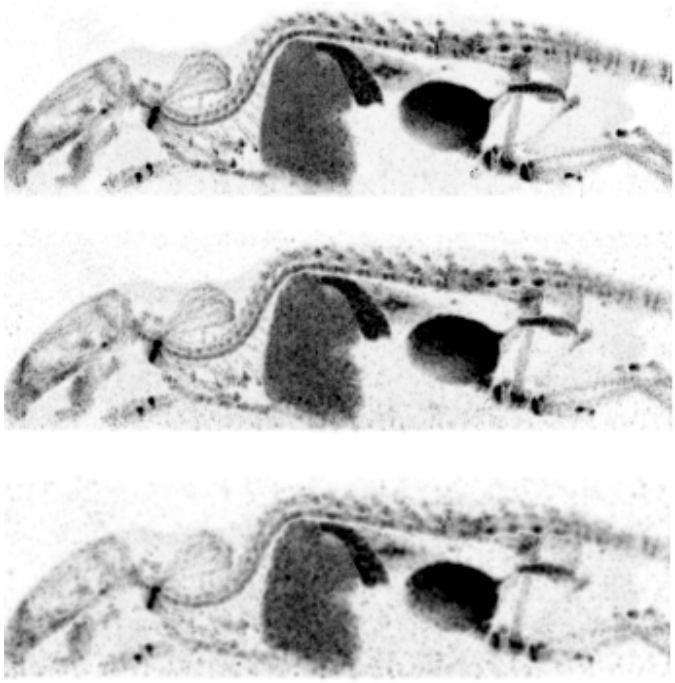

Figure 9: Maximum Intensity Projections of the SPECT data from the mouse bone study of figure 8. Images are based on 100 %, 33 %, and 10 % of the data.

Rat bone scan

Reconstruction of the rat HDP scan was performed using 100%, 33%, 10%, 3.3%, and 1% of the available counts. This emulates an injected activity of 1740 MBq and scan times of approximately 60 minutes, 20 minutes, 6 minutes, 2 minutes, and 36 seconds respectively. Alternatively, they emulate a scan time of one hour and injected activities of approximately 1740 MBq, 580 MBq, 174 MBq, 58 MBq, and 17 MBq. Like in the case of the mouse bone scan, the reconstructions were post-smoothed with an increasing Gaussian kernel size to deal with the noise (kernel FWHMs were 0.30, 0.44, 0.66, 0.99, and 1.43 mm).

Figure 10 shows maximum intensity projections of those five reconstructions. The system sensitivity of the 1.0 mm rat collimator tube lies in between the sensitivities of the 0.6 and 0.35 mm mouse collimators. The size of the tube has been designed to be more than twice as large as the mouse collimator at the cost of resolution. The net result is that relative to the animal's size, approximately the same level of anatomical detail is visible in the mouse (figure 9) as in the rat (figure 10). The acquisition of the rat bone scan was performed with respiratory gating enabled (12 gates). A movie showing the respiratory motion is presented at http://www.isi.uu.nl/People/Freek.

100% = 1740 MBq, 60 minutes

33%, equiv. 1740 MBq, 20 minutes or 580 MBq, 60 minutes

10%, equiv. 1740 MBq, 6 minutes or 174 MBq, 60 minutes

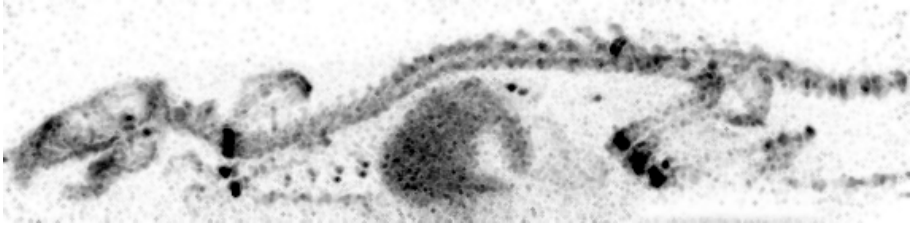

3%, equiv. 1740 MBq, 2 minutes or 58 MBq, 60 minutes

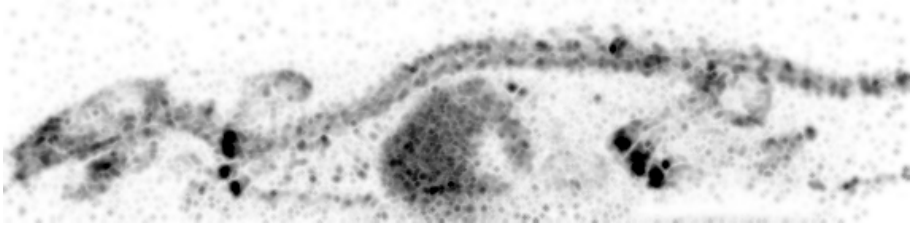

1%, equiv. 1740 MBq, 36 seconds or 17 MBq, 60 minutes

Figure 10: Maximum intensity projection images of a rat Tc-99m-HDP bone scan. The reconstruction used 100% down to 1% of the available counts from the list mode data.

Mouse kidney imaging

Figure 11 shows slices of a Tc-99m DMSA image of the right kidney of the mouse. The slice thickness is only 0.375 mm. The uptake in the kidney's cortex demonstrates the sub-mm resolution of the instrument in this *in vivo* image. Figure 11B shows the same study as frame a, but was reconstructed using only 10% of the recorded photons. This emulates a scan time of 1 hour and with an injected activity of 13.8 MBq, or alternatively, a scan time of 6 minutes with an injected activity of 138 MBq. DMSA is retained for a long time in the cortex of the kidney, especially in the tubules. The images show the distribution of functioning kidney tissue. Such scans can be used to localize defects in the parenchyma or to assess the relative contribution of each kidney, for example, the function of the left versus the right kidney. The resolution in the presented images is sufficient to access function of tiny parts of mouse kidneys.

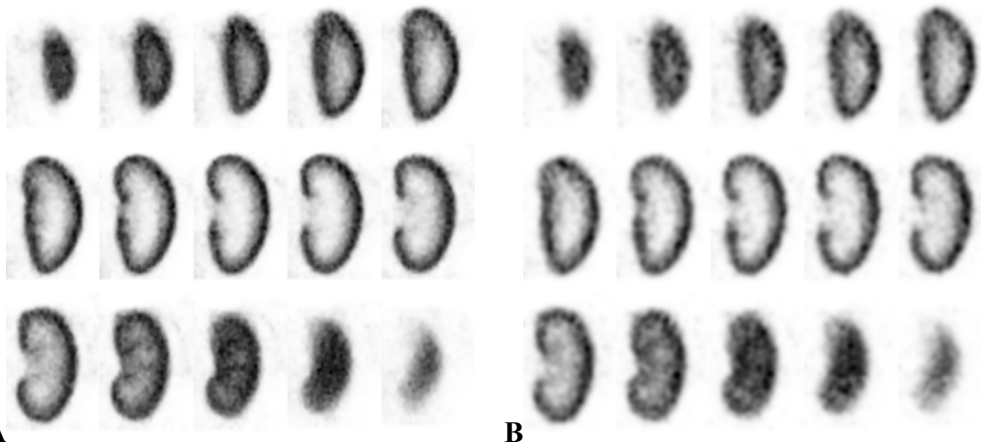

A 100%, 138 MBq, 60 min

B 10% of the counts (Equivalent to 138 MBq, 6 min or 14 MBq, 60 min)

Figure 11: A Tc-99m-DMSA scan of a mouse kidney (0.375 mm slices). Reconstruction was performed using 100% (A) and 10% (B) of the acquired counts. This image shows distribution of functioning kidney tissue. Such scans can be used to localize defects in the parenchyma, to assess the relative contribution of sub-compartments of a kidney.

Mouse In-111 tumor imaging

Figures 12B to 12D show that U-SPECT-II delivers a very good resolution for this medium-energy isotope. Moreover, the tumor can be imaged in 2-4 bed positions, enabled through the aforementioned dynamic list mode and the step-and shoot acquisition with the XYZ stage. The good agreement with anatomic data is presented in the perpendicular slices through the SPECT image volume (figure 12).

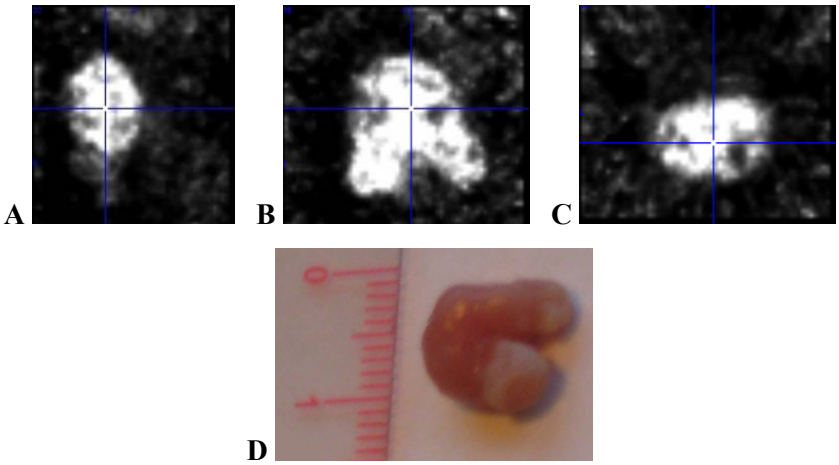

Figure 12: In-111-DTPA-14C5 mouse study (A), (B), and (C) three views of the reconstructed data. (D) photograph of the tumor. Color figure available in appendix.

Discussion

We built a versatile SPECT system with an advanced user interface that can be used for performing molecular imaging in both mice and rats. Its resolution is unmatched by any existing commercial SPECT or PET system. With the focusing design currently applied in the U-SPECT-II, it is possible to perform focused imaging, only studying a single organ of interest at extremely high sensitivity and resolution, as well as imaging larger volumes up to total-body imaging, with a single collimator tube. We expect that it is possible to improve significantly on the performance in specific cases with collimator tubes dedicated to specific tasks. For example, a dedicated collimator for extremities could have a much smaller diameter and the same amount of pinholes. The resulting increase of sensitivity and magnification factor may improve the resolution to about 0.1 mm for legs and possibly to 0.25 mm for the mouse brain. Another example is a dedicated brain collimator for rats [42]. However the first improvements may be possible by selecting the right pinhole diameter for a specific study type.

The reconstructed image quality for short scan times and low-dose studies was estimated by using only a part of the available counts from list-mode data. This approach has the advantage that there are no experimental differences such as inter-animal variability that influence the comparison, since the data being used is from the same acquisition. An inaccuracy for emulating the case of a low dose is that the scaling of the available counts like it was done here does not keep the background count rate (from e.g. cosmic radiation) constant, but instead reduces it along with the counts from the object. This may make the simulated low-count image look slightly more favorable than a real acquisition with a lower injected activity would have been.

For U-SPECT-II, the typical background count rate in the Tc-99m window is 50 cps for each of the three gamma cameras and a medium-to-high count animal acquisition produces 10000 cps in that window. If that is reduced to 10% (i.e. 1000 cps) we would be neglecting a background count rate of 5% of the total counts.

The algorithm that calculates the scan sequence from the boundaries drawn by the user is currently fairly straight forward [35]. There is ongoing research to optimize the scan sequence by means of experiments and advanced simulation studies. This may lead to further improvements in image quality.

Today, the advantages and disadvantages of using overlapping versus non-overlapping projections is actively being researched at several labs worldwide. Overlap increases system sensitivity but one has too keep in mind that this increase is at least partly artificial, since a significant amount of information per photon can be lost due to the overlap. Therefore, sensitivity of systems based on overlapping projections can not be compared to systems with non-overlapping projections. Moreover, overlap can lead to increasing reconstruction time due to slow convergence of iterative algorithms for these cases, and completely misplace the activity in the reconstruction when activity is present outside the area that is sufficiently sampled [43].

Projected future versions of U-SPECT may be based on detectors with a higher intrinsic resolution [19]. Higher resolution detectors suitable for gamma imaging are being developed (e.g., [44,45]). Detectors with a very high intrinsic resolution are currently still too much in a prototype stage or too expensive, for full ring devices despite the fact that a much smaller detector ring can be used with such detector resolutions [36,46].

Conclusion

The introduction of U-SPECT-II defines a new front line in ultra-high resolution small-animal radio-molecular imaging. It is flexible and user friendly with regard to selection of optimal collimators and field-of-view for different animals and imaging tasks. An outstanding volumetric resolution of 0.04 µl has been obtained with the highest resolution collimators tested in here for Tc-99m. In addition we showed that excellent images can be obtained with tracers such as I-125 and In-111. Results show that U-SPECT-II provides a significant resolution improvement over current state-of-the-art small-animal SPECT and PET systems. As a result, the system allows for assessing tracer dynamics in sub-compartments of organs, as was illustrated by initial *in vivo* images with sub-mm details of tracer uptake in rodent brains, heart and bone.

The high resolution and high sensitivity together with exchangeable collimator tubes, animal beds and a user-friendly web-cam based interface should now allow detailed molecular imaging to be applied successfully to a wide range of study types, thus creating a broad range of new experimental opportunities. Significant improvements in the image quality of U-SPECT-II can be expected when collimation parameters are optimized for specific tasks. It is expected that high-resolution gamma

detectors and collimators tailored to specific application (bone, brain, tumors) will play an important role in the future improvement of such small animal SPECT instruments.

Acknowledgements

This work was sponsored by the Netherlands Organization for Scientific Research (NWO), grant 917.36.335. We thank Norbert Gehéniau, Bert Westra, Henk te Biesebeek and Kees Ligtvoet for instrumental support, the staff at Inter Medical Medizintechnik and Gijs van der Wilt for technical assistance, Carmen van Vilsteren, Paul Hermans for fruitful discussions, Mart Rentmeester for registration of the SPECT and CT images, and Jan Heemskerk for proof-reading the manuscript.

References

[1] Gambhir SS, Herschman HR, Cherry SR, et al., 'Imaging transgene expression with radionuclide imaging technologies', *Nature Neoplasia* 2000; 2(1): 118–138.

[2] Phelps ME, 'Inaugural article: positron emission tomography provides molecular imaging of biological processes', *Proc. Natl. Acad. Sci. USA.* 2000; 97: 6226–6233.

[3] Herschman HR, MacLaren DC, Iyer M, Namavari M, Bobinski K, Green LA, Wu L, Berk AJ, Toyokuni T, Barrio JR, Cherry SR, Phelps ME, Sandgren EP, Gambhir SS, 'Seeing is believing: Non-invasive, quantitative and repetitive imaging of reporter gene expression in living animals, using positron emission tomography', *J. Neuroscience research.* 2000; 59(6): 699-705.

[4] Jacobs A, Voges J, Reszka R, Lercher M, Gossmann A, Kracht L, Kaestle C, Wagner R, Wienhard K, Heiss W, 'Positron-emission tomography of vector-mediated gene expression in gene therapy for gliomas', *The Lancet.* 2001; 358(9283): 727-729.

[5] Weissleder R, 'Scaling down imaging: molecular mapping of cancer in mice', *Nature Rev. Cancer.* 2002; 2(1): 11–18.

[6] Blasberg R, 'PET imaging of gene expression', *Eur. J. Canc.* 2002; 38: 2137-2146.

[7] Rudin M, Weissleder R, 'Molecular imaging in drug discovery and development', *Nature Rev. Drug Discov.* 2003; 2(2): 123–131.

[8] Shah K, Jacobs A, Breakefield XO, Weissleder R, 'Molecular imaging of gene therapy for cancer', *Gene Ther.* 2004; 11(15): 1175–1187.

[9] Rueger MA, Kracht LW, Hilker R, Thiel A, Sobesky J, Winkeler A, Thomas AV, Heneka MT, Graf R, Herholz K, Heiss WD, and Jacobs AH, 'Role of in vivo imaging of the central nervous system for developing novel drugs', *J. Nucl. Med. Mol. Im.* 2007; 51: 164-181.

[10] Tran N, Franken PR, Maskali F, Nloga J, Maureira P, Poussier S, Groubatch F, Vanhove C, Villemot JP, and Marie PY, 'Intramyocardial Implantation of Bone Marrow–Derived Stem Cells Enhances Perfusion in Chronic Myocardial Infarction: Dependency on Initial Perfusion Depth and Follow-up Assessed by Gated Pinhole SPECT', *J. Nucl. Med.* 2007; 48(3): 405-412.

[11] Vemulapalli S, Metzler SD, Akabani G, Petry NA, Niehaus NJ, Liu X, Patil NH, Greer KL, Jaszczak RJ, Coleman RE, Dong C, Goldschmidt-Clermont PJ, and Chin BB, 'Cell Therapy in Murine Atherosclerosis: In Vivo Imaging with High-Resolution Helical SPECT', *Radiology*. 2007; 242: 198-207.

[12] Vastenhouw B, van der Have F, van der Linden AJA, von Oerthel L, Booij J, Burbach JPH, Smidt MP, and Beekman FJ. 'Movies of dopamine transporter occupancy with ultra-high resolution focusing pinhole SPECT', *Mol. Psych.* 2007; 12: 984-987.

[13] Wu L\

[14] Jongen C, de Bruin K, Beekman FJ, and Booij J, 'SPECT imaging of D2 dopamine receptors and endogenous dopamine release in mice', *Eur. J. Nucl. Med. Mol. Im.* 2008; 35(9): 1692-1698.

[15] Gainkam LO, Huang L, Caveliers V, Keyaerts M, Hernot S, Vaneycken I, Vanhove C, Revets H, De Baetselier P, and Lahoutte T, 'Comparison of the biodistribution and tumor targeting of two Tc-99m-labeled anti-EGFR nanobodies in mice, using pinhole SPECT/micro-CT', *J. Nucl. Med.* 2008; 49(5): 788-795.

[16] Huang L, Gainkam LO, Caveliers V, Vanhove C, Keyaerts M, De Baetselier P, Bossuyt A, Revets H, Lahoutte T, 'SPECT imaging with Tc-99m-labeled EGFR-specific nanobody for in vivo monitoring of EGFR expression', *Mol. Imaging Biol.* 2008; 10(3): 167-175.

[17] King MA, Pretorius PH, Farncombe T, Beekman FJ, 'Introduction to the physics of molecular imaging with radioactive tracers in small animals (review)', *J. Cell. Biochem.* 2002; 39: 221–30.

[18] Meikle SR, Kench P, Kassiou M, Banati RB, 'Small animal SPECT and its place in the matrix of molecular imaging technologies', *Phys. Med. Biol.* 2005; 50(22): R45-61.

[19] Beekman FJ and van der Have F, 'The pinhole: gateway to ultra-high resolution three-dimensional radionuclide imaging', *Eur. J. Nucl. Med. Mol. Im.* 2007; 34: 151-161.

[20] Jaszczak RJ, Li J, Wang H, Zalutsky MR, Coleman RE, 'Pinhole collimation for ultra-high-resolution small-field-of-view SPECT', *Phys. Med. Biol.* 1994; 39: 425–37.

[21] Ishizu K, Mukai T, Yonekura Y, et al., 'Ultra-high-resolution SPECT system using four pinhole collimators for small animal studies', *J. Nucl. Med.* 1995; 26: 2282–2289.

[22] McElroy DP, MacDonald LR, Beekman FJ, et al., 'Performance evaluation of A-SPECT: A high resolution desktop pinhole SPECT system for imaging small animals', *IEEE Trans. Nucl. Sci.* 2002; 49: 2139–2147.

[23] Schramm NU, Ebel G, Engeland U, Schurrat T, Béhé M, Behr TM, 'High-Resolution SPECT using Multipinhole Collimation', *IEEE Trans. Nucl. Sci.* 2003; 50(3): 315-320.

[24] Walrand S, Jamar F, de Jong M, Pauwels S, 'Evaluation of novel whole-body high-resolution rodent SPECT (Linoview) based on direct acquisition of linogram projections', *J. Nucl. Med.* 2005; 46(11): 1872-80.

[25] Metzler SD, Jaszczak RJ, Patil NH, Vemulapalli S, Akabani G, and Chin BB, 'Molecular imaging of small animals with a triple-head SPECT system using pinhole collimation', *IEEE Trans. Med. Im.* 2005; 24(7): 853-862.

[26] Moore SC, Zimmerman RE, Mahmood A, Mellen R, Lim CB, 'A triple-detector multi-pinhole system for SPECT imaging of rodents', *J. Nucl. Med.* 2005; 45(5): 97P.

[27] Hesterman JY, Kupinski MA, Furenlid LR, Wilson DW, and Barrett HH, 'The multi-module, multi-resolution system (M^3R): A novel small-animal SPECT system', *Med. Phys.* 2007; 34(3): 987-993.

[28] Kastis GK, Barber HB, Barrett HH, Gifford HC, Pang IW, Patton DD, et al., 'High resolution SPECT imager for three-dimensional imaging of small animals (abstract)', *J. Nucl. Med.* 1998; 39(5): 25 Suppl S 9P.

[29] Liu Z, Kastis GA, Stevenson GD, Barrett HH, Furenlid LR, Kupinski MA, et al., 'Quantitative analysis of acute myocardial infarct in rat hearts with ischemia-reperfusion using a high-resolution stationary SPECT system', *J. Nucl. Med.* 2002; 43(7): 933–939.

[30] Furenlid LR, Wilson DW, Chen Y, Kim H, Pietrski PJ, Crawford MJ, et al., 'FastSPECT II: a second-generation high-resolution dynamic SPECT imager', *IEEE Trans. Nucl. Sci.* 2004; 51: 631-5.

[31] Beekman FJ, van der Have F, Vastenhouw B, van der Linden AJA, van Rijk PP, Burbach JPH, Smidt MP, 'U-SPECT-I: A novel system for sub-millimeter resolution tomography of radiolabeled molecules in mice', *J. Nucl. Med.* 2005; 46: 1194-1200.

[32] Funk T, Després P, Barber WC, Shah KS, Hasegawa BH, 'A multi-pinhole small animal SPECT system with submillimeter spatial resolution', *Med. Phys.* 2006; 33(5): 1259-67.

[33] Kupinski MA and Barrett HH, 'Small-Animal SPECT imaging', New York: *Springer Science+Business Media Inc.* 2005.

[34] van der Have F, Vastenhouw B, Rentmeester MCM, Beekman FJ, 'System Calibration and Statistical Image Reconstruction for Ultra-High Resolution Stationary Pinhole SPECT', *IEEE Trans. Med. Im.* 2008; 2008; 27(7): 960-971.

[35] Vastenhouw B and Beekman FJ, 'Submillimeter Total-Body Murine Imaging with U-SPECT-I', *J. Nucl. Med.* 2007; 48: 487-493.

[36] Rentmeester MCM, van der Have F, and Beekman FJ, 'Otimizing multi-pinhole SPECT geometries using an analytical model', *Phys. Med. Biol.* 2007; 52: 2567-2581.

[37] Chow PL, Stout DB, Komisopoulou E, and Chatziioannou AF, 'A method of image registration for small animal, multi-modality imaging', *Phys. Med. Biol.* 2006; 51: 379-390.

[38] Beekman FJ and Hutton BF, 'Multi-modality imaging on track', *Eur. J. Nucl. Med. Mol. Im.* 2007; 34(9): 1410-1414.

[39] Beekman FJ, 'Stralings detectie inrichting', *Dutch patent application, NL-1030168.* October, 2005

[40] Beekman FJ, 'Radiation detection device, scintillation device and detection method, as well as multiple image-forming device', *PCT application PCT/NL2006/000513*, October 2006.

[41] Beekman FJ, Vastenhouw B, van der Have F. 'Towards 3D nuclear microscopy using locally focusing many-pinhole SPECT', *Proceedings of the 2003 International Meeting on Fully Three-Dimensional Image Reconstruction in Radiology and Nuclear Medicine*, Saint-Malo, France, 2004.

[42] Beekman FJ, van der Have F, and Vastenhouw B, 'Sub-half mm rat brain SPECT with a dedicated ultra-high resolution focusing pinhole collimator', *J. Nucl. Med.* 2008; 49(Suppl 1): 401P-402P.

[43] Vunckx K, Suetens P, and Nuyts J, 'Effect of Overlapping Projections on Reconstruction Image Quality in Multipinhole SPECT', *IEEE Trans. Med. Imaging.* 2008; 27(7): 972-983.

[44] de Vree GA, Westra AH, Moody I, van der Have F, Ligtvoet CM, and Beekman FJ, 'Photon-counting Gamma Camera based on an Electron-Multiplying CCD', *IEEE Trans. Nucl. Sci.* 2005; 52: 580-588.

[45] Meng LJ, Clinthorne NH, Skinner S, Hay RV, and Gross M, 'Design and feasibility study of a single photon emission microscope system for small animal I-125 imaging', *IEEE Trans. Nucl. Sci.* 2006; 53: 1168-1178.

[46] Beekman FJ and Vastenhouw B, 'Design and simulation of a high-resolution stationary SPECT system for small animals', *Phys. Med. Biol.* 2004; 49: 4579–4592.

Chapter 6

Field-of-view definition for focusing pinhole SPECT using optical cameras

Brendan Vastenhouw, Woutjan Branderhorst, Frans van der Have, Martin Baiker and Freek J. Beekman

Abstract

Focusing pinhole SPECT is capable of reaching high resolutions and high sensitivity. To optimize the definition of the volume-of-interest (VOI) to be scanned we propose a new tool that is based on a combination of dedicated hardware (optical cameras) and software. The SPECT-II system used in the present work is equipped with a cylindrical collimator containing 75 pinholes, which are all focused to a small field-of-view (FOV) to obtain a high count yield. To perform extended FOV imaging the animal bed steps through the collimator using an XYZ-stage. Prior to SPECT imaging, the bed is positioned in front of the collimator while three webcams acquire optical images of the animal from the left, right and top. Using a graphical user interface the boundaries of the volume to be scanned can be marked by rectangles in all directions in order to define a box. Next, a sequence of bed translations is calculated such that the focus of the pinholes scans only within this box. The ability to select the scan volume in all directions makes it possible to maximize the number of counts from an organ of interest which results in better resolution and lower noise. Images from resolution phantom scans as well as a mouse heart study show that this focused approach significantly improves image quality. Moreover, a sensitivity increase of approximately 250 % was obtained by using a highly-focused scan volume in all directions instead of a non-focused scan volume. Accuracy measurements show that it is possible to calibrate the correspondence between the optical images and the reconstructed image with an accuracy below 0.5 mm. We conclude that the combination of focused scanning with optical guided VOI selection enables easy and accurate selection of the VOI, and high resolution imaging which is vital to use the full potential of highly focusing systems.

Introduction

Several stationary and non-stationary pinhole SPECT scanners have been designed and constructed in recent years [1-21]. Recently, sub-half millimeter resolutions have been reached, using conventional detectors [6,22]. Key to obtaining these ultra-high resolutions is the application of pinhole collimation instead of parallel-hole or fan beam collimators. Pinholes allow magnification of the field-of-view (FOV) onto the detector. Magnification suppresses the effect of image degradation by detector blurring and therefore removes the intrinsic resolution of the detector as a hurdle to reach a better system resolution. To further improve multi-pinhole systems, all pinholes can be focused on a small area to get much more counts from a specific location. In this way, detailed images of mouse organs (e.g. beating heart, kidney and brain structures like the striatum) and molecular concentrations on a scale of about an order of magnitude smaller than the 3 mm intrinsic resolution of the detector, have been acquired [1,6,22,24]. With these highly focused systems it is

possible to scan a volume-of-interest (VOI) up to total body for mice and rats. This is accomplished by translating the animal through the focus of the scanner and using specially adapted reconstruction methods [23] where the images are reconstructed using all projections over all bed positions simultaneously.

To fully utilize the high peak sensitivity of focusing pinhole SPECT, the positioning of the focus to the VOI is important: the better one focuses the more counts can be obtained from the organ of interest. It is possible to position the focus using only a persistence scope, but this approach is time consuming for pinhole SPECT and is only possible when the tracer is already at the target location. The goal of the present chapter is to increase the performance of a focusing SPECT system based on a novel solution to quickly and accurately position the animal such that the focus accurately samples the selected VOI. Images obtained with different levels of focus will be presented, showing that accurate focusing leads to significant improvement of image quality.

Materials and Methods

System design

The U-SPECT-II is a multi-pinhole SPECT scanner for imaging rodents, consisting of a static detector set-up with exchangeable collimators for differently sized animals [6]. Each collimator consists of a tungsten cylinder containing 75 micro-pinhole apertures which all focus to a small FOV in the center of the collimator. This approach maximizes the detection yield of gamma-photons. For a mouse collimator, the FOV is approximately 7 mm in length and has a diameter of 12 mm. To scan a region larger than the FOV, the animal is moved stepwise through the focus [23]. The animal is placed on a thin, half-cylindrical transparent bed (polymethylmethacrylate) which contains a heater pad to keep the temperature of the animal stable during the acquisition. The bed is mounted on a motor-controlled XYZ stage, which allows accurate positioning of the animal (figure 1).

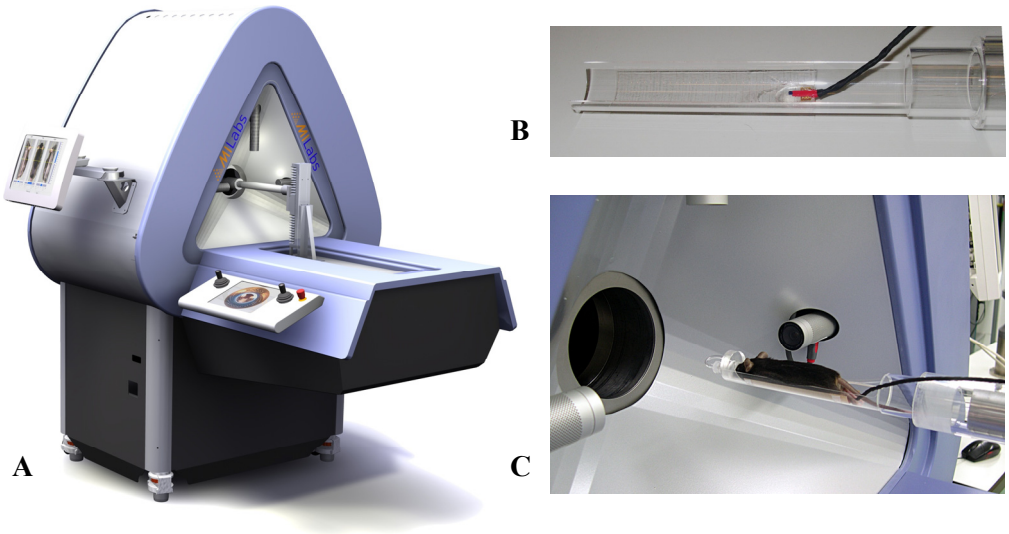

Figure 1: (A) The U-SPECT-II system showing the optical cameras at the front of the scanner, the XYZ stage and the control panels. (B) Animal bed with transparent heater pad. (C) Close-up of a mouse on the bed in front of the optical cameras. Color figure available in appendix.

Webcam based positioning

Prior to the SPECT scan, three optical cameras acquire images of the animal from the top, left and right. The optical cameras are mounted in front of the collimator and the correspondence between points projected on the optical images and points inside the collimator is accurately determined via calibration. A graphical user interface displays the three views of the animal, on which the user marks the boundaries of the VOI to be scanned (figure 2A). The boundaries are determined by a box which is projected on top of the animal images and can be adjusted in each direction using sliders alongside the images. The software calculates a sequence of bed positions such that the focus of the pinholes samples only the area within the box. Each location within the box will be inside the focus of the pinholes for at least one of the bed positions. Depending on the size of the selection, the number of positions needed can range from one single position for organs like the heart, brain or a tumor up to several tens of positions for total-body scanning. During SPECT acquisition, the animal is automatically moved stepwise through the collimator according to the calculated sequence and photons are collected from the entire box-shaped VOI.

Additional persistence scope

Optionally, the user can utilize the persistence scope functionality during the definition of the scan volume, which allows for fine-positioning the bed when the tracer is already injected. The user can preview how the gamma photons from the center of the selected VOI are projected through the central pinholes onto the gamma

cameras (figure 2B). These projections correspond to the left, right and top views from the optical cameras (figure 2D). When the images from the persistence scope indicate that the location of the selected VOI is not positioned optimally one can shift the selected volume. Afterwards, the bed is moved to the new position and the user can check the persistence scope again, similar to a clinical SPECT system.

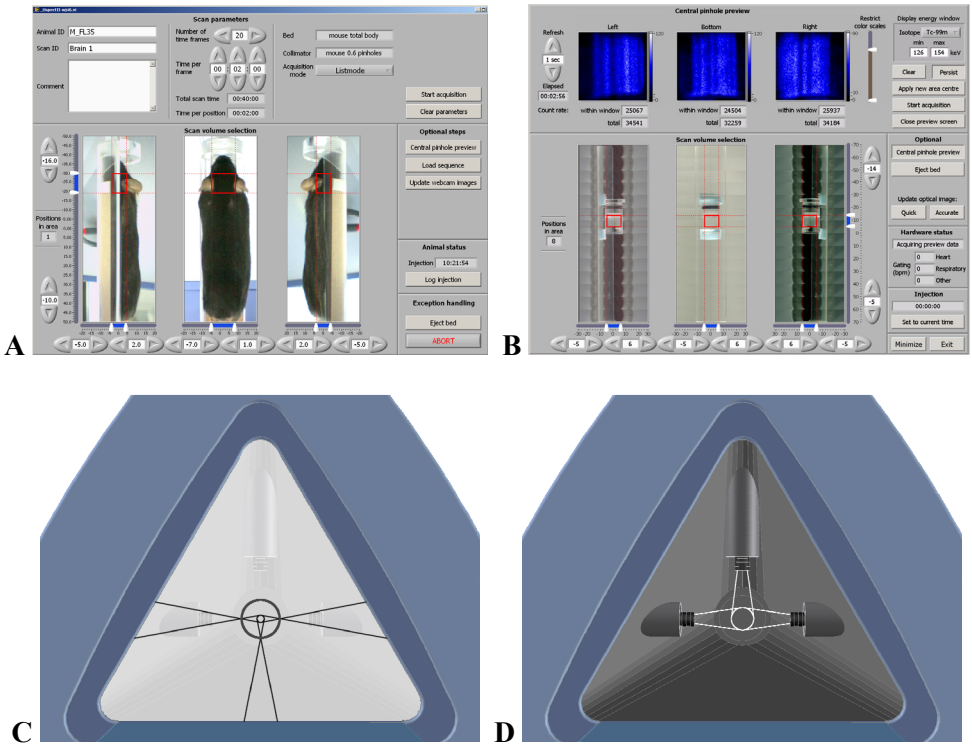

Figure 2: (A) Graphical user interface showing the webcam images of a mouse. The VOI selection is marked by red lines on top of each image. (B) The persistence scope screen displaying the webcam images of a small resolution phantom on the bottom of the screen and corresponding pinhole projections on the top of the screen, where individual rods can be readily distinguished. The projected gamma photons from 3 of the central pinholes of the gamma cameras (C) correspond to the left, right and top view of the optical images (D). Note that the inverted image from the bottom projection corresponds to the optical image from the top webcam. Color figure available in appendix.

Calibration of the webcams

The optical cameras are mounted on the system perpendicular to the longitudinal axis of the collimator tube with the focus directed to the centerline of the cylindrical collimator (figure 3). Small mechanical adjustments in angle and rotation are possible for each individual camera to obtain accurate assembly. To ensure that the images from the webcams are properly aligned, scaled and all pointing to the same reference point in 3D, a calibration procedure is performed. A special 'calibration block' is attached to the XYZ stage and positioned in front of the optical cameras. The block is made of white plastic, is 30 × 30 × 60 mm in size and has a grid of black lines 5 mm apart. For each camera, we obtain an image of this calibration block and rotate the image so that it aligns with the grid of the calibration block. Since the location and the dimensions of the grid are known, we can now calculate the parameters needed to scale, translate and resample the images from the optical cameras to match the grid of the 'calibration block'. Using this procedure, we automatically adjust for differences between the individual cameras and correct for optical distortion.

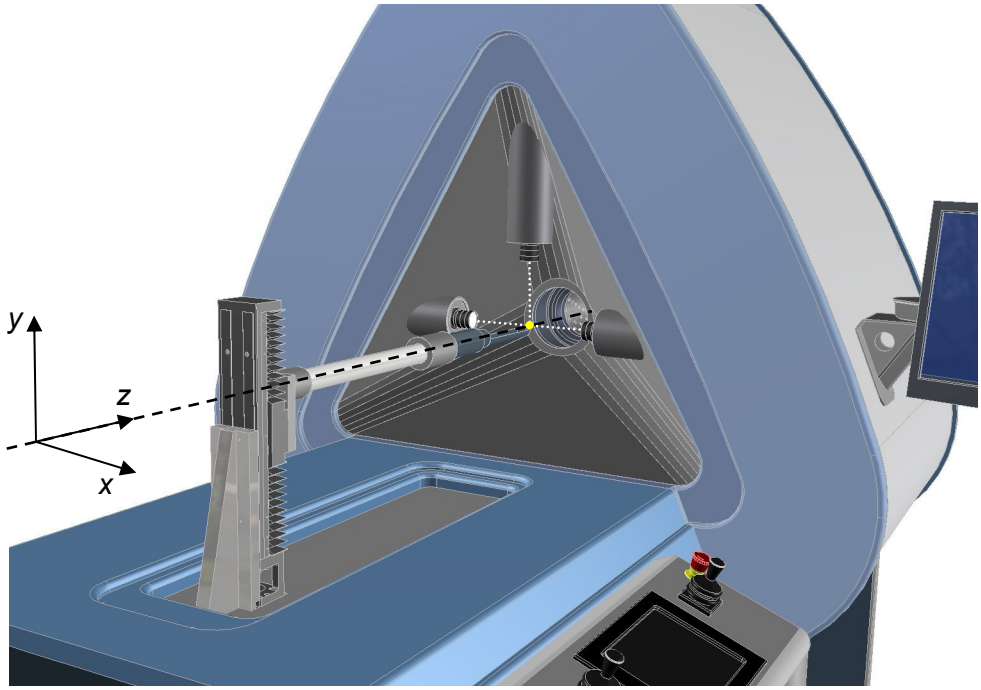

Figure 3: XYZ stage mounted in front of the collimator tube. The webcams are located in front of the collimator tube and the cameras focus to one point on the centerline of the collimator. Color figure available in appendix.

Calibration of the XYZ system

The XYZ stage is attached to the system with the *z*-axis parallel to the longitudinal axis of the collimator tube and the *x* and *y*-axis perpendicular to it (figure 3). Dial indicators are used to accurately measure the alignment between the collimator and the XYZ stage during assembly of the system. The center of the collimator cylinder is determined by mounting on the XYZ stage a thin cylindrical rod, which ends in a fine needle point. A Perspex cylinder with a small hole exactly in the center is inserted into the collimator. Afterwards, the XYZ stage is positioned in such a way that the needle points exactly through the hole of the Perspex cylinder and the *x* and *y* coordinates are stored as the center of the collimator cylinder.

To determine the distance between the center of the webcam images and the center of the collimator tube along the *z*-axis, a small point source (a resin bead, approx. 0.2 mm diameter dipped in Tc-99m) is glued to a fine point which is attached to the XYZ stage. This point source is slowly moved along the centerline of the collimator tube and the projection data from the gamma cameras is analyzed. When the point source is exactly in the center of the collimator, a small circle is present in the center of each pinhole projection image.

Each stage of the XYZ system is driven by a servo motor with integrated controller which is connected to the computer by a RS-232 interface. It is possible to read the current position of the stage using the same interface. When the power to the motors has been interrupted, the stages are homed once before use by slowly moving to a hardware reference point at the beginning of the stage. The minimal step size of each stage is 0.005 mm. By using a high precision measurement tool, the repeatability of the stages was determined to be ≤ 0.02 mm for each of the individual axes.

Image reconstruction

Image reconstruction was performed using an Ordered-Subset Expectation-Maximization algorithm which is specially adapted for the scanning focus design of the U-SPECT-II system [6,23]. All images were reconstructed with 6 iterations using 16 subsets, and afterwards a Gaussian post-filter was applied.

Accuracy measurements

For the webcam based selection it is important that the alignment of the optical cameras to the collimator is accurately known. Therefore, the accuracy of the optical selection method is tested using a cubic plastic phantom which contains 5 point sources in small holes at known locations. Ion exchange resin beads with a diameter of approximately 0.2 mm are dipped in Tc-99m and used as point sources. The cube is machined with high accuracy and the dimensions are $12 \times 12 \times 12$ mm. The accuracy of the dimensions was measured to be ≤ 0.04 mm. This phantom is scanned

10 times using the edges of the cube to select the scan volume. After each scan, new optical images are acquired and the scan volume is marked.

The first 5 scans are performed without removing the bed, while for the last 5 scans the bed containing the phantom is removed from the scanner and remounted before the next acquisition. When the system is properly calibrated, the position of the point sources in all reconstructed volumes should match with the known locations inside the cube. Furthermore, the deviations between the different scans will show the reproducibility of the positioning with the XYZ stage and the mounting mechanism of the bed.

Phantom and animal studies

To test the difference between focused and non-focused scanning, we performed resolution phantom scans and a mouse heart scan using three different protocols to select the volume of interest: (i) a non-focused scan, (ii) a medium-focused scan with the selection limited to the *z*-direction and (iii) a highly-focused scan with the selection in *x*,*y* and *z*-direction. The selected volumes for the different protocols are shown in figure 4.

The resolution phantom consists of several sections containing capillaries with diameters of 0.35, 0.40, 0.45, 0.50, 0.60 and 0.75 mm. The distance between the capillaries in each section is equal to the rod diameter in that section. This phantom was filled with 145 MBq Tc-99m. A 10 minute acquisition was performed for each of the protocols using a collimator with 0.35 mm pinholes. To obtain a low count study of the same phantom, the 3 scans were repeated after 20 hours. In this case a collimator with 0.6 mm pinholes was used. For all scans of the resolution phantom, the total number of photons was calculated in a 20 % energy window to determine the sensitivity for each of the different protocols.

For the mouse heart study, a 29 g male mouse (C57BL/6JO1aHsd, Harlan, the Netherlands) was injected with 0.3 ml tetrafosmin containing 580 MBq Tc-99m. The animal study was conducted following protocols as approved by the animal research committee of the University Medical Center Utrecht. One and a half hour after injection the first SPECT scan of 60 minutes was performed. To compensate for the decay of the isotope, the scan time for the 2nd and 3rd scan was extended to 67 and 76 minutes respectively.

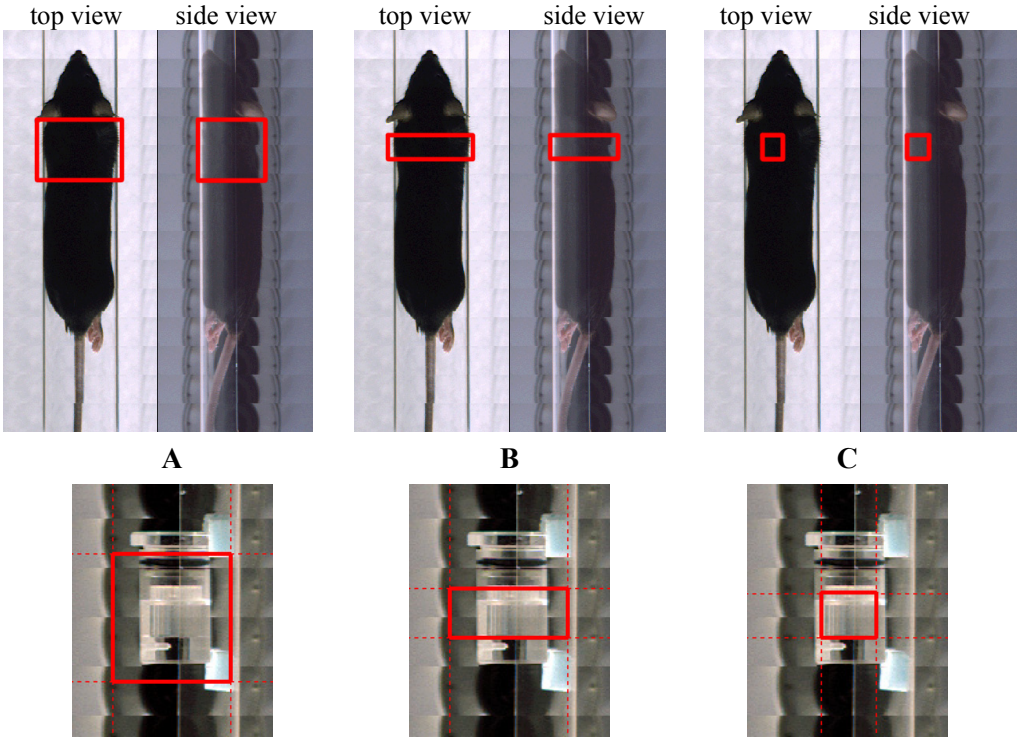

Figure 4: Different volume selection for a mouse heart and a resolution phantom. (A) non-focused scan, (B) medium-focused scan with the selection limited to one direction, (C) highly-focused scan with selection in all directions. Color figure available in appendix.

Results

Accuracy measurements

A reconstructed image from the point source phantom is shown in figure 5. In this image, the expected locations of the point sources are marked with a small cross. The position of the center of mass of the point sources is calculated for all reconstructed images from the different acquisitions of this phantom. The maximum distance between the center of mass to the expected location of a point source was 0.48 mm. For selection of a volume which is approximately the size of a mouse organ, this small deviation will be no problem and we find the calibration of the webcam images and the alignment between the webcams and the collimator is accurate enough for this task.

A maximum deviation of 0.11 mm was measured between two scans without removing the bed and the average deviation was 0.05 mm. This indicates that the precision of the XYZ system is sufficiently accurate for a system with 0.35 mm reconstructed resolution. When the bed was removed after one scan and remounted for the next scan, the maximum deviation between the reconstructed point sources was 0.45 mm.

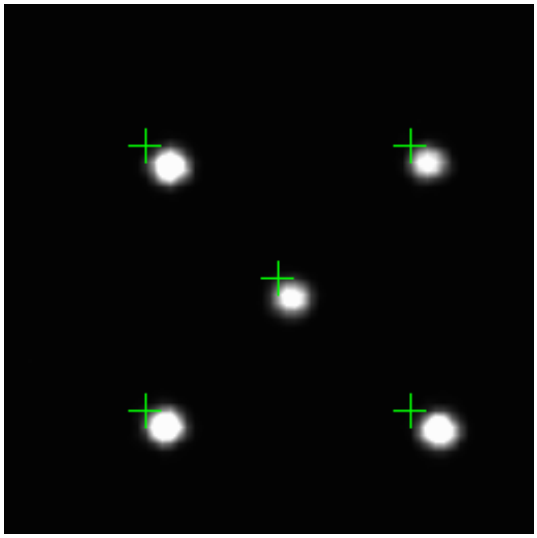

Figure 5: Reconstructed image from the point source phantom showing the point sources as white dots. The expected locations of the sources are marked with a small cross.

Resolution phantom scans

The reconstructed images from the resolution phantom scans are shown in figure 6. The top row contains the images from the high count study with 0.35 mm pinholes and the bottom row shows the images from the low count study using 0.6 mm pinholes. In both cases, the amount of focus has significant impact on the image quality. The highly-focused scan shows higher resolution and less noise than the medium-focused and non-focused scan. The number of counts obtained with the different scan protocols for the resolution phantom study are listed in table 1. For all cases, a 20 % window around 140 keV is used. A sensitivity increase of approximately 250 % can be realized by performing a highly-focused scan instead of a non-focused scan.

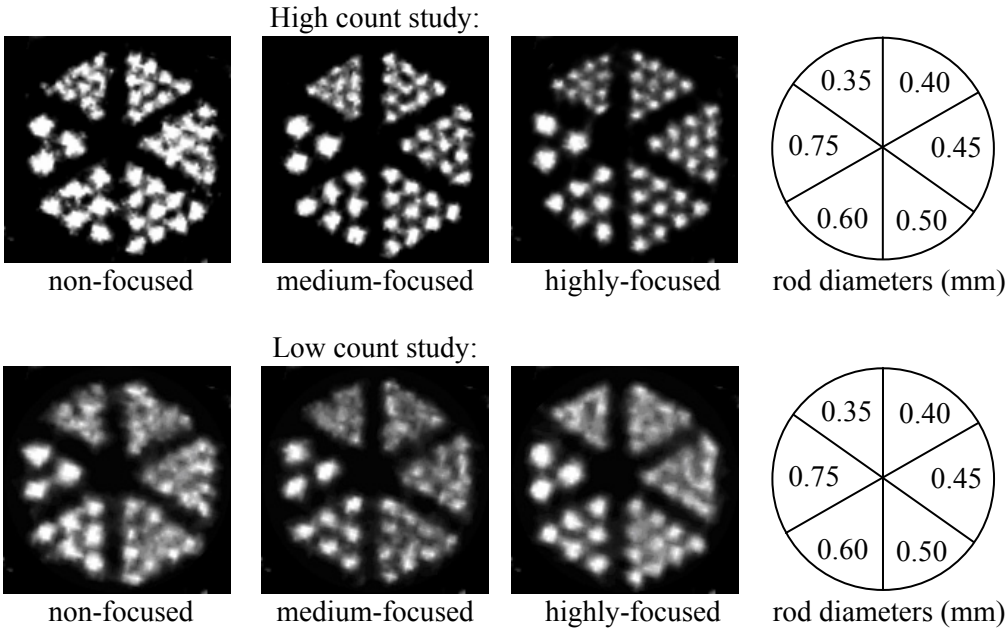

Figure 6: Reconstructed images of the resolution phantom obtained with different scan protocols representing different levels of focus. Top row: high count study using 0.35 mm pinholes. Bottom row: low count study using 0.6 mm pinholes.

	non-focused	medium-focused (*z* direction)	highly-focused (*xyz* direction)
High count study:			
Number of counts	10070563	23458496	35763763
Sensitivity	100 %	232.94 %	355.13 %
Low count study:			
Number of counts	2883632	6660745	9830920
Sensitivity	100 %	230.98 %	340.92 %

Table 1: The number of counts in a 20 % window around 140 keV and the relative sensitivity for the resolution phantom measurements obtained with the different scan protocols.

Mouse heart scans

Slices through the reconstructed images from the mouse heart scan are shown in figure 7. The highly-focused scan shows a better resolution and contrast than the medium-focused scan and clearly outperforms the image quality of the non-focused image.

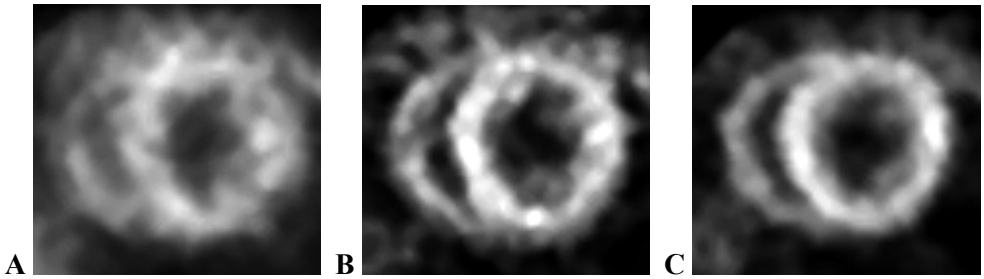

Figure 7: Reconstructed images of the mouse heart scan. (A) non-focused (B) medium-focused (C) highly-focused scan.

Discussion

Measurements from the point source phantom show that the alignment between the images from the optical cameras and the reconstructed volumes is sufficiently accurate for the current application of using the webcams to select the VOI for the SPECT scan. The maximum distance between the center of mass of a point source to the expected location of a point source was 0.48 mm. There is a clear shift between the expected and reconstructed locations for all point sources in the phantom (figure 5). To further improve the alignment between the webcams and the collimator, this offset can be eliminated by incorporating this offset into the matrix used for image reconstruction.

Using the webcam based selection is an easy and effective method to define the scan volume. However, the localization of an organ of interest inside the animal, based on the optical cameras only can be difficult. This task would be greatly facilitated by having an atlas of the anatomy of the animal which is registered to the animal outlines of the webcam images. Moreover, this anatomy enhanced organ selection would be more reliable, which in turn would increase the sensitivity and resolution. We have tested an implementation where we use a digital 3D mouse phantom [25] as anatomical data set. The phantom is non-rigidly transformed to a target animal using a set of anatomical landmarks derived from CT data [26]. In contrast to the work in [26], we do not have to deal with large variations in posture and shape since we are using the same animal holder for each scan. Therefore we restrict ourselves to deriving anatomical landmarks on the skin contours of the animal on two orthogonal webcam images. We assume that the animal is put on the holder in

prone or supine position with no rotation with respect to the anteroposterior axis and that the lateral extent of the animal is restricted by the holder. We subsequently map the 3D mouse phantom to the webcam reference frame and generate 2D projections onto each of the optical images. Finally, the user can select an organ of interest and therefore define the scan volume. One example of a registered phantom where several organs are projected onto the animal is shown in figure 8. Currently, the landmarks which define the outline of the animal on the webcam images are marked manually. However, an automated procedure for this is under development.

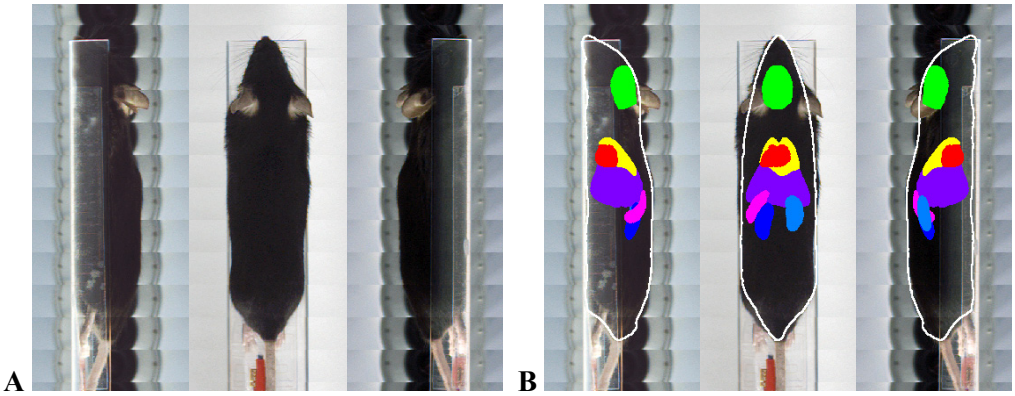

Figure 8: (A) Images from a mouse from the left, top and right webcams. (B) Same images with projections of the registered anatomical dataset containing the outline of the animal, the brain, the lungs, the heart, the spleen, the liver and the kidneys. Color figure available in appendix.

Conclusion

With the focusing multi-pinhole design of the U-SPECT-II system, very high sensitivity in the center of the focus is achieved. This enables imaging of organs with resolutions up to 0.35 mm [6]. Accurate positioning of the focus allows one to take even more advantage of this high sensitivity. Resolution phantom studies and *in vivo* mouse scans show that highly-focused VOI selection significantly improves the reconstructed image quality. A sensitivity increase of approximately 250 % was obtained by using a highly-focused scan volume in all directions instead of a non-focused scan volume. Using images from optical cameras is a very user-friendly way to select a VOI and accomplish accurate positioning of the focus in the animal. The selection and localization of specific organs can be further enhanced by using atlases of anatomy which are registered to the optical images.

Acknowledgements

This work was sponsored by the Medical Council of Netherlands Organization for Scientific Research, grant 917.036.335. We like to thank Ruud Ramakers for technical support and his help during measurements and image reconstructions.

References

[1] Beekman FJ, van der Have F, Vastenhouw B, van der Linden AJA, van Rijk PP, Burbach JPH and Smidt MP, 'U-SPECT-I: A novel system for submillimeter-resolution tomography with radiolabeled molecules in mice', *J. Nucl. Med.* 2005; 46(7): 1194 – 1200.

[2] Beekman FJ and Vastenhouw B, 'Design and simulation of a high-resolution stationary SPECT system for small animals', *Phys. Med. Biol.* 2004; 49: 4579–4592.

[3] Beekman FJ, Vastenhouw B, and van der Have F, 'Towards 3D nuclear microscopy using locally focusing many-pinhole SPECT', *Proceedings of the 2003 International Meeting on Fully Three-Dimensional Image Reconstruction in Radiology and Nuclear Medicine.*

[4] Cao Z, Bal G, Accorsi R, and Acton PD, 'Optimal number of pinholes in multi-pinhole SPECT for mouse brain imaging — a simulation study', *Phys. Med. Biol.* 2005; 50(19): 4609–4624.

[5] Furenlid LR, Wilson DW, Chen YC, Kim H, Pietraski PJ, Crawford MJ, and Barrett HH, 'FastSPECT II: A second-generation high-resolution dynamic SPECT imager', *IEEE Trans. Nucl. Sci.* 2004; 51(3): 631–635.

[6] van der Have F, Vastenhouw B, Ramakers RM, Branderhorst WJ, Krah JO, Ji C, Staelens SG and Beekman FJ, 'U-SPECT-II: an ultra-high resolution device for molecular small-animal imaging', submitted 2008.

[7] Goertzen AL, Jones DW, Seidel J, Li K and Green MV, 'First Results From the High-Resolution mouseSPECT Annular Scintillation Camera.', *IEEE Trans. Med. Imaging.* 2005; 24: 863-867.

[8] Ishizu K, Mukai T, Yonekura Y, Pagani M, Fujita T, Tamaki N, Shibasaki H and Konishi J, 'Ultra-high-resolution SPECT system using four pinhole collimators for small animal studies', *J. Nucl. Med.* 1995; 26: 2282–2289.

[9] Ivanovic M, Weber DA and Loncaric S, 'Multi-pinhole collimator optimization for high resolution SPECT imaging', *IEEE Nuclear Science Symposium.* 1997; 2, 1097–1101.

[10] Jaszczak RJ, Li J, Wang H, Zalutsky MR and Coleman RE, 'Pinhole collimation for ultra-high-resolution small-field-of-view SPECT', *Phys. Med. Biol.* 1994; 39: 425–437.

[11] King M.A., Pretorius P.H., Farncombe T. and Beekman F.J., 'Introduction to the physics of molecular imaging with radioactive tracers in small animals', *J. Cell. Biochem.* 2002; Suppl. 339: 221–230.

[12] McElroy DP, MacDonald LR, Beekman FJ, Wang Y, Patt BE, Iwanczyk JS, Tsui BMW and Hoffman EJ, 'Performance evaluation of A-SPECT: A high resolution desktop pinhole SPECT system for imaging small animals', *IEEE Trans. Nucl. Sci.* 2002; 49: 2139–2147.

[13] Meikle SR, Kench P, Weisenberger AG, Wojcik R, Smith MF, Majewski S, Eberl S, Fulton RR, Rosenfeld AB and Fulham MJ, 'A prototype coded aperture detector for small animal SPECT', *IEEE Trans. Nucl. Sci.* 2002; 49(5): 2167–2171.

[14] Palmer J and Wollmer P, 'Pinhole emission computed tomography: method and experimental evaluation', *Phys. Med. Biol.* 1990; 35(3): 339-50.

[15] Rentmeester MCM, van der Have F and Beekman FJ, 'Optimizing multi-pinhole SPECT geometries using an analytical model', *Phys. Med. Biol.* 2007; 52: 2567-2581.

[16] Rogulski MM, Barber HB, Barrett HH, Shoemaker RL and Woolfenden JM, 'Ultra-high-resolution Brain spect imagine: Simulation results', *IEEE Trans. Nucl. Sci.* 1993; 40: 1123–1129.

[17] Rowe RK, Aarsvold JN, Barrett HH, Chen JC, Klein WP, Moore BA, Pang IW, Patton DD and White TA 'A stationary hemispherical SPECT imager for three-dimensional brain imaging', *J. Nucl. Med.* 1993; 34: 474–480.

[18] Schramm N, Wirrwar A and Halling H, 'Development of a multi-pinhole detector for high-sensitivity SPECT imaging'*, Conference Record of 2001 IEEE Nuclear Science Symposium and Medical Imaging Conference, San Diego, USA,* 2001; 3: 1585–1586.

[19] Schramm NU, Ebel G, Engeland U, Schurrat T, Béhé M and Behr TM, 'High-Resolution SPECT Using Multipinhole Collimation', *IEEE Trans. Nucl. Sci.* 2003; 50(3): 315-320.

[20] Weber DA and Ivanovic M, 'Ultra-high-resolution imaging of small animals: implications for preclinical and research studies'*, J. Nucl. Card.* 1999; 6: 332–344.

[21] Wu MC, Tang HR, Gao DW, Ido A, O'Connell JW, Hasegawa BH and Dae MW, 'ECG gated pinhole SPECT in mice with millimeter resolution', *IEEE Trans. Nucl. Sci.* 2000; 47: 1218–1227.

[22] Beekman FJ and van der Have F, 'The pinhole: Gateway to ultra-high resolution three-dimensional radionuclide imaging', *Eur. J. Nucl. Med. Molec. Im.* 2007; 34: 151-161.

[23] Vastenhouw B and Beekman FJ, 'Submillimeter total-body murine imaging with U-SPECT-I', *J. Nucl. Med.* 2007; 48(3): 487-493.

[24] Vastenhouw B, van der Have F, van der Lindern AJA, von Oerthel L, Booij J, Burbach JPH, Smidt MP, Beekman FJ, 'Movies of dopamine transporter occupancy with ultra-high resolution focusing SPECT', *Mol. Psych.* 2007; 12: 984-987.

[25] Segars WP, Tsui BMW, Frey EC, Johnson GA, and Berr SS, 'Development of a 4D digital mouse phantom for molecular imaging research', *Mol. Imaging Biol.* 2004; 6(3): 149–159.

[26] Baiker M, Dijkstra J, Que I, Löwik CWGM, Reiber JHC and Lelieveldt BPF, 'Organ approximation in CT data with low soft tissue contrast using an articulated whole-body atlas', *Proc. IEEE Intl. Symp. on Biomedical Imaging*, 2008: 1267–1270.

Chapter 7

Movies of dopamine transporter occupancy with ultra-high resolution focusing pinhole SPECT

Brendan Vastenhouw, Frans van der Have, Annemarie J.A. van der Linden, Lars von Oerthel, Jan Booij, J. Peter H. Burbach, Marten P. Smidt and Freek J. Beekman

Molecular Psychiatry, 2007; 12: 984-987.

Abstract

A pivotal question in neuropharmacology is how the function of neurotransmitter systems relates to psychiatric diseases. In experimental neuropharmacology, we have dreamt about a looking glass that would allow us to see neurotransmitter systems in action, and about animals that would faithfully serve us as models for human psychiatric disease. Analysis of animal models has been limited by the availability of methods to study *in vivo* neurotransmitter dynamics. Now, a single photon emission computed tomography system called U-SPECT can localize dopamine transporters in sub-compartments of the mouse brain during a range of points in time. Applied to the midbrain dopamine system of different models of disease, this will aid the understanding of dynamic processes of this neurotransmitter that underlie brain functions and human brain pathology.

Functional imaging techniques such as positron emission tomography (PET) and single photon emission computed tomography (SPECT) have revolutionized human neuropharmacology in the nineties. They allowed us to experience part of our dream to see neurotransmitter systems in action in the living brain and emerged as important means to study aspects of neurotransmission systems *in vivo*, such as transporter and receptor densities (for a review see [1]). For the dopamine system, the imaging of the dopamine transporter (DAT) has become increasingly important since the DAT is subject to extensive modulation as a consequence of degenerating dopaminergic neurons in Parkinson's disease, and as the primary target of drugs of abuse, such as cocaine [2.3]. Its function, the re-uptake of dopamine from the synaptic cleft, is crucial in the damping of dopaminergic transmission in the striatum, essential for movement control, attention and mood state. Since the DAT is implicated in neurological and psychiatric diseases of the central nervous system as Parkinson's disease, Alzheimer's disease, ADHD, schizophrenia, Tourettes syndrome, obesity and depression [4], it has become a major target for development of new pharmacotherapies. In line with this, the properties of DAT imaging have provided a window to the brain. Initially, PET and SPECT have proven their relevance in DAT imaging in preclinical and clinical Parkinson's disease [5-9], providing the means to use these techniques as specific diagnostic tools. The development of new therapies and diagnostic tools rely heavily on the development and analysis of animal models. In this respect, dedicated PET and SPECT systems that enable imaging of the dopamine system in small laboratory animals are essential assets. Although these systems have shown the feasibility to detect DAT in rats and mice [10-12], these systems lack the spatial and temporal resolution to study fast dynamic aspects of DAT occupancy as a measure of the state of dopaminergic tonus and release parameters in anatomical subdivisions of the forebrain.

We recently developed an ultra-high resolution pinhole SPECT system (U-SPECT-I [13]) which enables rapid dynamic and sub-millimeter resolution imaging in rodents. Most animal SPECT systems use one, up to a couple independent pinhole detectors that can acquire only a subset of the projections at the time while heavy SPECT detectors need be rotated several times to acquire projections under a sufficient number of angles. Stationary pinhole approaches were reviewed in [14]. U-SPECT-I has stationary detectors and utilizes a cylindrical tungsten collimator in which 69 gold pinhole apertures are mounted that all focus on a small volume in the animal to maximize the detection yield of gamma-quanta emitted from the brain. From the 69 simultaneously acquired projections, 3D SPECT images are reconstructed using the Maximum Likelihood Expectation Maximization (ML-EM) algorithm [15]. Recovery of resolution losses due to the finite pinhole size and gamma-camera blurring is performed by accurately modeling these effects during ML-EM reconstruction [13]. With 0.6 mm pinhole apertures a resolution of less than 0.5 mm can be obtained, while a resolution of 0.35 mm have been reached with smaller pinholes [14]. Rapid temporal processes can be imaged since effectively the pinhole cameras surround the animal while simultaneously observing the mouse brain. Here we demonstrate that with the U-SPECT-I system DAT imaging is possible with a sub-millimeter resolution and sub-minute time frames in the mouse brain, allowing imaging of the immediate action of an addictive drug.

To analyze *in vivo* DAT occupancy in a dynamic context in the mouse, 140 MBq [^{123}I]*N*-ω-fluoropropyl-2ß-carbomethoxy-3ß-(4-iodophenyl)nortropane (FP-CIT [16]), a DAT radioligand, was injected intraperitoneally in male C57BL/6J mouse (body weight approximately 30 g). SPECT projection data acquisitions of 45 seconds each were obtained, starting approximately 3 hours and 40 minutes post injection. Cocaine (30 mg/kg) was administered intraperitoneally 4 hours after injecting FP-CIT. From the reconstructed 3D SPECT images, movies of DAT-ligand (radioactivity) displacement in the striatum and associated regional time activity curves were generated from 17 minutes before the administration of the cocaine, up to 28 minutes after administration. The movie (available on-line at www.isi.uu.nl/People/Freek/"FP-CIT_displacement") of which snapshots are presented in figure 1, shows tracer concentrations in fixed volumes of interest, positioned over the striatum bilaterally. From 17 minutes before administration of the cocaine up to 3 minutes after its administration the striatal [^{123}I]FP-CIT concentration was stable. Thereafter it rapidly declined, with about 50 % loss of DAT-binding at 28 minutes after cocaine injection.

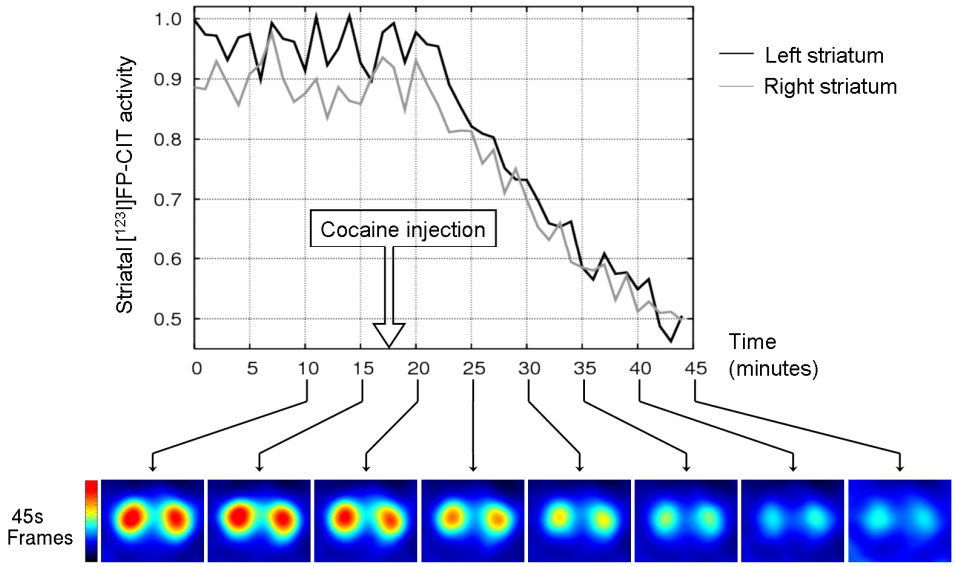

Figure 1: Coronal SPECT slices at the level of the striatum of a mouse. To label the DAT *in vivo*, [^{123}I]*N*-ω-fluoropropyl-2ß-carbomethoxy-3ß-(4-iodophenyl) nortropane ([^{123}I]FP-CIT) was used as a radiotracer and the new U-SPECT multiple pinhole technique was used to detect radiation emitted by ^{123}I labels. Before and up to about 3 minutes after administration of cocaine (i.p. 30 mg/kg body weight) a stable level of radioactivity is measured in the striatum representing a stable binding of FP-CIT to the DAT. Thereafter, cocaine starts occupying the DAT and displaces [^{123}I]FP-CIT binding, which is shown in the images and the associated curve. Approximately 28 minutes after the administration of cocaine, about 50 % of activity has been displaced by cocaine which indicates that the DAT rapidly binds cocaine. Color figure available in appendix.

To demonstrate the feasibility of resolving DAT-ligand binding in very small volumes, down to sub-compartments of the brain, we performed a long SPECT acquisition (40 minutes, figure 2 frames A and C). In this case 38 MBq FP-CIT was injected in a male mouse (C57BL/6J, 30 g). A special data acquisition mode combined with an adapted ML-EM reconstruction algorithm [17] was used that shifts the animal through the pinhole focus by a couple of mm per step during scanning to cover a larger area in the animal. Validation of the accuracy of the DAT-binding obtained with this SPECT procedure was performed using autoradiography which was derived and adjusted from [18,19]. Briefly, the coronal sections (16 µM) were pre-incubated in 50 mM Tris-HCl 120 mM NaCl (pH 7.5) for 20 minutes. Incubation was performed in 50 mM Tris-HCl 120 mM NaCl (pH 7.5) containing 50 pM

[^{125}I]RTI-55 and 1 uM Citalopram (a selective serotonin transporter re-uptake inhibitor) and Nisoxetine (selective norepinephrine transporter blocker), (400 ul) for 60 minutes. To determine the non-specific binding, control sections were incubated with the addition of 1 uM of GBR12909 (selective DAT blocker). Slides were rinsed twice for 10 seconds at 4^{o} C with the incubation buffer in containers. After that they were dipped rapidly in de-ionized water, dried under airflow, and imaged using a phosphor imager (Bas 5000, Fuji-Film).

On the SPECT images shown in figure 2 (frames A and C), different sub-striatal structures can be distinguished from each other, as the caudate putamen, nucleus accumbens and olfactory tubercle. The similarity between the SPECT image and the autoradiogram (figure 2 frames B and D) validates the accuracy to image DAT in the sub-millimeter range using this new focusing pinhole SPECT technique. This technique opens possibilities to distinguish different modes of action in dopamine transmission in relation to CNS disease and (new) pharmacotherapies, which in a later stage can be used in human CNS pathology. Moreover, the dynamic process of occupancy of transporters such as DAT or receptors influenced by endogenous neurotransmitter release or peripheral administrated drugs (of abuse) can be visualized and therefore used to gain a better understanding of how and why specific pharmacotherapy works to alleviate symptoms in for example ADHD and schizophrenia. This adds to the possibilities of analysis of specific disease processes in terms of dopaminergic-transmission dynamics. Moreover, the ability to monitor *in vivo* fast changes in the expression of DAT may be crucial to better understand the temporal coordination of this transporter *in vivo*. Due to its high time- and spatial resolution, this highly focusing pinhole SPECT technique offers the unique opportunity to characterize new SPECT tracers for potentially all kinds of receptors, which will be of importance for future research on neuropsychiatric diseases. Taken together, neuroreceptor imaging *in vivo* with a new technique which offers not only a high spatial resolution but also a high time-resolution may not only improve our understanding of the pathophysiology of neuropsychiatric diseases, but it may be also of value to evaluate new potential diagnostic tracers and to monitor new therapeutic treatments, which in the end will improve our knowledge of neuropsychiatric diseases in humans.

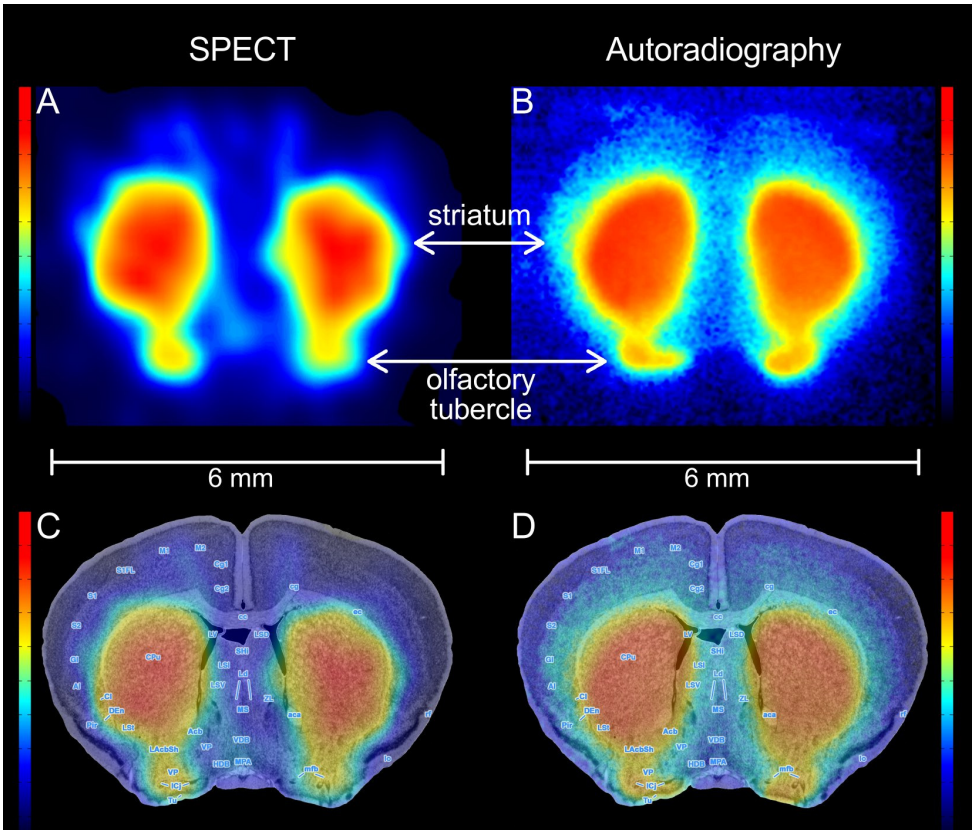

Figure 2: High resolution *in vivo* imaging of striatal DAT (left) compared to DAT autoradiography (right). (A) Coronal SPECT slice of the striatum, showing the possibility to distinguish sub-striatial structures through DAT binding of [^{123}I]FP-CIT. (B) Autoradiogram at the level of the striatum and olfactory tubercle of a mouse brain postmortem. Please note, that the autoradiography and SPECT images look similar, suggesting that pinhole SPECT is able to delineate DAT binding within a sub-millimeter range (C) SPECT slice overlaid on an anatomic brain atlas of the mouse [20,21]. (D) Autoradiogram overlaid on anatomic brain atlas. Color figure available in appendix.

References

[1] Booij J, Tissingh G, Winogrodzka A, van Royen EA, 'Imaging of the dopaminergic neurotransmission system using single-photon emission tomography and positron emission tomography in patients with Parkinsonism', *Eur. J. Nucl. Med.* 1999; 26: 171-182.

[2] Ritz MC, Lamb RJ, Goldberg SR, Kuhar MJ, 'Cocaine receptors on dopamine transporters are related to self-administration of cocaine', *Science.* 1987; 237: 1219-1223.

[3] Volkow ND, Wang GJ, Fischman MW, Foltin RW, Fowler JS, Abumrad NN et al., 'Relationship between subjective effects of cocaine and dopamine transporter occupancy', *Nature.* 1997; 386: 827-830.

[4] Runyon SP, Carroll FI, 'Dopamine transporter ligands: recent developments and therapeutic potential', *Curr. Top. Med. Chem.* 2006; 6: 1825-1843.

[5] Lee CS, Samii A, Sossi V, Ruth TJ, Schulzer M, Holden JE, et al., 'In vivo positron emission tomographic evidence for compensatory changes in presynaptic dopaminergic nerve terminals in Parkinson's disease'. *Ann. Neurol.* 2000; 47: 493-503.

[6] Marek KL, Seibyl JP, Zoghbi SS, Zea-Ponce Y, Baldwin RM, Fussell B, et al. '[123I]beta-CIT/SPECT imaging demonstrates bilateral loss of dopamine transporters in hemi-Parkinson's disease', *Neurology.* 1996; 46: 231-237.

[7] Tissingh G, Booij J, Bergmans P, Winogrodzka A, Janssen AG, van Royen EA, et al.., 'Iodine-123-N-omega-fluoropropyl-2beta-carbomethoxy-3beta-(4-iod ophenyl)tropane SPECT in healthy controls and early-stage, drug-naive Parkinson's disease', *J. Nucl. Med.* 1998; 39: 1143-1148.

[8] Ponsen MM, Stoffers D, Booij J, van Eck-Smit BL, Wolters ECh, Berendse HW. 'Idiopathic hyposmia as a preclinical sign of Parkinson's disease', *Ann. Neurol.* 2004; 56: 173-181.

[9] Stiasny-Kolster K, Doerr Y, Moller JC, Hoffken H, Behr TM, Oertel WH, et al., 'Combination of 'idiopathic' REM sleep behaviour disorder and olfactory dysfunction as possible indicator for alpha-synucleinopathy demonstrated by dopamine transporter FP-CIT-SPECT', *Brain.* 2005; 128: 126-137.

[10] Nikolaus S, Beu M, Wirrwar A, Antke C, Muller HW. '*In vivo* snapshots of the dopaminergic synapse in small animals', *Mol. Psych.* 2005; 10: 516-518.

[11] Andringa G, Drukarch B, Bol JG, de Bruin K, Sorman K, Habraken JB, et al., 'Pinhole SPECT imaging of dopamine transporters correlates with dopamine transporter immunohistochemical analysis in the MPTP mouse model of Parkinson's disease', *Neuroimage.* 2005; 26: 1150-1158.

[12] Inaji M, Yoshizaki T, Okauchi T, Maeda J, Nagai Y, Nariai T, et al., 'In vivo PET measurements with [11C]PE2I to evaluate fetal mesencephalic transplantations to unilateral 6-OHDA-lesioned rats', *Cell Transplant.* 2005; 14: 655-663.

[13] Beekman FJ, van der Have F, Vastenhouw B, van der Linden AJA, van Rijk PP, Burbach JPH *et al*. 'U-SPECT-I: a novel system for submillimeter-resolution tomography with radiolabeled molecules in mice' *J Nucl Med* 2005; 46: 1194-1200.

[14] Beekman F, van der Have F, 'The pinhole: gateway to ultra-high-resolution three-dimensional radionuclide imaging', *Eur. J. Nucl. Med. Mol. Im.* 2007; 34: 151-161.

[15] Lange K, Carson R. 'EM reconstruction algorithms for emission and transmission tomography', *J. Comput. Assist. Tomogr.* 1984; 8: 306-316.

[16] Neumeyer JL, Wang S, Gao Y, Milius RA, Kula NS, Campbell A, et al., 'N-omega-fluoroalkyl analogs of (1R)-2 beta-carbomethoxy-3 beta-(4-iodophenyl)-tropane (beta-CIT): radiotracers for positron emission tomography and single photon emission computed tomography imaging of dopamine transporters', *J. Med. Chem.* 1994; 37: 1558-1561.

[17] Vastenhouw B, Beekman F, 'Submillimeter total-body murine imaging with U-SPECT-I', *J. Nucl. Med.* 2007; 48: 487-493.

[18] Kindlundh AM, Rahman S, Lindblom J, Nyberg F, 'Increased dopamine transporter density in the male rat brain following chronic nandrolone decanoate administration', *Neurosci. Lett.* 2004; 356: 131-134.

[19] Kula NS, Baldessarini RJ, Tarazi FI, Fisser R, Wang S, Trometer J, et al., '[3H]beta-CIT: a radioligand for dopamine transporters in rat brain tissue', *Eur. J. Pharmacol.* 1999; 385: 291-294.

[20] Rosen GD, Williams AG, Capra JA, Connolly MT, Cruz B, Lu L, Airey DC, Kulkarni K, Williams RW, 'The Mouse Brain Library [www.mbl.org]', *Int. Mouse Genome Conference.* 2000; 14: 166.

[21] Williams RW, 'Mapping genes that modulate mouse brain development: a quantitative genetic approach', *Results Probl. Cell. Differ.* 2000; 30: 21-49.

Chapter 8

Design and simulation of a high-resolution stationary SPECT system for small animals

Freek J. Beekman and Brendan Vastenhouw

Physics in Medicine and Biology, 2004; 49: 4579-4592.

Abstract

Exciting new SPECT systems can be created by combining pinhole imaging with compact high-resolution gamma cameras. These new systems are able to solve the problem of the limited sensitivity-resolution trade-off that hampers contemporary small animal SPECT. The design presented here (U-SPECT-III) uses a set of detectors placed in a polygonal configuration and a cylindrical collimator that contains 135 pinholes arranged in nine rings. Each ring contains 15 gold pinhole apertures that focus on the centre of the cylinder. A non-overlapping projection is acquired via each pinhole. Consequently, when a mouse brain is placed in the central field-of-view, each voxel in the cerebrum can be observed via 130 to 135 different pinholes simultaneously. A method for high-resolution scintillation detection is described that eliminates the depth-of-interaction problem encountered with pinhole cameras, and is expected to provide intrinsic detector resolutions better than 150 μm. By means of simulations U-SPECT-III is compared to a simulated dual pinhole SPECT (DP-SPECT) system with a pixelated array consisting of 2.0 × 2.0 mm NaI crystals. Analytic calculations indicate that the proposed U-SPECT-III system yields an almost four times higher linear and about sixty times higher volumetric system resolution than DP-SPECT, when the systems are compared at matching system sensitivity. In addition, it should be possible to achieve a 15 up to 30 times higher sensitivity with U-SPECT-III when the systems are compared at equal resolution. Simulated images of a digital mouse-brain phantom show much more detail with U-SPECT-III than with DP-SPECT. In a resolution phantom, 0.3 mm diameter cold rods are clearly visible with U-SPECT-III, whereas with DP-SPECT the smallest visible rods are about 0.6–0.8 mm. Furthermore, with U-SPECT-III, the image deformations outside the central plane of reconstruction that hamper conventional pinhole SPECT are strongly suppressed. Simulation results indicate that future pinhole SPECT systems are likely to bring about significant improvements in radio-molecular imaging of small animals.

Introduction

Pinhole SPECT permits radio-labelled molecule distributions to be imaged *in vivo* in small animals. Several small animal SPECT systems have been developed recently [1-9]. In addition to SPECT systems, dedicated small animal PET systems have been devised for the imaging of radio-actively labelled molecules (reviewed in [10]). The small animal versions of CT, PET and SPECT are sometimes referred to as micro-CT, micro-PET and micro-SPECT, respectively. An introduction to the physics of small animal SPECT and PET systems can be found in [11]. The applications of SPECT and PET partly overlap and are often complementary. The method that will be chosen for a particular application will depend on matters such as equipment costs,

infrastructure, required resolution and count sensitivity and will be influenced by factors such as logistics, costs and the availability of the specific radio-molecules required.

With pinhole SPECT, high spatial resolution projection data can be obtained, particularly in small organs. For example, it has been shown experimentally that in the thyroid of a mouse (typical size 1 × 1 mm), an image resolution as good as 200 μm can be obtained in pinhole projection images [12] and about 500 μm in reconstructed pinhole SPECT volume-images [7,9]. A serious drawback of SPECT compared to PET is the limited photon counting sensitivity; the latter is decreased even further when small pinholes are used for obtaining a high resolution. An important reason for low sensitivity is that most contemporary pinhole SPECT systems are based on the use of conventional scintillation cameras with a typical intrinsic resolution of approx. 2–3.5 mm. A large camera is required for such low intrinsic resolutions because a significant projection image magnification is needed to obtain sufficient resolution. Therefore, only a few pinhole cameras can be placed around the animal. Another drawback of conventional SPECT systems is that the cameras need to be rotated in order to obtain sufficient projection angles. This complicates these SPECT devices and makes them difficult to calibrate. In addition, the flexibility to acquire and process dynamic series becomes limited with systems requiring detector rotation. A few groups have managed to create stationary SPECT systems by combining a large number of non-overlapping detectors with multiple pinhole geometries (e.g., [9,13]). When compact high-resolution detectors become available it is possible to place many more small cameras around the subject [14,15]. However, high-resolution detectors are currently very difficult to make and are very expensive. Their production becomes even more complicated if they have to adequately detect photons with medium or high energy that are emitted by isotopes attached to tracer molecules used in clinical imaging (e.g., Tc-99m, I-123, Tl-201). For such energies, methods are required that will eliminate the effects of varying depth-of-interaction of the photons in the detector material in order to further optimize resolution. A number of solutions have been proposed recently (e.g., [15,16,17]).

The goal of the present chapter is (i) to evaluate a new design for a stationary small animal SPECT system (U-SPECT-III) that comprises a novel highly focusing pinhole geometry and special detectors, (ii) to describe a method for reducing parallax errors that arise from depth-of-interaction variations which are inherent to pinhole imaging and (iii) to show that projections obtained with the proposed U-SPECT-III pinhole geometry can yield reconstructions with reduced distortion.

Methods

In this section we discuss the U-SPECT-III system geometry (composition and positioning of pinholes and detectors), the design of a high-resolution detector, the image reconstruction algorithms used and the simulation studies used for evaluation.

Pinhole design and geometry of U-SPECT-III

Cross-sections through the detector and the pinhole set-up of U-SPECT-III are shown in figures 1 and 2. One-hundred-and-thirty-five gold pinhole apertures are placed in a multiple ring geometry. Cross-sections of the head of a mouse (represented by MRI images) inside the U-SPECT-III system are included in these images. The edges of the 15 photon beams passing through the pinhole apertures in one of the nine rings are shown in figure 1. To increase sensitivity, the pinholes are focused on the organ of interest (in this case the brain as can be seen in figure 2): in the outer rings the apertures are placed at a larger angle. In this way, each voxel of the cerebrum of a mouse can be observed via many pinholes simultaneously. A map showing how many apertures can observe a voxel in the object under study is presented in figure 3; voxels in the entire brain of a mouse can be observed via 130 up to 135 pinholes simultaneously. The high photon-counting sensitivity obtained in this way can be traded for increased image resolution by the use of smaller pinholes.

The pinholes can be shaped and baffles can be placed in such a way that approximately rectangular projections are created that do not overlap [18]. Furthermore, the pinhole positions in adjacent rings are rotated over 8° in order to increase the variety of angles at which each voxel is observed. The latter is possible because the object is observed through pinholes in different rings (figure 2). The diameters of the detector ring and the cylinder with pinholes are 150 and 44 mm, respectively.

The gold pinhole apertures in the U-SPECT-III system ensure high photon stopping power, which reduces the blurring caused by radiation penetration and scattering in the aperture edges. In previous studies we have shown that gold gives better results than commonly used materials such as lead or tungsten [19]. The opening angle α of the gold pinhole apertures modeled in U-SPECT-III is 30°.

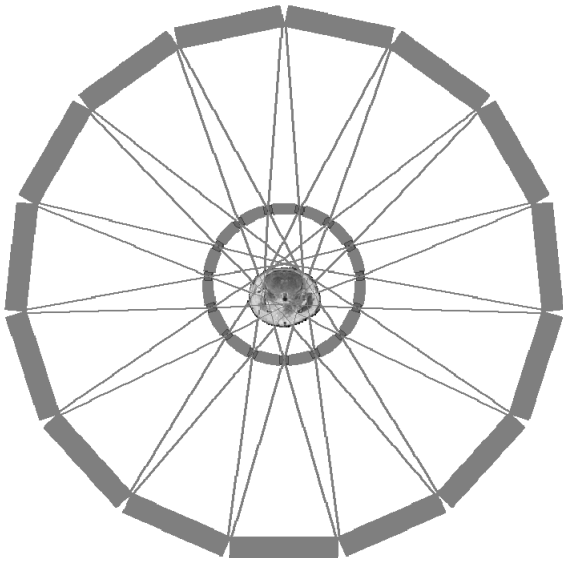

Figure 1: Cross-section through the detector ring and collimator ring with pinholes of the U-SPECT-III system. A tungsten cylinder contains a total of 135 gold pinhole apertures, with 15 pinholes in each ring. Lines mark the triangular cross-sections of beams in which emitted gamma quanta can travel from the mouse brain towards the detector. At the centre of the system a cross-section of a mouse head obtained by MRI imaging is visible.

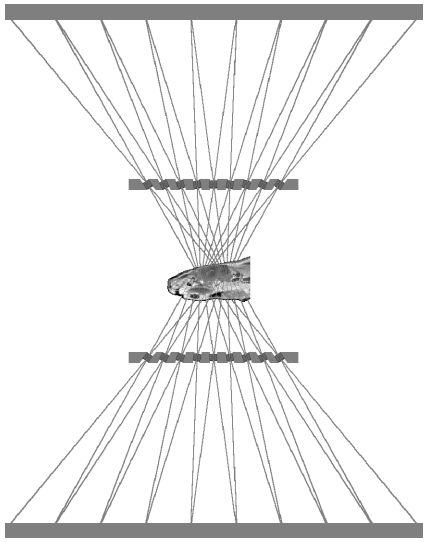

Figure 2: Sagittal cross-section of U-SPECT-III. Pinholes in all rings are focused on the mouse brain in order to maximize count yield from this specific area of interest. Not shown here is that adjacent pinholes rings are trans-axially rotated with regard to each other by 8˚.

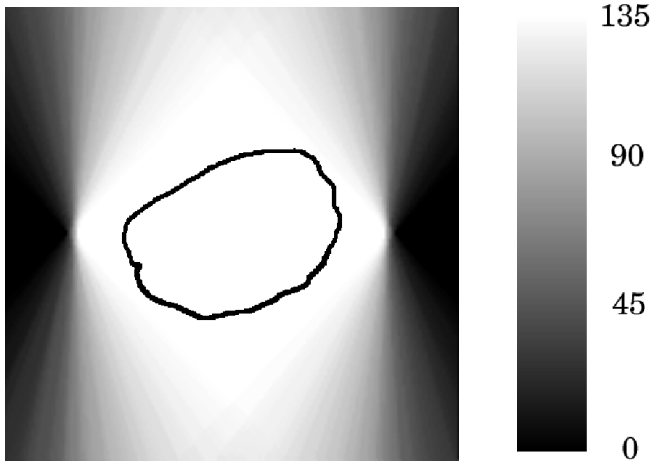

Figure 3: In U-SPECT-III, the number of pinholes that simultaneously observe individual voxels in the fore-and mid-brain area of a mouse ranges from 130 up to 135. A sagittal slice of the brain is displayed together with the outline of the fore-and mid-brain. The grey scale represents the number of pinholes that observe a voxel simultaneously.

High-resolution detector design

It is anticipated that scintillation detectors with an intrinsic resolution of 150 μm can be used in U-SPECT-III (figure 5). In the recent past, such a high resolution could only be achieved with thin crystals (a few hundred microns). For isotopes such as I-125, which emit low-energy photons (27–35 keV), relatively thin crystals are still adequate to secure the required detection yield. Higher energy photons though, such as those emitted by radionuclides like Tc-99m (140 keV), have a very low probability of interaction with such thin crystals. Thicker crystals spread out the scintillation light towards the detector (figure 4A), leading to a significant loss of spatial resolution. In the case of x-ray imaging the problem can be avoided by using crystals consisting of parallel bundles of tiny CsI(Tl) fibers (e.g., [20], figure 4B). However, in the case of pinhole collimation, a 'parallax' error would remain, since the radiation penetrates into the columns at an angle, and therefore the column in which the interaction takes place cannot be determined *a priori*. Consequently, different columns will scintillate when gammas are emitted from a single point P, as shown in figure 4B. This results in an undesirable line pattern instead of a well-defined point-like emission of light at the interface between the crystal and the position-sensitive light detector. This problem can be avoided by directing the fibers towards the pinhole ('cone beam crystals'). Using such crystals, the scintillation light is transmitted along the same direction as the direction travelled by the gamma quantum (figure 4C). As a result, the depth-of-interaction in the scintillator will not influence the place where the light hits the position-sensitive light detector [17]. Since thin CsI fibers (with size of only a

couple of microns) can now be manufactured routinely, and initial experiments with straight parallel fibers coupled to a photon-counting CCD have had promising results (figure 5), it seems reasonable to assume that an intrinsic camera resolution of better than 150 μm will become available not only for I-125, but also for isotopes with a higher energy, such as Tc-99m. A sample image acquired at our lab with straight CsI columns is shown in figure 5; it was obtained by illuminating a columnar crystal with a thickness of 1 mm with a 50 μm wide beam (Co-57, 122 keV). The crystal was mounted on a cooled photon-counting CCD. An intrinsic spatial image resolution of ≈120 μm FWHM was obtained [21]. A slightly poorer intrinsic detector resolution, namely 150 μm, was assumed in the U-SPECT-III simulations presented below, which was modeled by Gaussian blurring prior to detector binning. Furthermore, due to computer memory limitations, the smallest projection pixel binning that could be used during simulation was 150 μm, causing additional blurring.

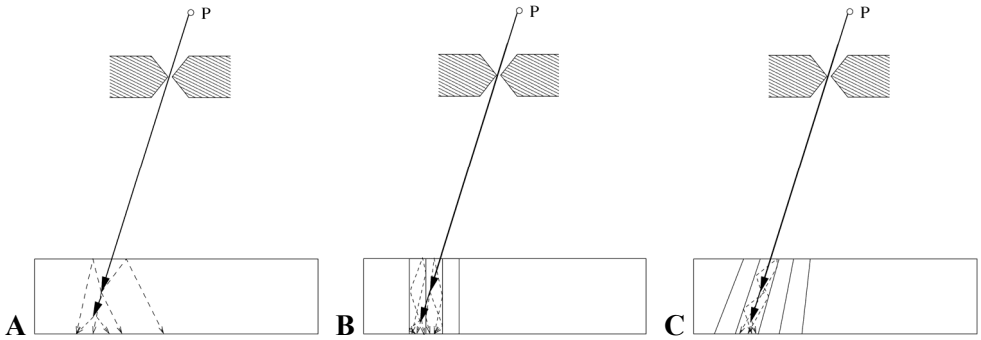

Figure 4: Cross-sectional drawings of a gamma pencil beam coming from point P which enters a micro-pinhole and then interacts with a crystal. Scintillation light is represented by dashed arrows. In a continuous crystal there is a significant spread of light (A). A scintillator composed of columnar crystals prevents light from spreading laterally (B). This solution is still not optimal since with a pinhole camera, gamma-quanta enter the crystal at an angle. This will cause a parallax error since a gamma quantum will interact with a column that is not determined *a priori*. This results in a line-like light spread function rather than a point-like one, because different columns project to different positions at the position-sensitive light detector. This problem could be eliminated by directing columns towards the pinhole (C); then the scintillation light is transported along the same line as the gamma quantum travelling before it interacted with the crystal.

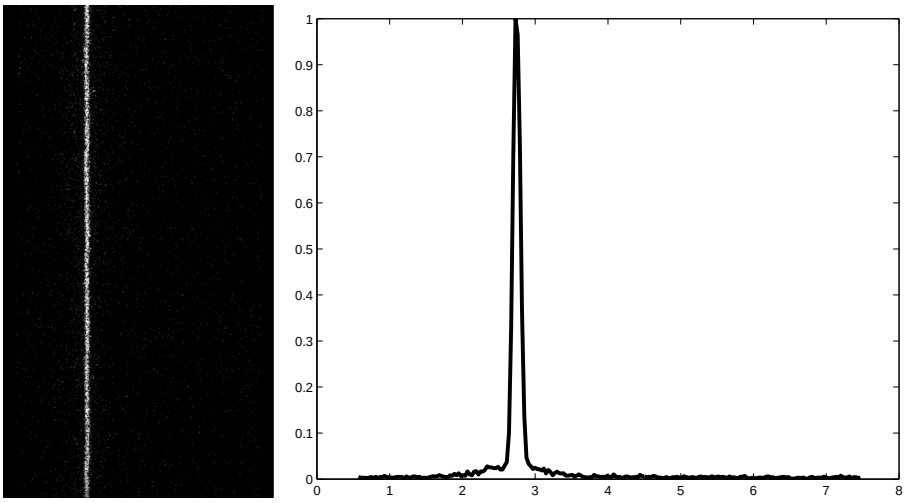

Figure 5: Line pattern response of a columnar crystal read out by a photon-counting CCD, recorded at the Molecular Imaging Physics Lab at Utrecht University [21]. The width of the response was 120 μm FWHM.

System sensitivity and resolution

In addition to the full simulations of the DP-SPECT and U-SPECT-III with extended distributions that are used here to investigate effects of the hardware on reconstructed images, we provide the analytically calculated system sensitivity and system resolution of both devices. These system properties are independent of the reconstruction algorithm, system discretization and phantoms used and are based on recently published mathematical expressions for so-called 'effective' pinhole diameters.

The geometric resolution R_g for a source at distance z from the pinhole reads

$$R_g \approx D_{\text{eff,res}}(l+z)/l$$

where l is the distance between the pinhole and the detector and where $D_{\text{eff,res}}$ is the effective hole diameter in terms of resolution [22]:

$$D_{\text{eff,res}} = D + \frac{\ln(2)}{\mu}\tan\left(\frac{\alpha}{2}\right)$$

with D the physical diameter of the pinhole and α the pinhole opening angle (figure 6). The expression used for calculating the total resolution obtained with a single pinhole R_t in terms of the full-width-at-half-maximum (FWHM) reads

$$R_t \approx \sqrt{\left(\frac{z}{l}R_i\right)^2 + R_g^2}$$

with R_i the intrinsic detector resolution (2.2 mm for DP-SPECT and approx. 150 μm for U-SPECT-III). This expression is also valid for a ring of pinholes when a point source is at the centre of the ring. Pinholes in different rings can produce projections with different resolutions since l and z differ for each ring. The average system resolution R_a for a U-SPECT system with N rings at the centre of the field-of-view is defined here as

$$R_a \approx \frac{\sum_{k=1}^{N} S^k R_t^k}{\sum_{k=1}^{N} S^k}$$

where S^k is the count sensitivity of ring k. The volumetric resolution is defined here as $R_v = R_a^3$.

The contribution ΔS made by a pinhole to the total sensitivity S was estimated to be

$$\Delta S \approx \cos^3(\gamma)\frac{D_{\text{eff,sens}}^2}{16r^2}$$

where γ is the angle between the pinhole aperture axis and the line connecting the source and the centre of the pinhole, r is the distance between the pinhole and the source as projected on the pinhole aperture axis and $D_{\text{eff,sens}}$ is the effective pinhole diameter in terms of sensitivity[23]. For small values of γ, the Metzler equation is very well approximated by the much simpler equation proposed in [24]:

$$D_{\text{eff,sens}} = \sqrt{D^2 + \tfrac{2}{\mu}\tan\left(\tfrac{\alpha}{2}\right)\cdot D + \tfrac{2}{\mu^2}\tan\left(\tfrac{\alpha}{2}\right)}\,.$$

Using this and the above equations, point source sensitivity S will be compared at matching system resolutions, and resolutions R_a and R_v will be compared at matching sensitivity in the results section.

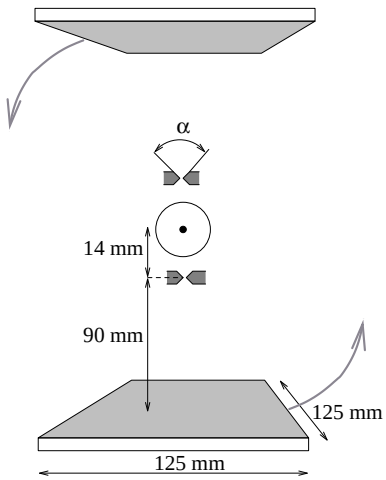

Figure 6: Schematic of dual pinhole SPECT system used for comparisons.

Simulations

Analytic simulations representing Tc-99m (140 keV) and I-125 (27–35 keV) imaging were performed with three different phantoms. Different isotopes were chosen in order to investigate how the image resolution is affected by the increased photon penetration that occurs with Tc-99m. Poisson noise was generated in the projection data. A mouse-brain phantom (figure 7) was derived from serial cryo-sections, in which the white and grey matter were segmented manually. Grey-to-white uptake ratio was assumed to be 5 to 1, in accordance with the Hoffman phantom [25]. The Defrise phantom consists of a set of discs filled with activity, which has been proved useful for investigating the effects of incomplete data that occur in cone-beam imaging geometries (note that ideal pinhole systems obey a cone beam geometry). Finally, we used a resolution phantom consisting of six sectors with rods of different diameters (0.25, 0.3, 0.4, 0.6, 0.8 and 1.0 mm), as shown in figure 8. The distance between the centre of adjacent rods was twice the rod diameter.

It was assumed that 10.4 MBq Tc-99m or 6.33 MBq I-125 was present in the entire mouse brain during a simulated scan with an acquisition time of 30 min. The gamma abundances differ per isotope. Here, the ratio between the Tc-99m and I-125 activities was chosen such that the number of gamma (plus x-ray photon emissions in case of I-125) from both isotope distributions were equal. In grey matter, the concentration was 41.42 kBq μl^{-1} for Tc-99m and 25.21 kBq μl^{-1} for I-125. The same concentration as in the grey matter was simulated in the active areas of the resolution phantom and the Defrise phantom.

The resolution-degrading effects of pinhole diameter and aperture penetration were accurately modelled during projection simulation [26]. The accuracy of the simulation was checked against analytical equations and Monte Carlo simulations [19,23]. The voxel size during simulation was 50 μm, which is two times smaller than the size used during image reconstruction. The smaller size was selected to emulate the fine resolution properties of real activity distributions.

In performing three-dimensional phantom simulations, we used pinhole diameters of 100, 200, 300 and 500 μm for U-SPECT-III and 400, 600, 800 and 1200 μm for dual pinhole SPECT. Different pinholes size ranges were chosen for U-SPECT-III and dual pinhole SPECT, since both systems have very different sensitivities.

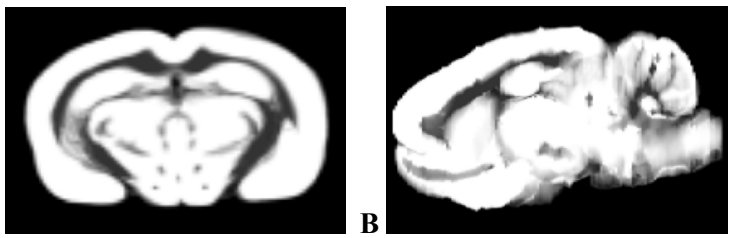

Figure7: Slices (0.4 mm thickness) of the mouse-brain phantom. (A)trans-axial slice (brain width is ≈9 mm). (B) sagittal slice.

Figure 8: Cylindrical cold rod phantom with rod diameters of 0.25, 0.3, 0.4, 0.6, 0.8 and 1.0 mm.

Image reconstruction

Image reconstruction for both U-SPECT-III and the dual pinhole SPECT was performed using ordered subset estimation maximization [28]. Relevant matrix elements (non-zero) were pre-calculated using analytic simulation of point source responses, and were stored on disc lexicographically. The effects of collimator blurring (including effects of pinhole diameter and penetration) and intrinsic detector blurring are accurately represented in the matrix elements and were calculated using ray tracing methods according to the equations contained in [26]. The voxel size during reconstruction was 100 μm.

Dual pinhole system

The geometry of the DP-SPECT that was used for comparing with that of U-SPECT-III is shown in figure 6. The focal length is 90 mm, and the distance between the centre of rotation and the pinhole is 14 mm, which represents a circular orbit that fits tightly around the mouse head. The opening α of the pinhole was 90°, which is just sufficient to avoid truncation of the projections at the detector corners. It was assumed that detector was pixelated (2.2 mm × 2.2 mm pixels), and a crystal with 71 % chance of gamma detection for Tc-99m. The probability of 71 % is based on 6 mm thick NaI with 10 % detection loss due to crystal gaps. The same detection probabilities were assumed for U-SPECT-III and for all I-125 simulations. The dual pinhole system parameters simulated closely resembles those of a system described in [7], but with some improvements implemented that comprises gold pinholes apertures and advanced ML-EM reconstruction with accurate resolution recovery.

Results

The system sensitivity and the system resolution of U-SPECT-III and DP-SPECT for a range of pinhole diameters are listed in table 1. Figure 9 shows that sensitivity, at matching resolution in the central FOV, is ≈15–30 times higher with U-SPECT-III than with DP-SPECT. These graphs also show that with U-SPECT-III, the spatial system resolution can be almost four times higher and volumetric resolution about 60 times higher than with DP-SPECT, when the systems are compared at matching sensitivity.

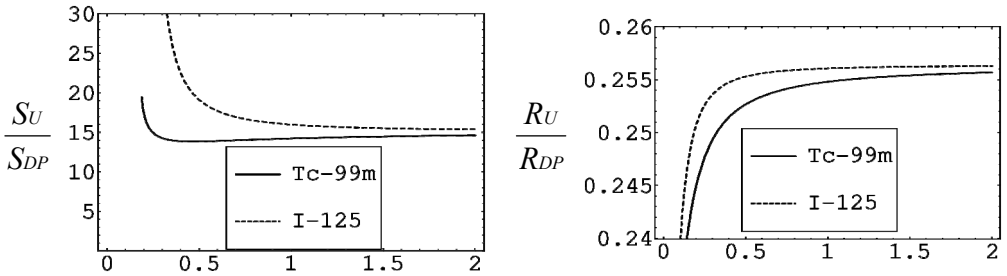

Figure 9: (A) ratio between sensitivity of U-SPECT-III and dual pinhole SPECT, calculated at equal average resolution R_a, as a function of the pinhole diameter of U-SPECT-III. (B) ratio between average resolution R_a of U-SPECT-III and dual pinhole SPECT, calculated at equal sensitivity S, as a function of the pinhole diameter of U-SPECT-III.

System	U-SPECT-III					Dual pinhole SPECT				
diameter (μm)	100	200	300	400	500	400	600	800	1200	2000
R_a Tc (μm)	220	358	498	639	780	754	966	1185	1632	2542
R_a I(μm)	160	295	434	575	716	586	786	999	1442	2349
R_v Tc (μL)	0.0107	0.0460	0.1236	0.261	0.474	0.429	0.901	1.662	4.349	16.43
R_v I(μL)	0.0041	0.0257	0.0820	0.190	0.366	0.201	0.485	0.996	2.995	12.96
S Tc (%)	0.0356	0.0816	0.1483	0.236	0.344	0.0232	0.0371	0.0546	0.100	0.235
S I (%)	0.0116	0.0439	0.0970	0.171	0.266	0.0080	0.0175	0.0305	0.0695	0.185

Table 1: Linear system resolutions (R_a), volumetric system resolution (R_v) and Sensitivity (S) for U-SPECT-III and dual pinhole SPECT, for various pinhole diameters.

SPECT phantom simulations

Results of pinhole diameters of 100, 200, 300 and 500 μm for U-SPECT-III and 400, 600, 800, and 1200 μm for dual pinhole SPECT are shown in this subsection for two different phantoms in figures 10 and 11. The images are shown at the iteration

that has the minimum difference with the digital phantom (in terms of mean squared error) that was reached during the iteration process. A problem when using small pinholes is that a higher fraction of radiation penetrates the aperture edges. To investigate the effects, we performed simulations of U-SPECT-III not only with I-125, but also with Tc-99m.

Figure 10 shows reconstructions of the resolution phantom. U-SPECT-III produces superior image quality. Cold rods with a diameter of 0.3 mm are resolved with U-SPECT-III, whereas with dual pinhole SPECT the rods with a diameter of 0.8 mm are the smallest that are clearly resolved. There is only a small difference between Tc-99m and I-125 simulations; the Tc-99m images are slightly smoother, because (i) an increased number of photons are detected due to penetration of the pinhole aperture and (ii) more blurring occurs due to increased edge penetration.

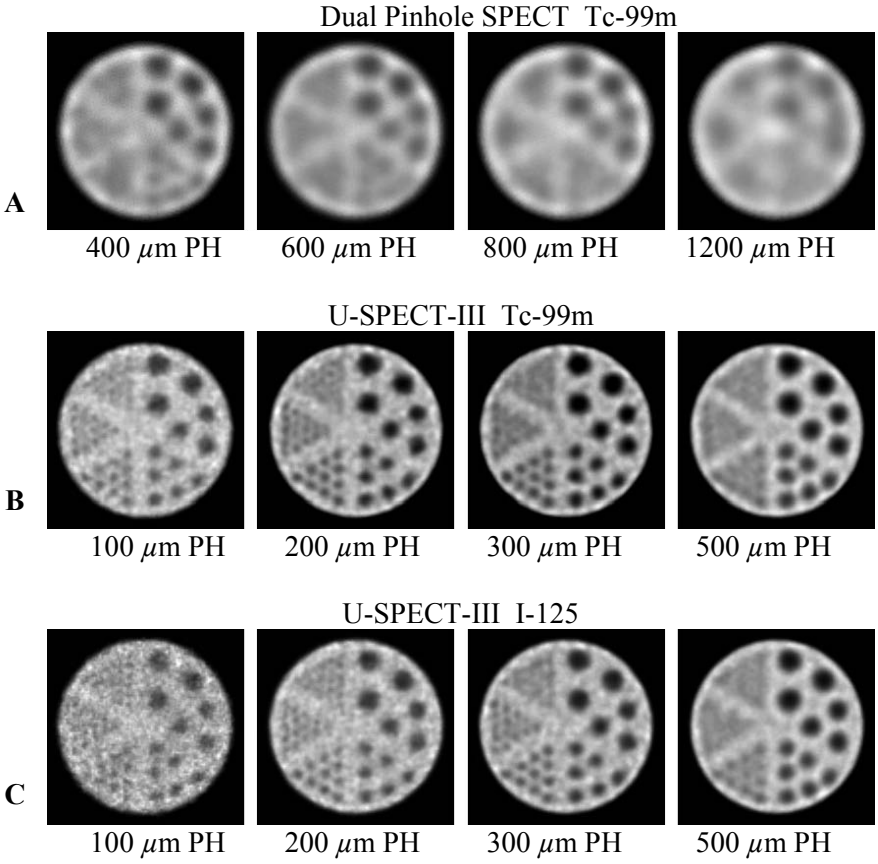

Figure 10: Simulated images of the resolution phantom (0.25, 0.3, 0.4, 0.6, 0.8 and 1.0 mm diameter rods). (A) dual pinhole SPECT with 400, 600, 800 and 1200 μm pinholes and Tc-99m. (B) U-SPECT-III system with 100, 200, 300 and 500 μm pinholes and Tc-99m. (C) U-SPECT-III with I-125.

Figure 11 shows reconstructions of the mouse-brain phantom. Images of simulated U-SPECT-III are compared with simulated DP-SPECT. Several details that are not visible with DP-SPECT are clearly visible in U-SPECT-III images. Furthermore, the shape of the brain is more severely distorted with DP-SPECT than with U-SPECT-III. The effects of photon penetration in the brain phantom that can be seen when Tc-99m is imaged instead of I-125 are similar to those visible in the resolution phantom.

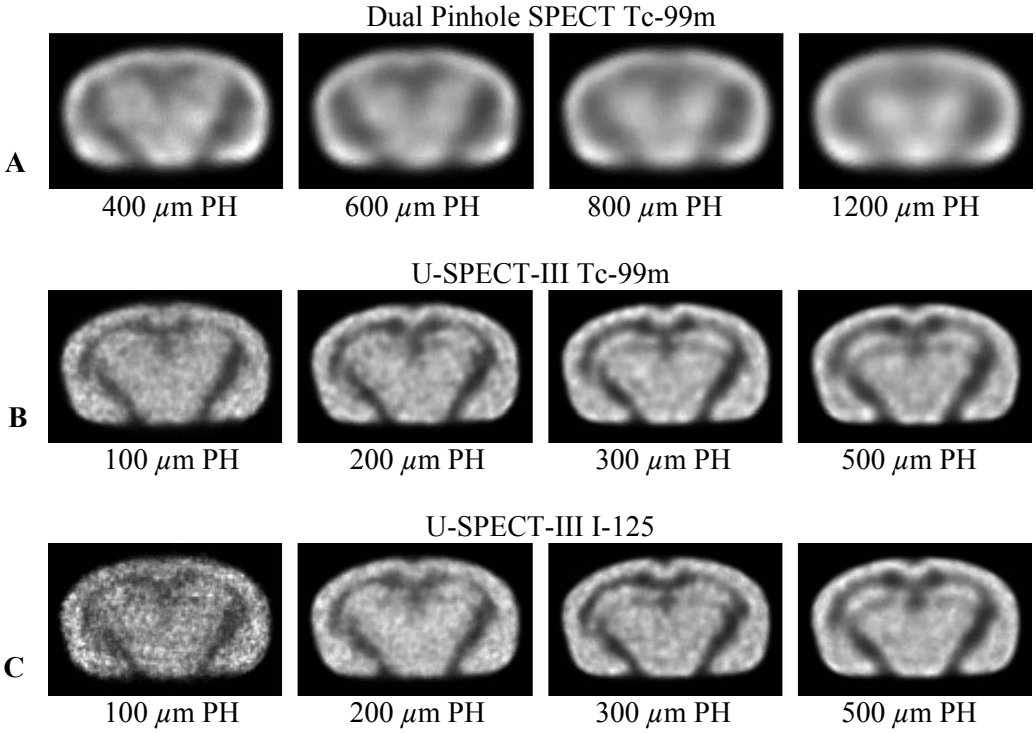

Figure 11: Simulated images of mouse-brain phantom. (A) dual pinhole SPECT, Tc-99m. (B) U-SPECT-III system, Tc-99m. (C) U-SPECT-III system, I-125.

Figure 12 shows the effects of different degrees of data-incompleteness in both systems. Dual pinhole SPECT suffers significantly more from this problem than U-SPECT-III does. This means that the superior resolution of U-SPECT-III that is shown in figures 10 and 11 is combined with a significantly larger object area which can be sampled adequately.

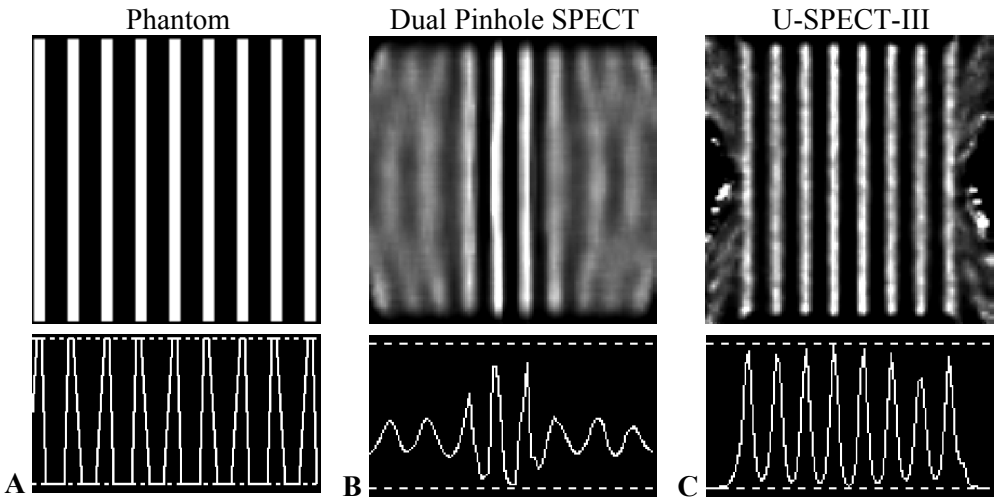

Figure 12: Reconstructions (sagittal slices) and image profiles of the Defrise disc phantom. (A) phantom. (B) dual pinhole SPECT. (C) U-SPECT-III image.

Conclusion and Discussion

In this chapter, we have proposed a new design for a high-resolution and high-sensitivity molecular imaging device (U-SPECT-III), and have simulated a number of outcomes. The U-SPECT series have a new type of pinhole geometry with non-overlapping projection views. This enables one to better estimate Orlov conditions for adequate sampling of data and to achieve better results than with conventional pinhole SPECT. The U-SPECT geometry produces excellent reconstructed images beyond the central plane of the scanner. Furthermore, the design allows for stationary data acquisition; this will make it easier to perform dynamic studies, will reduce maintenance requirements and may simplify system calibration. The proposed detector with focused columnar crystals is expected to prevent the blurring that can arise as a result of interactions taking place at different depths in the crystal.

The focusing of the pinholes of U-SPECT-III on a small cylindrical area of about 1cc leads to a very high sensitivity. The part of the field-of-view with the extremely high sensitivity is sufficiently large to cover important areas of interest such as the entire fore-and mid-brain, the kidneys or the heart of a mouse. We have shown here, and also in physical experiments with the U-SPECT-I system, that this set-up results in a very high-image resolution. It is also possible to extend the field-of-view without changing the pinhole geometry: the bed then needs to be moved to a few different positions, so that the area with highest sensitivity scans through the volume-of-interest in the animal. Previously, we have presented and validated a combined reconstruction and acquisition strategy that simultaneously takes into account all

projection data from different bed positions and therefore yields good reconstruction over an extended image volume [9]. Using this method, it should be possible to extend the images to complete transaxial slices of the mid-brain of a rat (approx. 16 mm diameter) using two or three different bed positions, with the presented U-SPECT geometry. Bed positions can be alternated sufficiently rapidly for dynamic studies to be performed flexible and satisfactorily. Of course the extension of the FOV will lead to reduction of the ultra-high sensitivity that can be obtained in a small area with the 'single bed position acquisition mode'.

The U-SPECT design presented requires to focus the crystals differently for each ring of pinholes that has a different tilt. This can make production more expensive. Therefore, entire units in different rings may be differently tilted in the final design. However, this has the drawback that close packing of the units will become more difficult.

For both U-SPECT-III and dual pinhole SPECT, a detection probability of 71 % was assumed for I-125 as well as Tc-99m gamma quanta. Seventy-one per cent is the interaction probability in 6 mm thick NaI crystals at 140 keV. For I-125 this interaction change is higher, but the probability of detection may not be higher due to limited light emission. In particular for Tc-99m, the assumed 71 % interaction probability may be an optimistic assumption for the case of U-SPECT-III, since long needles for putting together columnar crystals are currently hard to produce. If only those CsI needles with lengths that are currently readily available (up to about 2 mm) can be used, the sensitivity of U-SPECT-III may drop by 30–40 % due to reduced chance of interaction.

Another assumption that was made for U-SPECT-III calculations is an intrinsic detector resolution of about 150 μm, which was modeled by Gaussian blurring prior to detector binning. This is slightly worse than the measured intrinsic resolution of 120 μm with 1 mm columnar crystals. The lower resolution compared to measured resolution was taken because (i) longer crystals needles may suffer from more cross talk of scintillation light between columns and (ii) the columns will generally be mounted under an angle with respect to the CCD surface. In addition, due to current computer memory limitations, the smallest pixel size that could be used was 150 μm. This results in an additional degradation of intrinsic resolution that causes further reduction of performance of the simulated U-SPECT-III system compared to what may be possible in the near future. Another factor that can influence resolution is Compton interaction in the crystal, causing light flashes in different columns from a single gamma emission. Using Monte Carlo simulations we found that Compton scattering does not result in significant broadening of the FWHM of the point spread response. An intrinsic spatial image resolution of ≈120 μm FWHM was obtained [21].

At which pace systems like those presented in this chapter can be realized depends very much on costs and the availability of high-resolution detectors and dedicated crystals. Therefore, we go step by step, which has already started with the

recently launched U-SPECT-I system that produced its first *in vivo* small animal images at a resolution below 0.5 mm [9].

Like U-SPECT-III, this system has a focusing pinhole geometry, but is still based on conventional clinical NaI detectors and 75 gold pinholes. The successor, U-SPECT-II, is currently under construction and is based on somewhat more conventional detectors than those that we expect to use in U-SPECT-III. In any case we hope that the simulation studies and ideas presented in this chapter will lead to further improvements over the current state-of-the-art of animal and clinical SPECT imaging.

Acknowledgements

This work was sponsored by the Medical Council of Netherlands Organization for Scientific Research, grant 917.36.335. We are grateful to Gerralt de Vree and Frans van der Have for technical assistance and fruitful discussions.

References

[1] Jaszczak RJ, Li J, Wang H, Zalutsky MR and Coleman RE, 'Pinhole collimation for ultra-high-resolution small-field-of-view SPECT', *Phys. Med. Biol.* 1994; 39: 425–437.

[2] Ishizu K, Mukai T, Yonekura Y, Pagani M, Fujita T, Tamaki N, Shibasaki H and Konishi J, 'Ultra-high-resolution SPECT system using four pinhole collimators for small animal studies', *J. Nucl. Med.* 1995; 26: 2282–2289.

[3] Weber DA and Ivanovic M, 'Ultra-high-resolution imaging of small animals: implications for preclinical and research studies', *J. Nucl. Cardiol.* 1999; 6: 332–344.

[4] Wu MC, Tang HR, Gao DW, Ido A, O'Connell JW, Hasegawa BH and Dae MW, 'ECG gated pinhole SPECT in mice with millimeter resolution', *IEEE Trans. Nucl. Sci.* 2000; 47: 1218–1227.

[5] Meikle SR, Fulton RR, Eberl S, Dahlbom M, Wong KP and Fulham MJ, 'An investigation of coded aperture imaging for small animal SPECT', *IEEE Trans. Nucl. Sci.* 2001; 48: 816–821.

[6] Habraken JBA, de Bruin K, Shehata M, Booij J, Bennink R, van Eck Smit BL and Sokole EB, 'Evaluation of high-resolution pinhole SPECT using a small rotating animal', *J. Nucl. Med.* 2001; 42: 1863–1869.

[7] McElroy D P, MacDonald L R, Beekman F J, Wang Y, Patt B E, Iwanczyk J S, Tsui B M W and Hoffman E J, 'Performance evaluation of A-SPECT: a high

resolution desktop pinhole SPECT system for imaging small animals', *IEEE Trans. Nucl. Sci.* 2002; 49: 2139–2147.

[8] Acton PD, Choi SR, Plossl K and Kung HF, 'Quantification of dopamine transporters in the mouse brain using ultra-high resolution single-photon emission tomography', *Eur. J. Nucl. Med. Mol. Imaging.* 2002; 29: 691–699.

[9] Beekman FJ, Vastenhouw B and van der Have F, 'Towards 3D nuclear microscopy using locally focusing many-pinhole SPECT', *Proceedings of the 2003 International Meeting on Fully Three-Dimensional Image Reconstruction in Radiology and Nuclear Medicine*, 2004.

[10] Chatziioannou A, 'Molecular imaging of small animals with dedicated PET tomographs', *Eur. J. Nucl. Med. Mol. Imaging.* 2002; 29: 98–114.

[11] King MA, Pretorius PH, Farncombe T and Beekman FJ, 'Introduction to the physics of molecular imaging with radioactive tracers in small animals', *J. Cell. Biochem. Suppl.* 2002; 39: 221–230.

[12] Beekman FJ, McElroy DP, Berger F, Gambhir SS, Hoffman EJ and Cherry SR, 'Towards in vivo nuclear microscopy: I-125 imaging in mice using micro-pinholes', *Eur. J. Nucl. Med. Mol. Imaging.* 2002; 29: 933–938.

[13] Liu Z, Kastis GA, Stevenson GD, Barrett HH, Furenlid LR, Kupinski MA, Patton DD and Wilson DW, 'Quantitative analysis of acute myocardial infarct in rat hearts with ischemia-reperfusion using a high-resolution stationary SPECT system', *J. Nucl. Med.* 2002; 43: 474–480.

[14] Rowe RK, Aarsvold JN, Barrett HH, Chen JC, Klein WP, Moore BA, Pang IW, Patton DD and White TA, 'A stationary hemispherical SPECT imager for three-dimensional brain imaging', *J. Nucl. Med.* 1993; 34: 474–480.

[15] Beekman FJ and Vastenhouw B, 'Design and simulation of U-SPECT, an ultra-high resolution molecular imaging system', *IEEE Nucl. Sci. Symp. Conf. Record (Norfolk,VA)* 2002; 2: 792–796.

[16] He Z, Li W, Knoll GF, Wehe DK and Stahle CM, '3-D position sensitive CdZnTe gamma-ray spectrometers', *Nucl. Instrum. Methods* A. 1999; 422: 173–178.

[17] Beekman FJ, 'Fiber camera', *Patent application,* 2002, NL 102 1554. (September 2002)

[18] Beekman FJ, 'A method for obtaining a tomographic image, including an apparatus', *Patent application,* 2002, PCT/NL02/00303. (8 May 2002)

[19] van der Have F and Beekman FJ, 'Photon penetration and scatter in micro-pinhole imaging: a Monte Carlo investigation', *Phys. Med. Biol.* 2004; 49: 1369–1386.

[20] Nagarkar VV, Gordon JS, Vasile S, Gothoskar P and Hopkins F, 'High resolution x-ray sensor for non destructive evaluation', *IEEE Trans. Nucl. Sci.* 1996; 43: 1559–1563.

[21] de Vree GA, Westra AH, Moody I, van der Have F, Ligtvoet C M and Beekman F J, 'Electronics for a photon counting gamma camera based on an electron-multiplying CCD', *IEEE Trans. Nucl. Sci.* 2005; 52:580-588.

[22] Accorsi R and Metzler SD, 'Analytic determination of the resolution-equivalent effective diameter of a pinhole collimator', *IEEE Trans. Med. Imaging.* 2004; 23: 750–763.

[23] Metzler SD, Bowsher JE, Smith MF and Jaszczak RJ, 'Analytic determination of pinhole collimator sensitivity with penetration', *IEEE Trans. Med. Imaging.* 2001; 20: 730–741.

[24] Paix D, 'Pinhole imaging of gamma rays', *Phys. Med. Biol.* 1967; 12: 489–500.

[25] Hoffman EJ, Cutler PD, Digby WM and Maziotta JC, '3D-phantom to simulate cerebral bloodflow and metabolic images for PET', *IEEE Trans. Nucl. Sci.* 1990; 37: 616–620.

[26] Gieles M, de Jong HWAM and Beekman FJ, 'Monte Carlo simulations of pinhole imaging accelerated by kernel-based forced detection', *Phys. Med. Biol.* 2002; 47: 1853–1867.

[27] Beekman FJ, Vastenhouw B, van der Have F, Hoekstra A and van Rijk PP, 'U-SPECT I: Sub-mm resolution small animal SPECT based on a triple detector gamma camera', *J. Nucl. Med.* 2004; 45: 97P.

[28] Hudson HM and Larkin RS, 'Accelerated image reconstruction using ordered subsets of projection data', *IEEE Trans. Med. Imaging.* 1994; 13: 601–609.

Chapter 9

Summary

The main subjects of this thesis are simulation, construction, development of a small-animal SPECT system called U-SPECT. With the U-SPECT it is possible to study the function of organs and tissue *in vivo* at sub-half millimeter scale using radioactively labeled tracers. Prior to the SPECT scan, the animal is injected with the tracer which is accumulated at the target location. The radioactive molecules emit gamma photons in all directions which have enough energy to escape the body. Gamma cameras are used to detect the photons emerging from the body and acquire a projection of the tracer distribution inside the animal. The resulting set of projection images are used to obtain a 3D volume of the tracer distribution inside the animal using tomographic image reconstruction techniques.

In **chapter 2**, the design and implementation of the first prototype U-SPECT-I is presented. This machine is based on a clinical SPECT system with three gamma cameras. A custom build collimator and shielding are used. The special design of the cylindrical collimator which contains 75 gold pinholes results in large magnification of the projection data, which is important to deal with limited gamma camera resolution. All pinholes are focused to a small field of view to obtain a high photon count yield from the organ under investigation. Since the pinholes surround the animal and simultaneously observe the animal from a large number of angles, there is no need to rotate the animal or the gamma cameras. The sensitivity and resolution of the system is investigated and the first mice studies are presented. Reconstructed images from a small resolution phantom show that sets of radioactively filled capillaries with a diameter of 0.5 mm are clearly separated. Images from the first *in vivo* mouse studies show tiny details of a mouse spine and myocardial perfusion in the left and right ventricular wall.

Image reconstruction is performed using an iterative reconstruction algorithm. For this type of reconstruction, a method to simulate the detector response for a known activity distribution is required, which is given by the system matrix. **Chapter 3** presents a method that was developed to obtain the system matrix, which is based on point source measurements. The detector response for a point source, called point spread function (PSF), is measured at a number of locations and the complete system matrix is constructed using interpolation. Reconstructed image resolutions of 0.45 mm with 0.6 mm pinholes and below 0.35 mm with 0.3 mm pinholes are obtained. When the PSFs are modelled more accurate, better reconstructed images are obtained. However, more accurate modelling also leads to a larger matrix and consequently image reconstruction takes more time. This trade-off between image quality and reconstruction times is investigated using capillary phantoms with different rod sizes. The influence of the acquisition time on the reconstructed image quality is studied and we show that it is still possible to achieve sub-mm resolution for sub-minute acquisition times using 0.6 mm pinholes.

The field of view of the U-SPECT-I is large enough for imaging most mouse organs like the heart, brain or kidneys. In **chapter 4** we present a combined acquisition and reconstruction strategy that allows a larger volume to be scanned, up-to full-body imaging. During acquisition, the animal is stepwise moved through the

focus of the pinholes using a motor-controlled XYZ stage, and projections from the entire animal are collected (Scanning Focus Method, SFM). A specially adapted iterative reconstruction method is used, which exploits all projections simultaneously to reconstruct the entire volume sampled. Simulations and phantom measurements show that the SFM provides a clear improvement over the method that involves stitching separate reconstructions of sub-volumes obtained from the different bed positions. Using phantoms and a mouse bone scan we demonstrate that the U-SPECT-I is capable of total-body mouse imaging with a resolution better than 0.5 mm.

The successor of the U-SPECT-I (U-SPECT-II) is presented in **chapter 5**. This system is based on the same fundamentals of the U-SPECT-I but is a stand alone system, specially designed for small animal imaging. Significant improvements over the first system include larger detectors, a lager field of view, list mode data processing, gating capabilities and a user friendly interface. Several collimators are available for both rats and mice with a variety of pinhole diameters ranging from 0.35 mm to 1.5 mm. The performance of this system is characterized with sensitivity measurements, resolution phantom scans and *in vivo* mouse and rat studies. The reconstructed resolutions (determined with Jaszczak capillary phantoms) are < 0.35 mm and 0.45 mm using the mouse collimators with 0.35 mm and 0.6 mm pinholes respectively and 0.8 mm resolution is obtained using the rat collimator with 1.0 mm pinholes. Phantom measurements show that the resolution with I-125 and In-111 is only slightly degraded compared to that of Tc-99m. *In vivo* cardiac, kidney, tumor, and bone images show that U-SPECT-II can be used for novel applications in the study of dynamic biological systems and (radio) pharmaceuticals at the sub-organ level. U-SPECT-II is a versatile imaging system capable of high resolution imaging of rats and mice using dedicated collimators and associated animal beds. A user friendly interface allows easy selection of volume of interest from single organ to total body scanning.

Focusing pinhole SPECT systems like the U-SPECT are capable of reaching high resolutions and high sensitivity. A potential problem with these systems is that the field-of-view is often small, which makes it difficult to define the volume-of-interest (VOI) to be scanned. In **chapter 6**, a new tool is proposed to optimize the definition of the VOI. This tool is developed for the U-SPECT-II system and is based on a combination of dedicated hardware (optical cameras) and special software. Prior to the SPECT acquisition, the bed is positioned in front of the collimator where three webcams acquire optical images of the animal from the left, right and top. The boundaries of the volume to be scanned can be marked on these images by rectangles in all directions in order to define a box. Next, a sequence of bed translations is calculated such that the focus of the pinholes scans only within this box. The ability to select a scan volume which fits tight around the organ of interest makes it possible to maximize the number of counts from the organ, which results in better resolution and lower noise. Images from resolution phantom scans as well as a mouse heart study show that accurate selection of the VOI significantly improves image quality. Moreover, a sensitivity increase of approximately 250 % was obtained by using a

highly focused scan volume in all directions instead of a non focused scan volume. Accuracy measurements show that the correspondence between the optical images and the reconstructed image is below 0.5 mm. We conclude that the combination of focused scanning with optical guided VOI selection enables accurate positioning and high resolution imaging which is vital to use the full potential of highly focusing systems.

The static design, high resolution and high sensitivity of the U-SPECT systems are well suited for dynamic imaging. **Chapter 7** shows an application of this dynamic capability by imaging dopamine transporters (DAT) in the mouse brain during a range of points in time. A mouse is injected with FP-CIT, which is a radio actively labeled tracer which binds to the DAT. SPECT acquisitions of 45 seconds each were obtained, while cocaine was administered to washout the FP-CIT from the brain. From the reconstructed SPECT images, movies of the concentration of the DAT-ligand in the striatum were generated. Before administration of the cocaine the concentration FP-CIT in the striatum was stable. Thereafter, it rapidly declined, with about 50 % loss of DAT-binding at 28 minutes after cocaine injection. To demonstrate the feasibility of resolving FP-CIT binding in very small volumes of the brain a long SPECT acquisition is performed and compared to an *ex vivo* image obtained by autoradiography. We demonstrated that with the U-SPECT system, DAT imaging is possible with high resolution and sub-minute time frames in the mouse brain. We expect that this will aid the understanding of dynamic processes of this neurotransmitter that underlie brain functions and human brain pathology.

The U-SPECT-I and U-SPECT-II systems are equipped with large scintillation cameras which have a spatial resolution of a few millimeters. While high image resolution is obtained by strong magnification, we expect that significant improvements are possible by using high resolution detectors like CCD's (charge-coupled device). The design of U-SPECT-III is presented in **chapter 8**, which uses a set of high resolution detectors combined with a cylindrical collimator that contains 135 pinholes. A method for high-resolution scintillation detection is described, that eliminates the depth-of-interaction problem encountered with pinhole cameras. This approach, based on scintillation fibers pointed towards the pinholes, is expected to provide intrinsic detector resolutions better than 150 micron. The U-SPECT-III design was compared with a dual pinhole small animal SPECT system through simulation. Simulated images of a digital mouse-brain phantom show much more detail with U-SPECT-III than with dual pinhole SPECT. In a resolution phantom, 0.3 mm diameter cold rods are clearly visible with U-SPECT-III, whereas with dual pinhole SPECT the smallest visible rods are about 0.6-0.8 mm.

Samenvatting

In dit proefschrift worden de simulatie, constructie en toepassing van een *Single Photon Emission Computed Tomography* (SPECT) systeem voor kleine laboratorium dieren beschreven. Met dit SPECT systeem genaamd 'U-SPECT' is het mogelijk de functie van organen en weefsels te bestuderen op submillimeter schaal met behulp van radioactief gelabelde moleculen (tracers). Voorafgaand aan de SPECT scan, wordt het dier geïnjecteerd met een tracer die zich na enige tijd op een locatie verzameld die specifiek is voor de gebruikte tracer. De radioactieve moleculen vervallen waarbij gammafotonen worden uitgezonden in alle richtingen. Deze gammafotonen beschikken over voldoende energie om aan het lichaam te ontsnappen. Voor de detectie van de gammafotonen worden gammacamera's gebruikt waarbij de gammafotonen in een scintillatiekristal worden omgezet in zichtbaar licht. Dat zichtbare licht wordt versterkt in zogenaamde fotomultiplicatorbuizen en omgezet in elektrische signalen om zo een projectiebeeld van de gedetecteerde fotonen op de detector te verkrijgen. De opgenomen projectiebeelden worden gebruikt om met behulp van tomografische beeldreconstructie een driedimensionaal beeld (volume) van de tracer verdeling te berekenen. Zo kunnen we zien waar in het lichaam de tracer terecht komt.

In **hoofdstuk 2**, wordt het ontwerp en de constructie van het eerste prototype van de U-SPECT-I gepresenteerd. Deze machine is gebaseerd op een klinisch SPECT systeem, uitgerust met drie gammacamera's. Een speciaal ontworpen 'collimator' zorgt ervoor dat slechts een deel van de gamma fotonen worden doorgelaten naar de detector. De cilindervormige collimator bevat 75 gouden 'pinholes'. Dit zijn kleine gaatjes waar de straling door kan, vergelijkbaar met de vroegere *camera obscura* voor fotografie. Door de speciale geometrie van de collimator wordt de tracerverdeling sterk uitvergroot op de detectoren geprojecteerd, hetgeen een belangrijke factor is om te compenseren voor de beperkte resolutie van de gammacamera's. Alle pinholes zijn gericht op een klein gezichtsveld (field-of-view) in het midden van de collimator om een groot deel van de fotonen op te vangen die afkomstig zijn uit het orgaan dat onderzocht wordt. Aangezien het dier door de verschillende pinholes gelijktijdig onder een groot aantal hoeken wordt geobserveerd, is het niet nodig om het dier of de gammacamera's te draaien tijdens het scannen. De gevoeligheid en de resolutie van het systeem is onderzocht en de eerste dierstudies worden in dit hoofdstuk gepresenteerd. Beelden van een mini resolutiefantoom, bestaande uit een verzameling radioactief gevulde capilairen met verschillende diameters, laten zien dat een resolutie van <0,5 mm haalbaar is. De studies met muizen tonen piepkleine details in de wervelkolom en de doorbloeding van het linker en rechter deel van de hartwand.

De beeldreconstructie wordt uitgevoerd volgens een iteratief algoritme. Voor dit type reconstructie is een methode nodig om het projectiebeeld op de detector te kunnen simuleren voor een bekende activiteitsverdeling. In deze stap wordt gebruik gemaakt van de zogenaamde 'systeem matrix', die het detector beeld beschrijft voor elke positie in het systeem. **Hoofdstuk 3** introduceert een methode die werd ontwikkeld om deze systeem matrix te construeren. De methode is gebaseerd op

metingen met een puntbron op een beperkt aantal locaties in het systeem. Aan de hand van de gemeten puntspreideingsfuncties (PSF's) wordt door middel van interpolatie de complete systeem matrix opgebouwd. Met deze methode worden beeldresoluties verkregen van 0,45 mm met 0,6 mm pinholes en minder dan 0,35 mm met 0,3 mm pinholes. Als de modellering van de PSF's nauwkeuriger wordt uitgevoerd resulteert dit in betere beelden. Een nauwkeurige modellering levert echter ook een grote systeem matrix op, waardoor de beeld reconstructie meer tijd in beslag neemt. De afweging tussen beeldkwaliteit en reconstructietijd is onderzocht met behulp van een mini resolutiefantoom. De invloed van de acquisitietijd op de gereconstrueerde beeldkwaliteit is ook bestudeerd en we laten zien dat het nog steeds mogelijk is om submillimeter resolutie te bereiken voor een acquisitie tijd minder dan 1 minuut met gebruik van 0,6 mm pinholes.

Het gezichtsveld van de U-SPECT-I is groot genoeg om de meeste organen van een muis te scannen zoals het hart, de hersenen of de nieren. In **hoofdstuk 4** presenteren we een nieuwe acquisitie en reconstructie strategie die het mogelijk maakt een groter volume te scannen (Scanning Focus Method, SFM). Zelfs het hele lichaam kan hierdoor gescand worden. Tijdens de scan wordt het dier stapsgewijs verplaatst door het gezichtsveld van de pinholes met behulp van een motor gestuurde XYZ robot. Een speciaal aangepaste iteratieve beeldreconstructie methode gebruikt alle projecties gelijktijdig voor het reconstrueren van het volledige gescande volume. Uit simulaties en fantoom metingen blijkt dat deze SFM een duidelijke verbetering is ten opzichte van de methode waarbij de deelvolumes van de verschillende bedposities apart worden gereconstrueerd en daarna samengevoegd. Met behulp van fantomen en een bot scan van een muis tonen wij aan dat de U-SPECT-I in staat is een hele muis te scannen met een resolutie beter dan 0,5 mm.

U-SPECT-II, de opvolger van de U-SPECT-I wordt gepresenteerd in **hoofdstuk 5**. Dit systeem is gebaseerd op dezelfde principes als de U-SPECT-I, maar is een systeem dat speciaal ontworpen is voor het scannen van kleine dieren. Belangrijke verbeteringen zijn grotere detectoren, een groter gezichtsveld en de dataverwerking op basis van *list mode* waarbij de data van elk gedetecteerde gamma foton apart wordt opgeslagen. Dit laatste maakt het mogelijk om tijdens de reconstructie verschillende energiewindows te gebruiken en zo meerdere isotopen tegelijkertijd op te nemen. De verschillende fasen van het kloppende hart of de ademhaling kunnen apart worden gereconstrueerd op basis van externe signalen. Er zijn verschillende collimatoren beschikbaar voor ratten en muizen met een verscheidenheid aan pinhole diameters variërend van 0,35 mm tot 1,5 mm. De prestaties van dit systeem worden gekenmerkt met gevoeligheidsmetingen, resolutiefantoom scans, muis- en ratstudies. De gereconstrueerde resoluties (bepaald met fantoom scans) zijn $< 0,35$ mm en 0,45 mm voor de muizencollimator met respectievelijk 0,35 mm en 0,6 mm pinholes. Voor de rattencollimator met 1,0 mm pinholes wordt een resolutie van 0,8 mm verkregen. Beelden van hart-, nier-, tumor-, en botscans tonen aan dat de U-SPECT-II kan worden gebruikt voor het bestuderen van dynamische biologische systemen op het niveau van deze organen en kleiner. U-

SPECT-II is een veelzijdig systeem om met hoge resolutie afbeeldingen te maken van ratten en muizen met behulp van speciaal ontwikkelde collimatoren.

Gefocusseerde pinhole SPECT systemen zoals de U-SPECT zijn in staat om hoge resoluties en hoge gevoeligheid te bereiken. Een potentieel probleem met deze systemen is dat het gezichtsveld vaak klein is, waardoor het moeilijk is om te bepalen welk volume er gescand moet worden. In **hoofdstuk 6** wordt een nieuwe methode voorgesteld om het te scannen volume te bepalen. Deze tool is ontwikkeld voor het U-SPECT-II systeem en is gebaseerd op een combinatie van speciale hardware (optische camera's) en software. Voorafgaand aan de SPECT scan worden er foto's van het dier gemaakt van links, rechts en boven. De grenzen van het volume dat moet worden gescand kan door de gebruiker worden aangegeven op deze beelden door het volume te markeren met rechthoeken. Vervolgens wordt een reeks bedposities berekend zodat enkel het gemarkeerde volume door het het gezichtsveld van de pinholes wordt bekeken. Door enkel het volume te scannen dat strak rond het orgaan past wordt het aantal opgevangen fotonen uit dit orgaan gemaximaliseerd, wat een betere resolutie en een lager ruisniveau oplevert. Beelden van resolutie fantomen en een muis hartstudie tonen aan dat nauwkeurige selectie van het orgaan de beeldkwaliteit aanzienlijk verbetert. Bovendien kan de gevoeligheid flink worden vergroot door het scanvolume strak om het orgaan te zetten. De afwijking tussen het geselecteerde volume op de foto's en het gereconstrueerde beeld is minder dan 0,5 mm. We concluderen dat de combinatie van een gefocusseerd systeem met een optisch volumeselectie een nauwkeurige positionering en een hoge resolutie SPECT scan mogelijk maakt. Deze eigenschappen zijn van belang om het volledige potentieel van sterk gefocuste systemen optimaal te benutten.

Het statische ontwerp, de hoge resolutie en hoge gevoeligheid van de U-SPECT systemen maakt deze zeer geschikt voor dynamische beeldvorming. **Hoofdstuk 7** geeft een toepassing van deze mogelijkheid door het in beeld brengen van dopamine transporters (DAT) in het brein van een muis op een groot aantal opeenvolgende tijdstippen. Een muis krijgt FP-CIT toegediend. Dat is een radioactief gelabelde tracer die bindt aan de DAT. Er is een serie SPECT acquisities gedaan van elk 45 seconden, terwijl na enige tijd cocaïne werd toegediend om de FP-CIT uit de hersenen te verdrijven (cocaïne bindt ook aan de DAT). Uit de gereconstrueerde SPECT beelden is een film gemaakt die de DAT concentratie in het striatum door de tijd laat zien. Vóór het toedienen van de cocaïne was de concentratie FP-CIT in het striatum stabiel. Daarna daalt deze snel, met als resultaat ongeveer 50 % verlies van de DAT-binding 28 minuten na injectie van de cocaïne. Een lange SPECT acquisitie toont aan dat de binding van het SPECT beeld vergelijkbaar is met een beeld verkregen door autoradiografie. Met het U-SPECT systeem is het mogelijk om de DAT in een muis in beeld te brengen met een hoge resolutie en een zeer korte scan tijd. We verwachten dat dit zal bijdragen aan de kennis van dynamische processen van deze neurotransmitter en de pathologie van de menselijke hersenen waarin deze en andere neurotransmitters een rol spelen.

De U-SPECT-I en U-SPECT-II systemen zijn uitgerust met grote gamma camera's met een intrinsieke resolutie van slechts enkele millimeters. Door gebruik te maken van een sterke vergroting wordt in de U-SPECT toch een hoge beeldresolutie verkregen. Wij verwachten echter dat er aanzienlijke verbeteringen mogelijk zijn door gebruik te maken van hoge resolutie detectoren op basis van bijvoorbeeld CCD's (charge coupled device). Het ontwerp van de U-SPECT-III wordt gepresenteerd in **hoofdstuk 8**, waarbij hoge-resolutie detectoren worden gecombineert met een cilindervormige collimator met 135 pinholes. Er wordt een methode voor een hoge resolutie scintillatie camera beschreven, waarmee het probleem van de variabele diepte van fotoninteracties in het kristal wordt weggenomen. Deze aanpak, gebaseerd op kleine naaldjes van scintillatie kristal die allemaal zijn gemonteerd in de richting van de pinhole, zal naar verwachting detectorresoluties beter dan 150 micron mogelijk maken. Het U-SPECT-III ontwerp wordt door middel van simulaties vergeleken met dieren-SPECT met twee pinholes. Beelden van een digitaal fantoom van een muizenbrein laten zien dat er veel meer detail met de U-SPECT-III gehaald kan worden dan met dual-pinhole SPECT. In een resolutiefantoom zijn 0,3 mm diameter capilairen duidelijk zichtbaar met de U-SPECT-III, terwijl met een 2-pinhole systeem 0,6 tot 0,8 mm de kleinste zichtbare zijn.

Dankwoord

Natuurlijk kon dit proefschrift niet tot stand komen zonder inzet en hulp van anderen. Een goede werksfeer, prettige collega's en de steun van vrienden en familie zijn voor mij zeer belangrijk geweest om mijn promotie tot een goed einde te brengen. Hier, in het meest gelezen deel van het boekje, sta ik stil om iedereen te bedanken die in de afgelopen jaren betrokken is geweest bij dit onderzoek.

Zeer veel dank ben ik verschuldigd aan prof. Freek Beekman. Ik ben bij jou begonnen als wetenschappelijk programmeur en de jaren zijn snel omgevlogen. Door het enthousiasme van de groep ben ik steeds verder bij het onderzoek betrokken geraakt. Ik heb de mogelijkheid die me werd geboden om zelf een proefschrift te gaan schrijven zeker aangenomen. Freek, jij hebt de aanzet voor dit proefschrift gegeven en zonder jou zou dit proefschrift waarschijnlijk nooit zijn verschenen. Je hebt een eindeloze hoeveelheid energie en je grote creativiteit levert vaak een stroom aan ideeën op. Ondanks dat je zeer druk bent, ben je altijd bereid tot snelle correcties van en aanvullingen op artikelen. Je bent altijd duidelijk aanwezig en deelt regelmatig hier en daar een duwtje uit om de zaken rond te krijgen.

Natuurlijk wil ik ook mijn andere promotor prof. Max Viergever bedanken voor de gelegenheid om te promoveren in de onderzoeksgroep van het ISI ondanks mijn ongebruikelijke manier waarop ik promovendus ben worden.

Frans, coauteur van veel stukken in dit boekje, je bent een toegewijde harde werker en goede collega. Ik ben je dankbaar voor een prettige samenwerking en ik heb vaak gebruik gemaakt van je gigantische hoeveelheid kennis. Als ik ergens niet uit kwam schudde jij de fysica moeiteloos uit je mouw. Bovendien ben je een prima kamergenoot met een eigenzinnige vorm van humor.

Uit onze groep wil ik verder Woutjan bedanken voor de vele uren intensief samenwerken (en ploeteren tot in de late uurtjes) om het geheel voor elkaar te krijgen. Ik wens je veel succes met het schrijven van papers voor je proefschrift. Ruud, bedankt voor je hulp tijdens het scannen (jij weet voor alles een praktische oplossing) en je goede gezelschap in Nice (succes met duiken). Norbert, je bent een 1000-poot die alles kan maken (onderdelen, tekeningen en foto's) en dat altijd met een brede glimlach. Zeker ook waardering voor de collega's van Milabs. Ik noem vooral Paul en Peggy voor een goede en ontspannen samenwerking. Jan, Marc en Marlies veel succes in Delft en ik hoop binnenkort weer met jullie samen te werken.

Natuurlijk ben ik ook m'n andere directe collega's en kamergenoten van de afgelopen jaren niet vergeten: o.a. Hugo, Auke-Pieter, Marcia, Renee, Mart (ik ben je nog 5 kilo paaseieren schuldig), Wojtek (how is live in the US?), Jianbin (get well soon!), Tim, Anne-marie, Matthieu, Mariëtte en Carmen. Allen bedankt voor de goede werksfeer, de vele momenten van rust en gezelligheid tijdens koffiepauzes,

lunches en conferenties. Steven, bedankt voor je altijd positieve bijdrage, (duvels) goede humor en natuurlijk ook vele nuttige discussies.

Medewerkers van het RMI bedankt voor de prima werkomgeving en de gezelligheid tijdens koffiepauzes, labdagen en de frequente borrels. Marten en Roger, dank voor het uitwisselen van Linux-wijsheid en goede samenwerking. Ook is het altijd mogelijk om onder genot van een kop dampende koffie samen het Windows systeem af te kraken! ☺

Alle collega's van het ISI zou ik willen bedanken voor de gezelligheid tijdens vele sociale activiteiten zoals de Ardennenweekenden, AZU-estafettes en de gezamenlijke lunches. In het bijzonder wil ik Thijs, Hans, Theo, Luuk, Everine, Shirley, Bram en Anna bedanken voor de sportiviteit en de vele rondjes langs de kromme rijn. Ook dit jaar is het weer gelukt een 'WASIESSIEOFISIESSIE' team samen te stellen voor deelname aan de Pheidippidesloop. Ik hoop dat we deze traditie nog lang vol zullen houden!

De medewerkers van de instrumentele dienst en mechanica wil ik bedanken voor de ondersteuning en hulp bij het maken van onderdelen en fantomen (o.a. Henk, Cees, Ruben). De elektronica- en labviewkennis van Bert heeft ons ook veel verder geholpen. Roy van de afdeling digitale fotografie is gelukkig altijd bereid om op het laatste moment nog wat posters uit te draaien voor een conferentie. Op de afdeling van nucleaire geneeskunde is altijd met veel interesse gekeken naar onze opstellingen en iedereen is altijd bereid om te helpen waar nodig. Allen bedankt!

Natuurlijk mijn beide paranimfen: Paul en Norbert bedankt dat jullie me willen bijstaan voor, tijdens en na mijn verdediging.

Ook woorden van dank voor de mensen die niet direct betrokken waren bij dit proefschrift, maar die zeker een andere belangrijke rol hebben gespeeld. Naast het werk in het UMC was er gelukkig af en toe tijd voor de nodige ontspanning met vrienden en familie. Met name Son, Elian, Leon, Adeline, Riza, Francisco en Mireille wil ik bedanken voor het uitstekende gezelschap tijdens veel weekendjes weg. We hebben genoten van lange wandelingen, gezellige etentjes, BBQ-avonden en ontelbare foto momenten. Bas, bedankt voor je jarenlange vriendschap (en het sloopwerk in ons nieuwe huis). Ik wil jou en Brenda veel geluk wensen met de komst van jullie kleine. Frank en Saskia, bedankt voor veel koppen koffie en natuurlijk de goede zorgen voor mijn viervoeters als ik weer eens niet thuis was.

Mijn familie en schoonfamilie bedank ik voor de belangstelling, betrokkenheid en steun van de afgelopen jaren. Door jullie hulp bij het opknappen en verhuizen hebben we in korte tijd veel werk verzet en van ons nieuwe huis een mooie plek gemaakt. Ik wil zeker ook mijn ouders hartelijk bedanken. Door jullie constante steun en liefde heb ik van een zorgeloze jeugd genoten en ook kon ik rekenen op jullie hulp en vertrouwen tijdens mijn studie en ver daarna!

Tot slot mijn Annemarie. Heel erg bedankt voor je enthousiasme, glimlach, vertrouwen, geduld en liefde. Ik kijk uit naar een mooie toekomst samen!

Brendan

Publications

International journals:

F.J. Beekman, A.P. Colijn, B. Vastenhouw, V.M. Wiegant and M.A.F.M. Gerrits, 'High-resolution emission tomography of small laboratory animals: physics and gamma-astronomy meet molecular biology', *Nucl. Inst. & Meth. A*. 2003; 509: 229-234.

T. Bokulić, B. Vastenhouw, H.W.A.M. de Jong, A.J. van Dongen, P.P. van Rijk and F.J. Beekman, 'Monte Carlo based Down-Scatter correction of SPECT attenuation maps', *Eur. J. Nucl. Med. Mol. Im.* 2004; 31: 1173-1181.

F.J. Beekman and B. Vastenhouw, 'Design and simulation of a high-resolution stationary SPECT system for small animals', *Phys. Med. Biol.* 2004; 49: 4579–4592.

F.J. Beekman, F. van der Have, B. Vastenhouw, A.J.A. van der Linden, P.P. van Rijk, J.P.H. Burbach and M.P. Smidt, 'U-SPECT-I: A novel system for submillimeter-resolution tomography with radiolabeled molecules in mice', *J. Nucl. Med.* 2005; 46: 1194–1200.

B. Vastenhouw and R.H. Bisseling, 'A two-dimensional data distribution method for parallel sparse matrix-vector multiplication', *Siam Review.* 2005; 47: 67-95.

B. Vastenhouw and F.J. Beekman, 'Submillimeter total-body murine imaging with U-SPECT-I', *J. Nucl. Med.* 2007; 48: 487-493.

B. Vastenhouw, F. van der Have, A.J.A. van der Linden, L. von Oerthel, J. Booij, J.P.H. Burbach, M.P. Smidt and F.J. Beekman, 'Movies of dopamine transporter occupancy with ultra-high resolution focusing pinhole SPECT', *Mol. Psych.* 2007; 12: 984-987.

F. van der Have, B. Vastenhouw, M. Rentmeester and F.J. Beekman, 'System calibration and statistical image reconstruction for ultra-high resolution stationary pinhole SPECT', *IEEE Trans. Med. Im.* 2008; 27: 960-971.

F. Van der Have, B. Vastenhouw, R. M. Ramakers, W.J. Branderhorst, J.O. Krah, C. Ji, S.G. Staelens and F.J. Beekman, 'U-SPECT-II: an ultra-high resolution device for molecular small-animal imaging', in revision.

B. Vastenhouw, W.J. Branderhorst, F. van der Have, M. Baiker and F.J. Beekman, 'Field-of-view definition for focusing pinhole SPECT using optical cameras', in preparation.

Conference proceedings:

F.J. Beekman and B. Vastenhouw, 'Design and simulation of U-SPECT, an ultra-high resolution molecular imaging system', *Conference proceeding of 2002 IEEE Nuclear Science Symposium and Medical Imaging Conference, Norfolk, USA*, 2002; 2: 792-796.

B. Vastenhouw, H.W.A.M. de Jong, P.P. van Rijk and F.J. Beekman, 'Monte Carlo based down-scatter correction of SPECT attenuation maps', *Conference proceeding of 2002 IEEE Nuclear Science Symposium and Medical Imaging Conference, Norfolk, USA*, 2002.

F. J. Beekman, B. Vastenhouw and F. van der Have, 'Towards 3D Nuclear Microscopy using locally focusing many-pinhole SPECT', *Proceedings of the 2003 International Meeting on Fully Three-Dimensional Image Reconstruction in Radiology and Nuclear Medicine*, 2004.

F. van der Have, B. Vastenhouw, M.C.M. Rentmeester and F. J. Beekman, 'System Calibration and Statistical Image Reconstruction for Sub-mm Stationary Pinhole SPECT', *Conference Record of the IEEE 2005 Nuclear Science Symposium and Medical Imaging Conference, Puerto Rico*, 2005: M11-291.

Curriculum Vitae

Brendan Vastenhouw werd geboren op 28 februari 1974 te Zaanstad. Hij verhuisde in zijn jeugd naar Alkmaar waar hij in 1992 zijn HAVO diploma behaalde aan het Jan van Scorel College. Na twee jaar gevolgd door een VWO diploma waarna hij begon aan de studie Computational Science aan de Universiteit van Utrecht. Tijdens zijn afstudeeronderzoek onder leiding van Rob Bisseling ontwikkelde hij een zoekmachine gebaseerd op 'Latent Semantic Indexing' waarbij een parallelle supercomputer werd ingezet om relaties tussen woorden te vinden in een verzameling documenten. Hierna publiceerden zij samen een artikel over een nieuwe methode om het werk over de verschillende processoren van de computer te verdelen. In 2001 begon hij in het Universitair Medisch Centrum Utrecht als wetenschappelijk programmeur bij het Image Sciences Institute in de groep van Freek Beekman. Daar werkte hij aan simulaties en de ontwikkeling van het U-SPECT systeem. Tijdens deze periode werd hij steeds meer betrokken bij het onderzoek en begin 2007 besloot hij een promotieonderzoek te starten. Hij kreeg hiertoe de mogelijkheid door zijn baan vier dagen aan te houden en daarnaast deeltijd promovendus te worden. De resultaten van het onderzoek staan beschreven in dit proefschrift.

Appendix: Color figures

Chapter 1

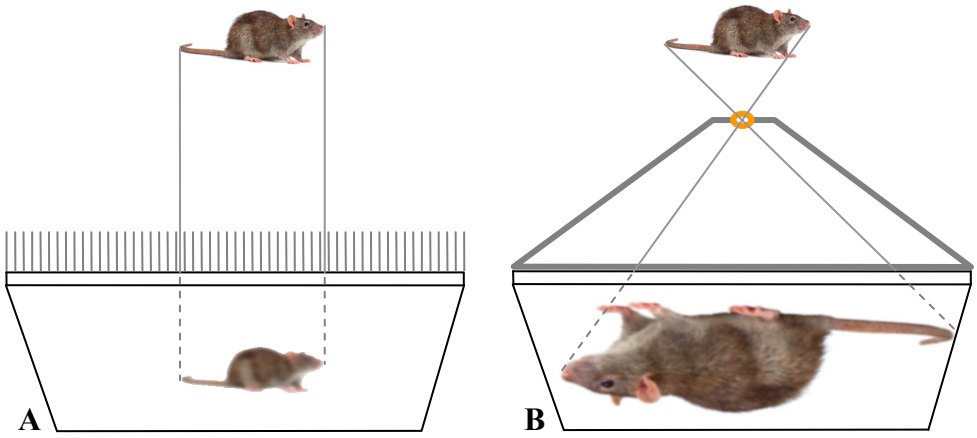

Figure 1: (A) parallel-hole projection. (B) pinhole-projection.

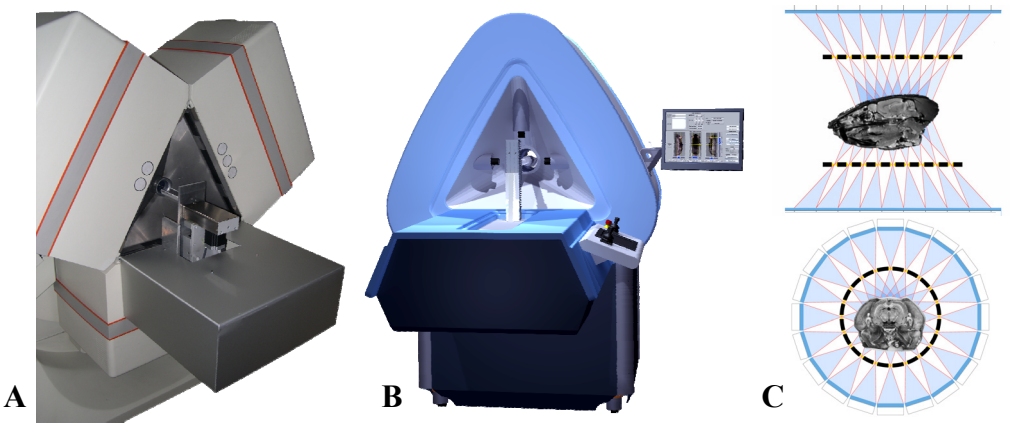

Figure 2: (**A**) U-SPECT-I (**B**) U-SPECT-II (**C**) cross sections through the U-SPECT-III geometry.

Chapter 2

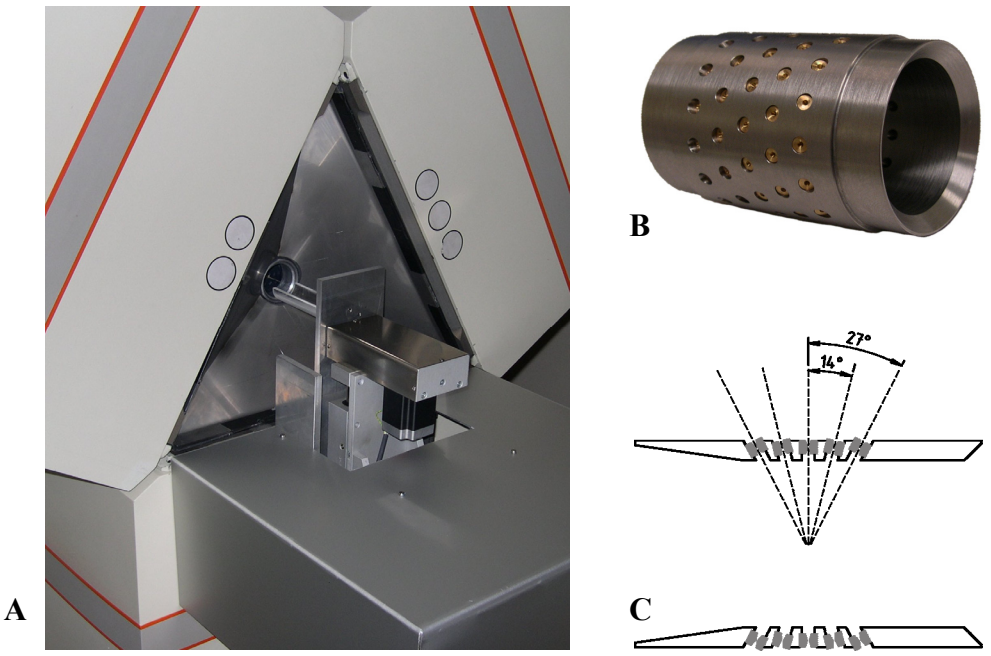

Figure 1: (A) overview of the U-SPECT-I system. Triangular shaped lead shielding is placed in between the camera heads of the triple detector system, the tungsten cylinder containing pinholes being placed in the center of the three detectors. The XYZ-stage with attached bed, placed in front of the lower detector, is also visible. (B) Cylinder with 75 gold pinhole apertures focused on the center of the cylinder. (C) Cross-section of cylinder with tilted pinholes.

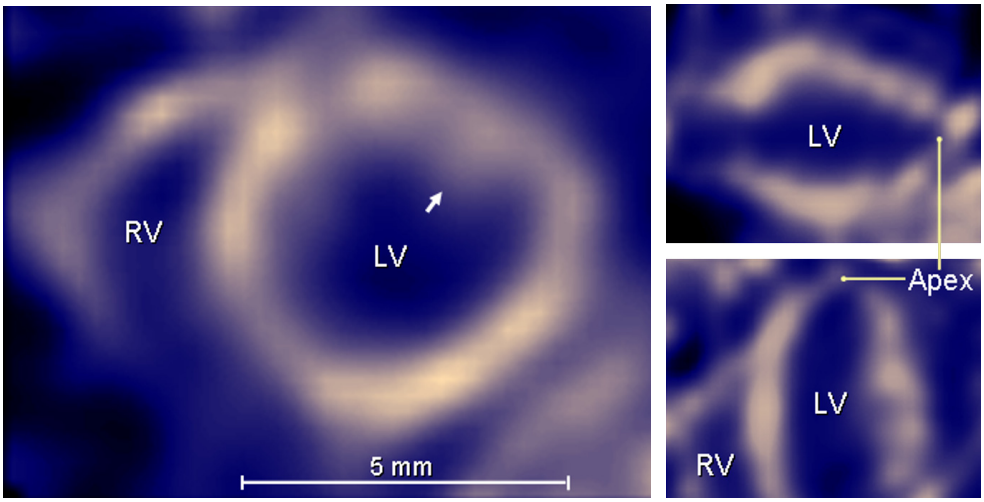

Figure 5: Mutual perpendicular cross sections through a sub-mm resolution 3D myocardial perfusion image volume of the living mouse (Animal co-image of the year, Society of Nuclear Medicine, Philadelphia 2004). Image data was acquired during 30 minutes, starting 30 min after administration of 222 MBq (6 mCi) Tc-99m-tetrofosmin. Left frame: short-axis slice shows myocardial perfusion in the right ventricular (RV) and left ventricular (LV) wall. Perfusion in the anterior papillary muscle (arrow) can be distinguished from the other parts of the left ventricular wall. Top right: vertical long-axis slice. Bottom right: horizontal long-axis slice.

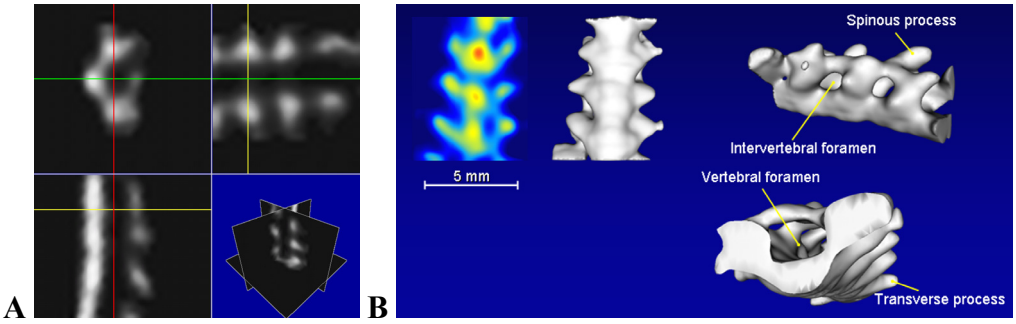

Figure 6: Different representations of a reconstructed image volume of the lumbar spine, acquired during 22 minutes, two hours after the injection of 148 MBq (4 mCi) Tc-99m-HDP. Frame (A) shows three different orthogonal cross-sections. In Frame (B) both a projection of local image maxima (upper left) and three iso-surface renderings of tracer concentrations in the same spinal section are displayed (Animal co-image of the year, Society of Nuclear Medicine, Philadelphia 2004).

Chapter 5

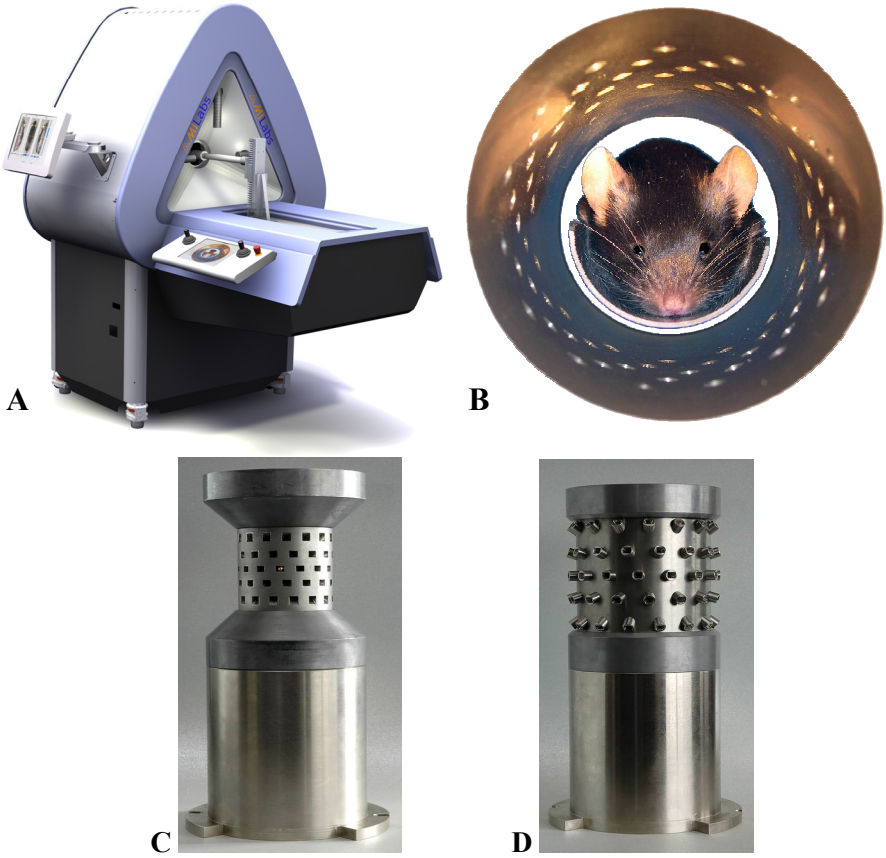

Figure 1: (A) U-SPECT-II system. (B) Collimator tube with mouse. (C) Mouse collimator and shielding tube. (D) Rat collimator and shielding tube.

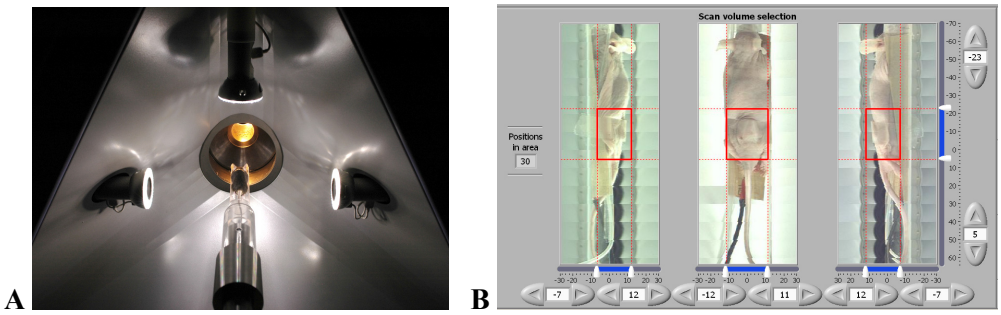

Figure 3: (A) Mouse observed with three optical cameras for region-of-interest selection. (B) User interface allows for selecting the region-of-interest that will be

scanned. In this case the region of interest is a tumor of which images are shown in figure 12.

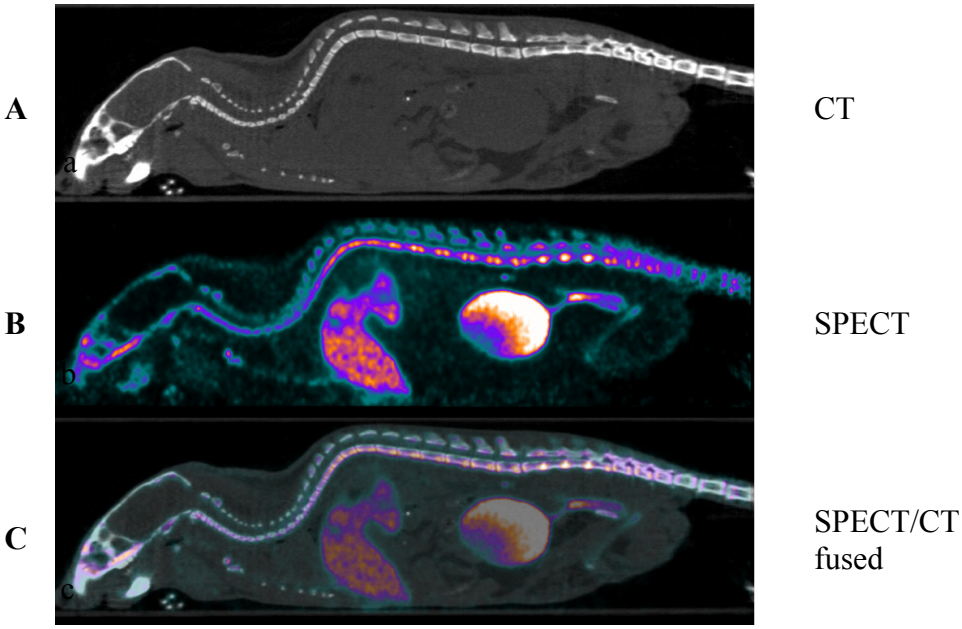

Figure 8: SPECT-CT saggital images of a mouse: (A) CT only (B) SPECT bone scan obtained with ^{99m}Tc-HDP on the U-SPECT-II system (C) fused SPECT/CT image. Registration was done by the method of Chow et al [37].

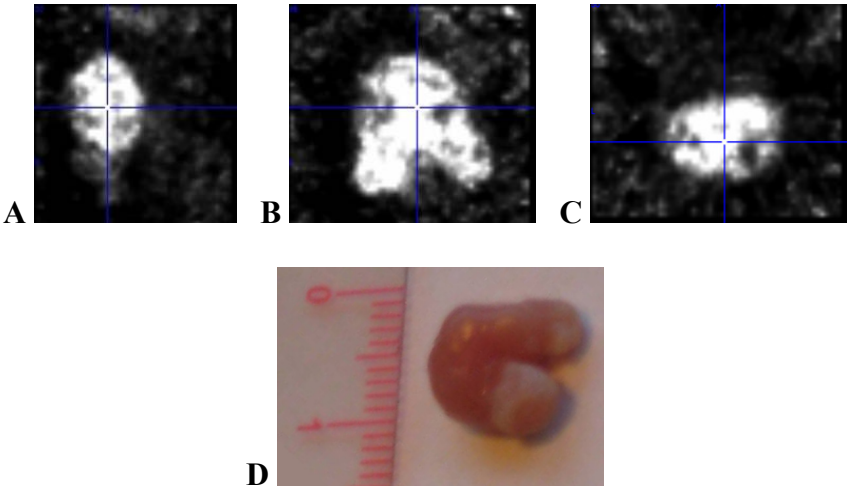

Figure 12: In-111-DTPA-14C5 mouse study (A), (B), and (C) three views of the reconstructed data. (D) photograph of the tumor.

Chapter 6

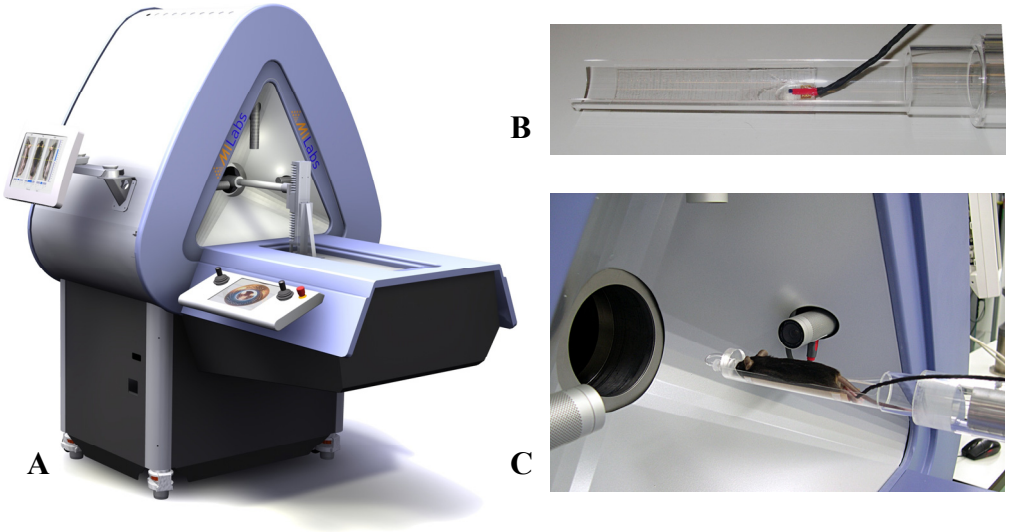

Figure 1: (A) The U-SPECT-II system showing the optical cameras at the front of the scanner, the XYZ stage and the control panels. (B) Animal bed with transparent heater pad. (C) Close-up of a mouse on the bed in front of the optical cameras.

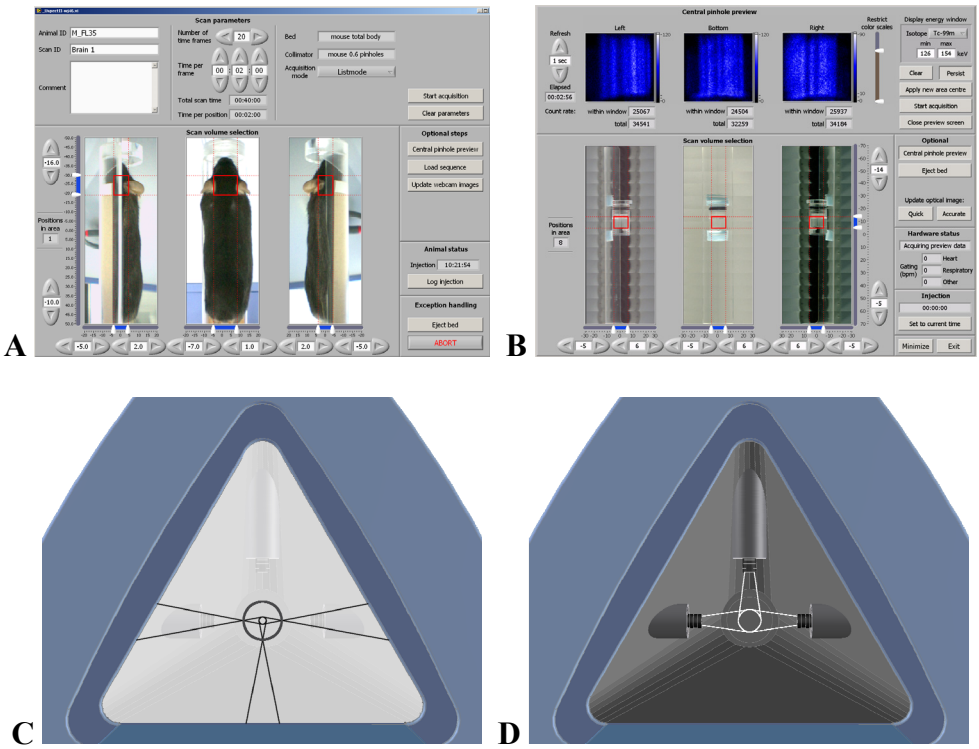

Figure 2: (A) Graphical user interface showing the webcam images of a mouse. The VOI selection is marked by red lines on top of each image. (B) The persistence scope screen displaying the webcam images of a small resolution phantom on the bottom of the screen and corresponding pinhole projections on the top of the screen, where individual rods can be readily distinguished. The projected gamma photons from 3 of the central pinholes of the gamma cameras (C) correspond to the left, right and top view of the optical images (D). Note that the inverted image from the bottom projection corresponds to the optical image from the top webcam.

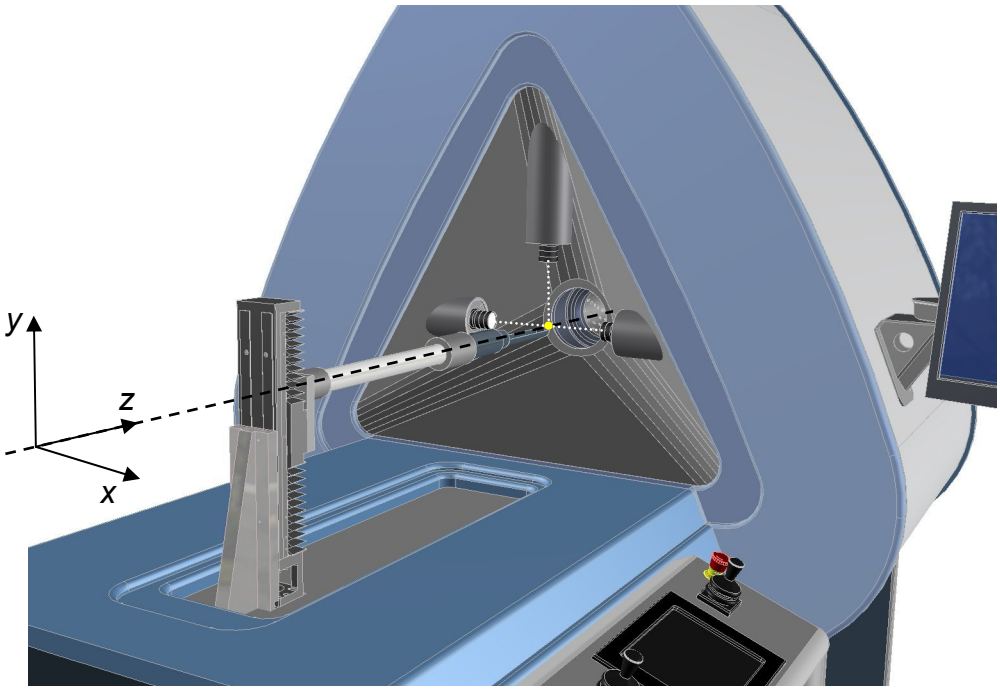

Figure 3: XYZ stage mounted in front of the collimator tube. The webcams are located in front of the collimator tube and the cameras focus to one point on the centerline of the collimator.

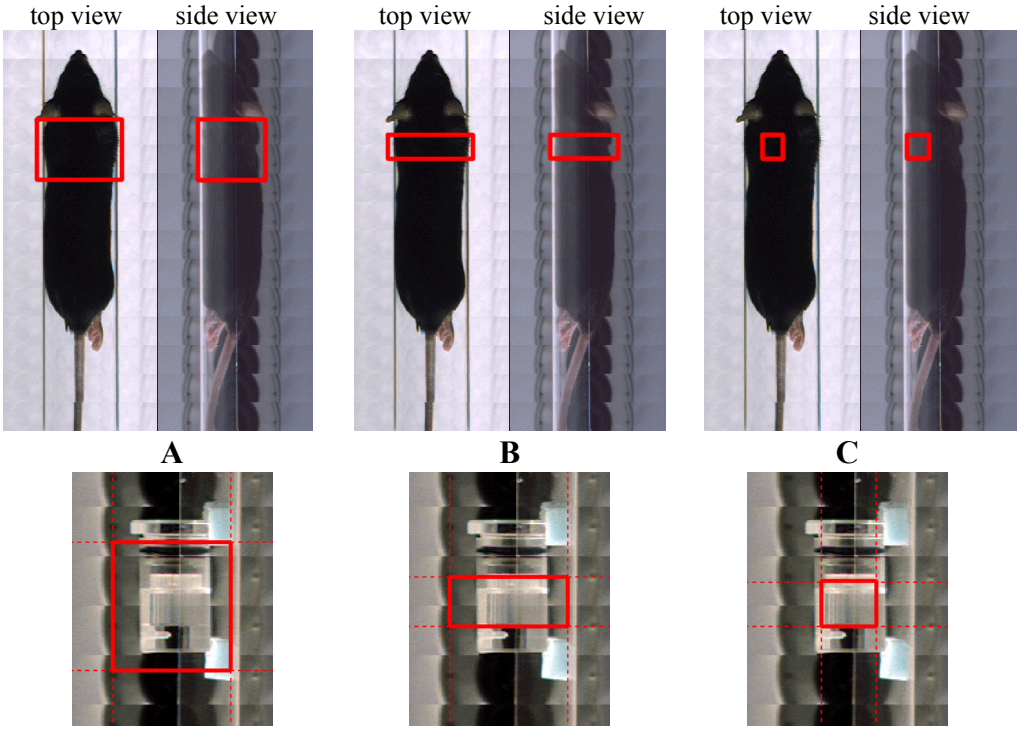

Figure 4: Different volume selection for a mouse heart and a resolution phantom. (A) non-focused scan, (B) medium-focused scan with the selection limited to one direction, (C) highly-focused scan with selection in all directions.

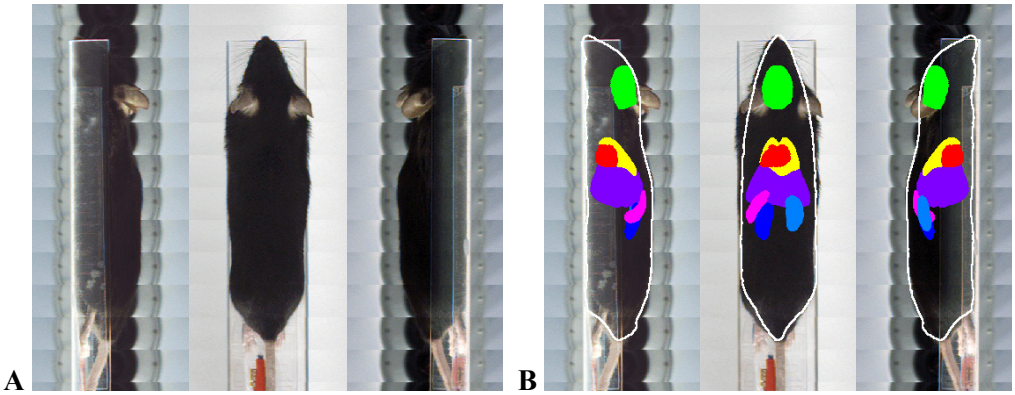

Figure 8: (A) Images from a mouse from the left, top and right webcams. (B) Same images with projections of the registered anatomical dataset containing the outline of the animal, the brain, the lungs, the heart, the spleen, the liver and the kidneys.

Chapter 7

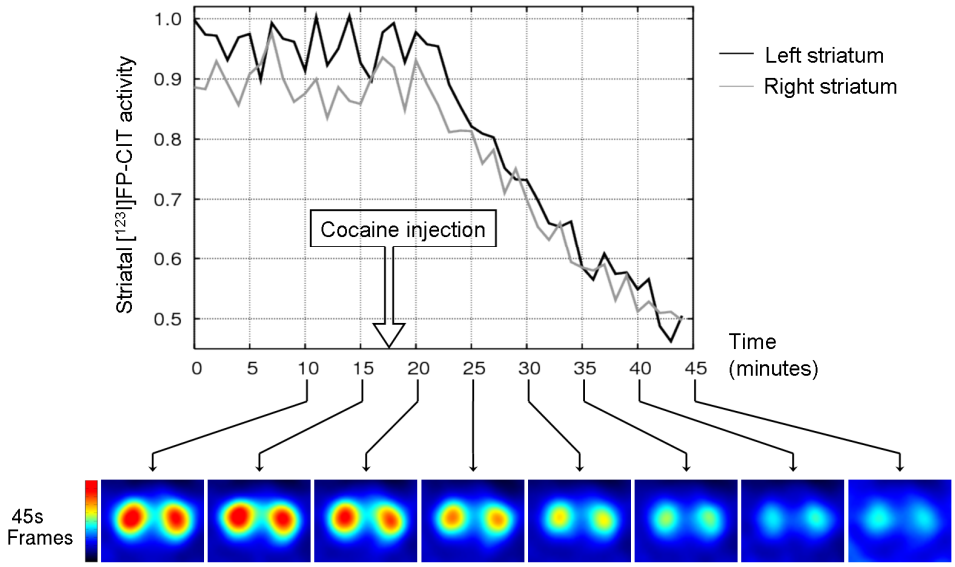

Figure 1: Coronal SPECT slices at the level of the striatum of a mouse. To label the DAT *in vivo*, [^{123}I]*N*-ω-fluoropropyl-2ß-carbomethoxy-3ß-(4-iodophenyl) nortropane ([^{123}I]FP-CIT) was used as a radiotracer and the new U-SPECT multiple pinhole technique was used to detect radiation emitted by ^{123}I labels. Before and up to about 3 minutes after administration of cocaine (i.p. 30 mg/kg body weight) a stable level of radioactivity is measured in the striatum representing a stable binding of FP-CIT to the DAT. Thereafter, cocaine starts occupying the DAT and displaces [^{123}I]FP-CIT binding, which is shown in the images and the associated curve. Approximately 28 minutes after the administration of cocaine, about 50 % of activity has been displaced by cocaine which indicates that the DAT rapidly binds cocaine.

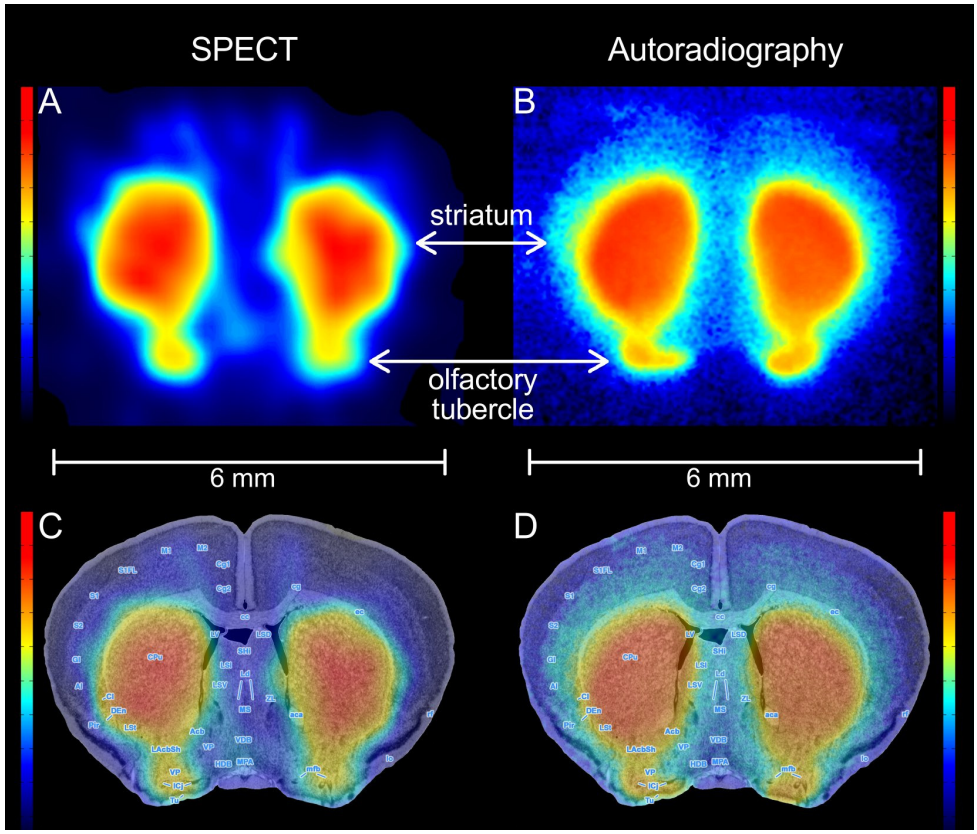

Figure 2: High resolution *in vivo* imaging of striatal DAT (left) compared to DAT autoradiography (right). (A) Coronal SPECT slice of the striatum, showing the possibility to distinguish sub-striatial structures through DAT binding of [^{123}I]FP-CIT. (B) Autoradiogram at the level of the striatum and olfactory tubercle of a mouse brain postmortem. Please note, that the autoradiography and SPECT images look similar, suggesting that pinhole SPECT is able to delineate DAT binding within a sub-millimeter range (C) SPECT slice overlaid on an anatomic brain atlas of the mouse [20,21]. (D) Autoradiogram overlaid on anatomic brain atlas.